M. Phil.

EFFECTS OF GAMMA AND NEUTRON IRRADIATIONS ON THE PHYSICAL, MAGNETIC AND ELECTRIC PROPERTIES OF Co-Cu-Cd AND Ni-Cu-Cd NANOFERRITES

EFFECTS OF GAMMA AND NEUTRON IRRADIATION ON THE PHYSICAL, MAGNETIC AND ELECTRIC PROPERTISE OF Co-Cu-Cd AND Ni-Cu-Cd NANOPARTICLES

By

MD. SALAUDDIN

MASTER of PHILOSOPHY in PHYSICS

Student ID: 14MPHY011P

DEPARTMENT OF PHYSICS

Chittagong University of Engineering & Technology, Chattogram-4349,

Bangladesh.

[Dept. of PHYSICS]

April - 2024

[2024]

EFFECTS OF GAMMA AND NEUTRON IRRADIATIONS ON THE PHYSICAL, MAGNETIC AND ELECTRIC PROPERTIES OF Co-Cu-Cd AND Ni-Cu-Cd NANOFERRITES

By

MD. SALAUDDIN

MASTER of PHILOSOPHY in PHYSICS

Student ID: 14MPHY011P

A thesis submitted in partial fulfilment of the requirements for the degree of

MASTER of PHILOSOPHY

DEPARTMENT OF PHYSICS

CHITTAGONG UNIVERSITY OF ENGINEERING & TECHNOLOGY

CHITTAGONG 4349, BANGLADESH

2024

DECLARATION

I hereby declare that the work contained in this Thesis has not been previously submitted to meet the requirements for an award at this or any other higher education institution. To the best of my knowledge and belief, the Thesis contains no materials previously published or another person except where due reference is cited. Furthermore, the Thesis complies with the PLAGIARISM and ACADEMIC INTEGRITY regulations of CUET.

.

MD. SALAUDDIN

Student ID: 14MPHY011P

Department of Physics

Chittagong University of Engineering and Technology (CUET)

DEDICATED TO

MY PARENTS

List of Publication

Journal Article

- M. Salauddin, M. Faishal Mahmood, M. Amirul Islam, M. Belal Hossen*, "Effect of gamma and neutron irradiations on the physical, magnetic and electrical properties of Ni–Cu–Cd nano-ferrites", Radiation Physics and Chemistry,226(2025),112254, September 2024. https://doi.org/10.1016/j.radphyschem.2024.112254

Conference

- M. Salauddin and M. Belal Hossen*, "Effects of Gamma and Neutron Irradiation on the Structural and Electric properties of CoCuCd and NiCuCd Ferrites Nanoparticles". 2nd International Conference on Physics for Sustainable Development and Technology (ICPSDT-2017) held on 10-11 December 2017
- M. Salauddin, M. Amirul Islam and M. Belal Hossen. "Effects of Gamma and Neutron Irradiation on the Structural, Magnetic and Electric Properties of Co-Cu-Cd Nanoparticles", International Conference on Physics for sustainable Development held on 08-10 March, 2018

Declaration of Supervisor

This is to certify that Md. Salauddin, Student ID 14MPHY011P has carried out this research work under my supervision and, he has fulfilled the relevant Academic Ordinance of Chittagong University of Engineering and Technology so that he is qualified to submit the following Thesis in the application for the degree of MASTER of PHILOSOPHY in Physics. Furthermore, the Thesis complies with the PLAGIARISM and ACADEMIC INTEGRITY regulations of CUET.

_____

Dr. Mohammad Belal Hossen

Professor

Department of Physics

Chittagong University of Engineering and Technology (CUET)

Acknowledgment

First and foremost, all praise to the *Almighty*, the most Beneficent, the most Merciful, who led me through this work and sustained me with help, guidance, the power to complete this work.

I would like to express my deep gratitude to Professor Dr. Mohammad Belal Hossen, Department of Physics, Chittagong University of Engineering and Technology, for his direct supervision, great interest, continuous help and valuable scientific discussions during this work. His unbelievable motivation and sincere effort made it possible for me to complete my thesis work.

I also would like to express my deep gratitude to Dr. Mohammad Amirul Islam, Chief Scientific Officer, Institute of Nuclear Science and Technology (INST), AERE, Savar of Bangladesh Atomic Energy Commission (BAEC), for his supervision, great interest, continuous help, and valuable scientific discussions during this research work.

I would like to pay special thanks to Professor Dr. Faruque-Uz-Zaman Chowdhury and Department of Physics, CUET who guided and suggested me positively throughout my degree.

I am pleased to express my deep appreciation to Professor Dr. H.M.A.R. Maruf, Head of the Department of Physics, Chittagong University of Engineering and Technology for his great interest, continuous help and valuable scientific discussions during this work.

I would like to thank the rest of the members of my examination committee for their encouragement and valuable comments.

I also would like to express my gratitude to all other faculty members in the Department of Physics, CUET to suggest and help me positively.

I am grateful to Mr. Sohel Rana, Technical officer, CUET postgraduate Lab for co-operation at the time of sample synthesis and other technical supports. Thanks also to other officers and staff of the Department of Physics.

I also Would Like to express my deep gratitude to M. Faishal Mahmood, Ph.D. research fellow, M. Shahbaz Khan, M.Sc. research fellow and Prof. Al Amin M. Sirajul Islam, Head, Physics Department, Chittagong College for his continuous help and friendship during his work.

I am thankful to my friend Bishakar Sharma, Lecturer, Department of Physics, Bakalia Shaheed N.M.M.J. College, Chattogram for his interest, valuable scientific discussion during this work.

Last but not least I would like to express my sincere gratitude to my dear wife Rabeya Sultana for her unwavering support and patience over the research work.

Author

April, 2024

MD. SALAUDDIN

Abstract

Irradiation effects on the structural, magnetic and electrical properties obtained by the sol-gel auto combustion synthesized $Co_{0.3}Cu_{0.2}Cd_{0.5}Fe_2O_4$ and $Ni_{0.3}Cu_{0.2}Cd_{0.5}Fe_2O_4$ nanoparticles by gamma (γ) and neutron irradiations are studied in the present research. The neutron irradiation of the samples has been done through neutrons ($1.50X10^{12}$ $cm^{-2}s^{-1}$ and 6.107×10^{13} $cm^{-2}s^{-1}$ thermal neutron flux) from the TRIGA MARK-II research reactor and gamma irradiation by 64 KCi cylindrical ^{60}Co source at room temperature (with doses of 1 MRad and 3 MRad at a dose rate of 0.1067 MRad/h) [for abstract the texts inside the first bracket may be omitted). XRD results show the stable spinel structure formation of the samples for the irradiation doses. The lattice constant (a_0) of the investigated samples has been increased with the increase of irradiation (neutron/gamma) due to the conversion of Fe^{3+} (0.67 Å) to Fe^{2+} (0.76 Å). Due to the redistribution of ions, changes in the lattice constant have been found by the irradiation through the results of the XRD and Rietveld refinement process. The saturated magnetization obtained from the VSM is found to changes and further analyzed by LAS. The frequency-dependent characteristics such as dielectric constant, electric modulus, impedance analysis and ac conductivity are inspected for all samples with both types of irradiation process. The electrical modulus spectroscopy ensures the dominant property as electric stiffness for investigated ferrite nanoparticles. Cole-Cole plots for the complex impedance analysis suggest the predominant contribution to conduction was through the grain boundary. In this study, electrical and dielectric properties have been carried out with the influence of gamma and neutron irradiations which can be interpreted by the existing theories.

বিমূর্ত

$Co_{0.3}Cu_{0.2}Cd_{0.5}Fe_2O_4$ এবং $Ni_{0.3}Cu_{0.2}Cd_{0.5}Fe_2O_4$ এর রাসায়নিক সূত্র সহ ন্যানো ফেরাইটের নমুনার ভৌত, চৌম্বকীয় এবং বৈদ্যুতিক বৈশিষ্ট্যগুলিতে গামা (γ) এবং নিউট্রন বিকিরণের প্রভাব অধ্যয়ন করা হয়েছে। এই নমুনাগুলি সোল-জেল অটো দহন পদ্ধতি দ্বারা প্রস্তুত করা হয়েছে। সংশ্লেষিত নমুনাগুলি দ্রুতগতির নিউট্রন ব্যবহার করে বিকিরিত করা হয়েছে (ফ্লাক্স: সর্বনিম্ন 1.50×10^{12} $cm^{-2}s^{-1}$ এবং 6.107×10^{13} $cm^{-2}s^{-1}$) TRIGA MARK-II গবেষণা চুল্লি এবং 64 KCi নলাকার 60Co উৎস থেকে γ রশ্মি কক্ষ তাপমাত্রায় 1 MRad এবং 3 MRad, 0.1067 MRadh-1 ডোজ হারে। এক্স-রে অপবর্তন (XRD) প্যারামিটার, চৌম্বককরণ, ডাই-ইলেক্ট্রিক ধ্রুবক, ডাই-ইলেক্ট্রিক লস ফ্যাক্টর, ইলেক্ট্রিক মডুলাস, প্রতিবন্ধকতা এবং এসি পরিবাহিতা বিকিরণের আগে এবং পরে তদন্ত করা নমুনার জন্য পরিমাপ করা হয়েছিল। XRD ফলাফলে দেখা যায় যে, বিকিরণ আয়ন পুনঃবন্টনের কারণে জালি ধ্রুবকের পরিবর্তন ঘটে। Fe^{3+} (0.67Å) থেকে Fe^{2+} (0.76Å) তে রূপান্তরের কারণে বিকিরণ (নিউট্রন/গামা) বৃদ্ধির সাথে তদন্তকৃত নমুনার জালি ধ্রুবক বৃদ্ধি পেয়েছে। অধিকন্তু, ক্যাটেশন বন্টন বিকিরণ (নিউট্রন/গামা) ডোজ বৃদ্ধির সাথে উভয় নমুনার এসি পরিবাহিতার মান বৃদ্ধিতে গুরুত্বপূর্ণ ভূমিকা পালন করে বলে মনে করা হয়। চুম্বকীয়করণ পরিমাপ করা হয় কম্পন স্যাম্পল ম্যাগনেটোমিটার (VSM) ব্যবহার করে কক্ষ তাপমাত্রায় 1.5T ($\mu0H$-এ) বিকিরণের আগে এবং পরে (নিউট্রন/গামা) বিভিন্ন মাত্রা প্রয়োগ করে। প্রাথমিকভাবে বিকিরণের আগে এবং পরে সম্পৃক্তি চুম্বককরণ বৃদ্ধি পায়। কক্ষ তাপমাত্রায় পালস ফিল্ড হিস্টেরেসিস লুপ কৌশল ব্যবহার করে বিকিরিত এবং অ-বিকিরিত ন্যানো ফেরাইটের চৌম্বকীয় বৈশিষ্ট্যগুলি সঞ্চালিত হয়েছিল। উভয় নমুনার এসি পরিবাহিতা, অন্তরক ধ্রুবক, অন্তরক ক্ষতির ফ্রিকোয়েন্সি নির্ভরতা অধ্যয়ন করা হয়েছে। ($Z^{//}$ বনাম $Z^{/}$) এর কোল-কোল প্লটগুলি বৈদ্যুতিক পরামিতির উপর নির্ভর করে ভিন্ন দুটি উপরিপাতিত অসম্পূর্ণ অর্ধবৃত্ত দেয়। এছাড়াও, ($M^{//}$ বনাম $M^{/}$) এর কোল-কোল প্লটগুলি নিশ্চিত করে যে, বৈদ্যুতিক কঠোরতা তদন্তকৃত নমুনার মূল বৈশিষ্ট্য। বৈদ্যুতিক বৈশিষ্ট্য যেমন ডিফিউশন সহগ এবং অন্তরক বৈশিষ্ট্যগুলি γ এবং নিউট্রন বিকিরণগুলির প্রভাবে পরিচালিত হয়েছিল। বিকিরণের পরে ছড়িয়ে পড়া প্রক্রিয়ার সক্রিয়করণ শক্তি হ্রাস পায়।

Contents

CHAPTER 4: RESULTS AND DISCUSSION

CHAPTER 5: CONCLUSION

List of Figures

List of Tables

Nomenclature

Symbol	Details
MRI	Magnetic resonance imaging
XRD	X-ray diffraction
M_s	Saturation magnetization
VSM	Vibrating Sample Magnetometer
Gy	Gray
MeV	Mega electron Volt
Hkl	Miller index
μ_{PE}	Photoelectric attenuation coefficient
BNCT	Borion-neutron capture therapy
n, p	Neutron-proton
Mrad	Mega rad
SHI	Swift heavy ion
$tan\delta$	Dielectric loss tangent
ε'	Dielectric constant
σ_{ac}	ac conductivity
Z	Impedance

ρ_X	X-ray density
N-R	Nelson Riley function
M	Electric modulus
M'	Real part of electric modulus
M''	Imaginary part of electric modulus
ε'	Imaginary part of complex permittivity
Z'	Real part of complex impedance
Z''	Imaginary part of complex impedance
kOe	Killo Oersted

CHAPTER 1: INTRODUCTION

1.1 BACKGROUND

Widespread uses of nanocrystalline ferrites in recent decades have sparked intense global scientific interest. Advanced features in memory cores, camera recorders, notebook computers, cellular phones, digital diaries, magnetic resonance imaging (MRI), DNA and RNA separation, drug delivery etc. introduced a new era in the field of electronic technology [1–5]. The nickel-copper ferrite, soft magnetic in nature, reveals highly essential electromagnetic characteristics like high magnetic permeability, high saturation magnetization, low dielectric losses, high electrical resistivity, better mechanical strength etc. therefore, emerges as a potential candidate and shows versatility in electronics and telecommunication with improved microwave devices, power transformers, loading coils, antenna rods, high-quality filters etc. [6–9]. In the research efforts, cadmium metal ion, divalent and nonmagnetic in nature, can be observed to show an appreciable modification of the electromagnetic properties of ferrites. In ferrite structure, Cd^{2+} ions occupy at A-site (tetrahedral) and 5s5p free orbitals in electronic configuration show sp3 hybridization with oxygen ions [10,11]. P. B. Belavi et al. [7] reports the influences of Cd^{2+} in potential Ni-Cu ferrite and shows better electromagnetic characteristics with the increasing intrinsic magnetic moment, higher dielectric properties and low intrinsic loss. Different applications in spacecrafts, satellites and nuclear environments like nuclear waste containers, nuclear reactors etc. can cause structural modifications with exposure to radiation and thereby noticeable changes in the physical characteristics. Therefore, it is important to learn about physical behaviors in radiation-rich environments. As a result, radiation techniques like gamma irradiation and neutron irradiation are become powerful tools and are being used worldwide to find out the actual behaviors in radiation-rich environments. Irradiation of gamma-rays can be observed to influence the structural and electromagnetic characteristics of ferrites with enhanced crystallographic defects [12–15]. Like gamma-rays, neutron irradiations also

influence the material properties significantly with various defects like vacancies, interstitials etc. [16–18]. In the literature survey, a few research efforts can be observed to investigate the potential Ni-Cd-Cu ferrite system while no investigations can be seen yet to reveal the modifications in structural and electromagnetic characteristics due to nonionizing radiation exposure; either gamma or neutron irradiation. Therefore, the present study has been performed with an aim to understand both the gamma and neutron irradiation effects on structural and electromagnetic behaviors. This is the first-ever effort, to the best of our present knowledge, performed to investigate the ionization effects in a potential Ni-Cd-Cu ferrite system. The synthesis of ferrite nanoparticles is an important step and different preparation methods can be observed worldwide. Synthesis techniques show noticeable effects on crystallite sizes and distributions, various imperfections such as impurities, micro-structural defects, dislocations etc. [19,20]. In this study, we synthesized nanoparticles with the renowned sol-gel auto-combusted technique. Different advantages like chemical homogeneity, uniform particle size, high purity, minimum evaporation loss etc. make the sol-gel method an efficient preparation technique in ferrite study [21,22].

As of yet, no studies comparing the effects of various radiations on the structural, magnetic, and electric characteristics of nanoferrites have been published. Because of this, we focused on investigating how gamma and neutron irradiation affect the structural, magnetic, and electric characteristics of Co-Cu-Cd and Ni-Cu-Cd nanoparticles for the first time. Altering the physico-chemical characteristics of these nanoferrites is an additional objective ($Co_{0.3}Cu_{0.2}Cd_{0.5}Fe_2O_4$ and $Ni_{0.3}Cu_{0.2}Cd_{0.5}Fe_2O_4$) by obtaining innovative properties using the sample low-cost technique of irradiation. The comparative analysis of the effects of two primary forms of irradiation—neutrons and gamma radiation from electromagnetic waves—on nanoparticles highlights the novelty of this productive work.

1.2 AIMS AND OBJECTIVES

These are the primary goals of the current study:

- ✓ Synthesis of $Co_{0.5}Cu_{0.2}Cd_{0.3}Fe_2O_4$ and $Ni_{0.5}Cu_{0.2}Cd_{0.3}Fe_2O_4$ nanoparticles by sol-gel technique.
- ✓ X-ray diffraction (XRD) has been used to characterize the structural properties of a variety of irradiated and unirradiated components.
- ✓ The variation of saturation magnetization (M_s) for various unirradiated and irradiated composition have been observed using Vibrating Sample Magnetometer.
- ✓ Complex dielectric constant, ac conductivity, and study of complex impedance spectra (Cole-Cole plot) of different compositions are examples of frequency-dependent transport properties that have been explored.

Possible outcomes of the research are as follows:

Magnetic nanoparticle fabrication using the sol gel process is anticipated. Materials are expected to be of higher quality in terms of phase pure synthesis, magnetization, and resistivity as a result of the primary focus on the synthesis of uniform magnetic nanoparticles with controllable size and their physical characteristics, which has sparked a search for general methods to create high-quality magnetic nanoparticles of various compositions. Scientists and engineers will be able to manufacture numerous devices for high frequency applications using the results.

1.3 THESIS OUTLINE

The following is the arrangement of the thesis:

Chapter–1 provides a synopsis of earlier research, an overview of Ni-Cu-Cd and Al based nano-crystalline ferrites, and an outline of the thesis' structure.

Chapter–2 deals with detailed theoretical background to study this type of research work and it have classified and described the magnetization term along with class of different materials. The detail in this chapter includes background material to help readers understand the purposes and goals of the investigation. It examines earlier study papers as well, allowing for a comparison of these results.

Chapter–3 incorporates with the detail of sample synthesis and irradiation procedure.

Chapter–4 includes specifics on the methods used in the experiments.

Chapter–5 describes the results and discussion of all studies.

Chapter-6 encompasses the scope of future work as well as the conclusions derived from the discussion and overall experimental outcomes.

At the conclusion, there is a brief summary of presentations linked to the ongoing study.

CHAPTER 2: LITERATURE REVIEW

2.1 GENERAL

This section represents the comprehensive overview of the research, which includes the main topic of the thesis that will be covered in literature review. Here, key studies related to this research will be discussed along with their methods, findings and contributions to this regarding field

2.1.1 EXPOSURE

The quotient of ΔQ divided by Δm is used to determine the exposure unit, or X, it reflects the total charges of electric on all of the ions of a single sign that are generated in the medium when all of the photon-released electrons in a volume element of the medium with mass m are completely stopped in the volume:

$$X = \frac{\Delta Q}{\Delta m} \ldots\ldots\ldots\ldots (2.1)$$

The roentgen (R) is a unique exposure unit that precedes the SI system. The ancient special unit, roentgen, is no longer used, but still appearing on occasion, especially in older literature. Furthermore, exposure has no SI unit.

2.1.2 ABSORBED DOSE

The ration of ΔE_D and by Δm defined as Absorbed dose, D, where ΔE_D is the energy that an element's volume, m, of matter receives from ionizing radiation:

$$D = \frac{\Delta E_D}{\Delta m} \ldots\ldots\ldots\ldots (2.2)$$

The rad is a unique unit of absorbed radiation that was frequently used until 1977: 1 rad = 100 erg g^{-1}. Rad is also a plural unit; for instance, 1rad or 20 rad. The rad is still often used despite

the introduction of the new special unit, the gray (Gy). The definition of the gray is the deposition of 1 J per kilogram, or 1Gy = 1 J kg^{-1}. In contemporary literature, the gray is gradually replacing the rad, and I'll make an effort to do the same in this essay. Since 1 Gy = 100 rad, the conversion between the rad and the gray is straightforward and leads to the immediately apparent equivalence. 1 rad equal 1 cGy. As a result, the centigray has gained widespread acceptance among radiation physicists for use in scientific writing.

2.1.3 Decay Constant

It is the ratio obtained by dividing dP by dt, where dP is the likelihood of a given nucleus having a spontaneous nuclear change from that state over a certain amount of time dt, determines the decay constant, of a radioactive nuclide in a given energy state:

$\lambda = \frac{dp}{dt}$..... (2.3)

The decay constant has a size of t^{-1}.

2.1.4 Gamma Rays

X-rays and gamma rays are examples of electromagnetic radiations, or photons, that possess sufficient energy to induce ionization. Atomic and radioactive elements are physically equivalent, however due to custom, ionizing photons created by "machines" are commonly referred to as X-rays while radioactive sources that produce ionizing photons are referred to as gamma rays.

2.1.5 Neutrons

The typical coulombic interactions associated with charged particles cannot be observed in neutrons since they are uncharged particles. However, neutrons frequently make up a large portion of the tissue dose and frequently have significant biological effectiveness due to their high LET (vide infra). Depending on the processes they emerge from, neutrons are produced

at a very wide range of energy. Thermal neutrons are produced by nuclear reactors and get their name from the fact that they have kinetic energies of around kT, or a minuscule fraction of an electron-volt, as well as neutrons with energies up to several MeV, as a result of the fission process. Fusion produces neutrons with energies of about 14 MeV, while reactions in space, as well as within and surrounding massive physics accelerators, produce neutrons with energies of several hundreds of MeV. At each of these energies, the procedures for transferring energy to tissue vary.

2.1.6 ANALYSIS OF STRUCTURE USING XRD

Ferrite crystals can provide a plethora of information about their crystal structure and crystallite size through XRD examination. As was previously mentioned, the crystal structure of each variety of ferrite is determined by its chemical makeup. X-ray diffraction is utilized to make sure the composition is formed. The Miller index of the scattering plane, denoted as (hkl), contributes the inter-planer gap. As stated by Bragg's diffraction equation

$$2d_{hkl}sin\theta = n\lambda \quad \ldots\ldots\ldots\ldots \quad (2.4)$$

The interplanar space is indicated by d_{hkl}, the diffraction order is shown by n, the diffraction angle is θ, and the X-ray wavelength is expressed by λ. The features spectrum of each ferrite structure is formed by the diffraction of the scattered X-rays. Fig. 2.1 displays an illustration of an X-ray for Mg-Cu-Zn-ferrite. [70]. The following relationship can be used to derive the lattice parameter from an XRD spectrum.

$$a_{exp} = d_{hkl}(h^2 + k^2 + l^2)^{\frac{1}{2}} \quad \ldots\ldots\ldots\ldots \quad (2.5)$$

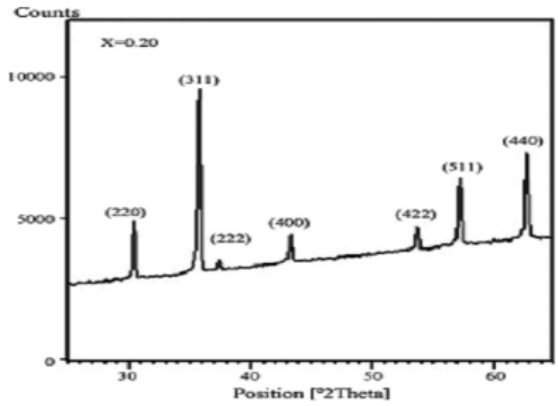

Fig. 2.1 XRD pattern of sample [70]

2.1.7 THE NEUTRON AND NUCLEAR FORCE

Protons are responsible for the positive charges in atomic nuclei, as has already been mentioned, and hydrogen has the simplest nucleus, consisting solely of one proton. If the proton is assigned a mass number of 1, then the mass numbers of the nuclei should coincide with the atomic numbers of the nuclei if every successive nucleus is just a multiple of the proton. It was found that this was untrue. It was found that the nuclear mass numbers, except for hydrogen, were almost twice as big as the equivalent atomic numbers and became disproportionately larger as the atomic numbers rose. It was also necessary to consider the stability of the nucleus against the repulsive coulombic pressures exerted by the nuclear protons.

2.1.8 NEUTRON CLASSIFICATION

Neutron was discovered in 1932 by Chadwick. In a power reactor, radioactive chain reactions typically produce neutrons. With a mass of 1.67 10^{-27} kg and no electrical charge, the neutron is a subatomic particle that is found in practically all nuclides (with the exception of the standard hydrogen isotope and protium).

On the basis of their kinetic energy, neutrons are categorized. Although there isn't a distinct line separating the categories, the following restrictions can be a helpful benchmark:

Slow (thermal) neutrons (0.003–0.4eV), Cold neutrons (<0.003eV), high-energy (relativistic) neutrons (>10MeV, intermediate neutrons (100eV–200keV), slow (epithermal) neutrons (0.4–100eV), fast neutrons (200keV–10MeV), Note: 1eV = 1.6×10^{-19}J.

Thermal neutrons have a kinetic energy of 0.025 eV on average, which corresponds to a neutron speed of 2200 ms^{-1}.

2.1.9 RADIATION'S INTERACTION WITH MATTER

In terms of theory and application, the interaction of radiation with substances is crucial. This encounter can be viewed from a variety of angles. The quality of a material may change as radiation interacts with it. Understanding how radiation affects materials used in electrical devices and control systems has become increasingly important in light of recent advances in nuclear engineering, such as the utilization of radioactive isotopes and accelerators for elementary particles.

The types and energies of the entering particles (or photons) have an impact on the interaction processes. For instance, the electromagnetic spectrum (photons) includes frequencies spanning many decades. For charged particles, the circumstance is similar. Their energy ranges from fractions of eV to 1020 eV, just like ultra-high energy cosmic rays. For instance, the energy dissipation process in a gas medium produces ion pairs, or electron and, separated positive ions and flow through the medium. The typical energy needed to produce an ion pair is 30 eV. The dense medium produces an electron-hole pair with a 3.6 eV energy requirement in semiconductors Different types of ionizing radiation (fluxes of and particles, X-rays, neutrons and gamma rays, etc.) have a significantly larger impact on materials. Depending on the nature

and energy of the incident radiation, these interactions may involve nuclear processes, elastic scattering, or inelastic scattering [15].

The particles or rays released during radioactive decay have certain energy and could contain a charge or not. All of them interact with the environment they are released into, transmitting energy to that environment until eventually all of their energy is lost. For the time being, it should be evident that these energy transfers will have significant effects on radiation shielding, radiation detection, radiation biology and nearly all real-world applications of radiation protection. The basic ways that radiation interacts with matter are as follows:

- Excitation
- Ionization
- Capture

Generally speaking, in radiation types and contact scenarios, the most important are ionization and excitation. Under some conditions, capture reactions for specific radiation types result in some significant results that its

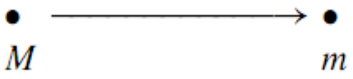

explain. Some radiation interactions can be compared to collisions between "billiard balls," since they solely cause elastic scattering. If a particle of mass M approaches a particle of mass m that is currently stationary:

In an interaction that is supposed to be a "head-on" collision, the maximum amount of energy that may be exchanged in a single collision can be determined through the conservation of energy and momentum. Assume particle M had velocity V prior to colliding with the object and velocity V_1 following the impact. Particle m was at rest prior to the collision and had velocity v following it. Undoubtedly, if this is an orbiting electron or any other particle, it is in motion. However, from a relative standpoint, in terms of this interaction, it can be said to have been at rest. Then, by maintaining all energy and motion, its discover that:

$\frac{MV^2}{2} = \frac{MV_1{}^2}{2} + \frac{mv^2}{2}$ ..... (2.6)

$MV = MV_1 + mv$ ..... (2.7)

Solving from Eq. (2.7) for *v*, it is found $v = \frac{MV - MV_1}{m}$, if this is substitute into Eq. (2.6), then the Eqn is $V_1 = \frac{(M-m)v}{M+m}$

If, use this expression for V_1, in a single collision, the greatest amount of energy that can be transferred is given as:

$Q_{max} = \frac{MV^2}{2} - \frac{MV_1^2}{2} = \frac{4MmE}{(M+m)^2}$ ..... (2.8)

2.1.10 INTERACTION OF GAMMA-RAYS WITH MATTER

This paragraph will examine the mechanism of gamma irradiation's interaction with matter in order to understand the characteristics in a gamma spectrum induced by interactions with the detector and surroundings (Fig. 2.2). Compton scattering, photoelectric absorption and pair creation are the three main interaction processes for radiation measurements.

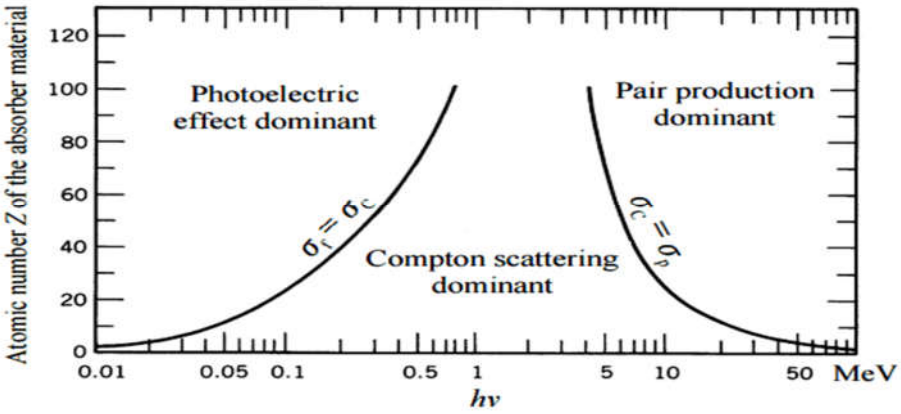

Fig 2.2. The relative significance of various gamma radiation interactions with matter processes [165]

In all three instances, there is partial or gamma-ray photon energy is completely converted to electron energy, resulting in the generation of free electrons and the formation of electron-ion or electron-hole pairs as these electrons are slowed down as they travel through the matter.

2.1.11 PHOTOELECTRIC ABSORPTION

Photoelectric absorption is produced when a gamma ray photon interacts with an atomically bound electron. If the gamma ray energy is greater than the energy required to bond to the K-shell of the innermost electron (Fig. 2.2), the electron may be ejected from that shell. If the energy is insufficient to eject a K electron, L or M electrons will be ejected in its place. Since the K, L, and M electron shells have binding energies, this causes abrupt discontinuities (K, L, or M edges) in the photoelectric absorption curves. The electron gains kinetic energy as a result of the gamma ray being completely absorbed and this is indicated by:

$$E_e = E_\gamma - E_b \quad \ldots\ldots\ldots\ldots (2.9)$$

Where, E_γ denotes the gamma ray energy and E_b represents the energy binding the electron in its shell. In most cases, the recoil atom must hold onto a relatively little amount of energy in order to maintain momentum after an electron is released.

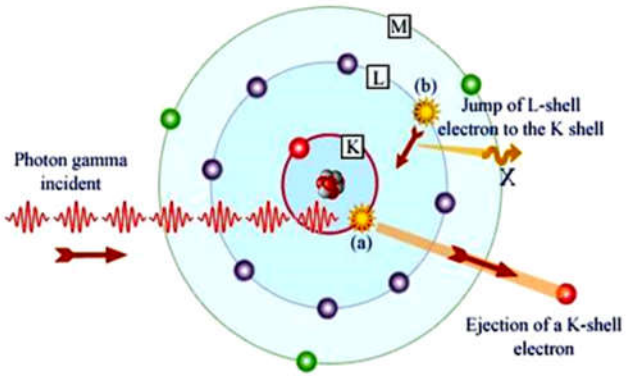

Fig. 2.3 The process of photoelectric absorption [166]

For all practical reasons, its disregard this because it is so little. Either the extra energy is spread among the atom's remaining electrons, absorbing additional energy, or an outer shell electron

(of greater energy) is added to replace the vacancy left by the photoelectron, causing the photoelectron to produce the distinctive X-ray known as X-ray fluorescence. The atom is left in an excited state with extra Eb energy as a result of this operation. If photoelectric absorption takes place, this X-ray may then continue to emit X-rays until all of the energy has been absorbed.

The energy of the -ray determines the energy level at which the electron is expelled. A "K" electron has the highest probability of being expelled (Fig. 2.4).

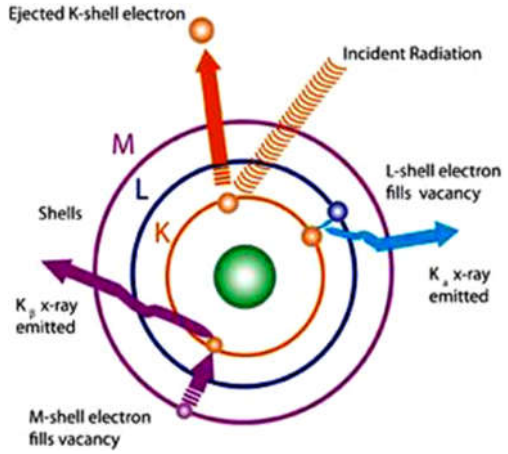

Fig. 2.4 X-ray fluorescence radiation emission [167].

L or M electrons will be released in its stead if there is insufficient energy to remove a K electron. Consequently, discontinuities can be seen in the photoelectric absorption curves. At the binding energies that correspond to the electron shell, these absorption edges occur. According to a complicated relationship, raising the absorber's atomic number (Z) and lowering the energy of gamma ray energy increases the likelihood that photoelectric absorption will happen to a photon, which is given as a relation:

$$\tau \approx \frac{Z^n}{E_\gamma^m} \quad \ldots\ldots\ldots\ldots (2.10)$$

Where, depending on energy, n and m indicate values between 3 and 5. The associated cross section can be used to obtain the photoelectric attenuation coefficient, μ_{PE}, in the following way:

$$\mu_{PE}(m^{-1}) = \tau \times \rho \times \frac{N_A}{A} \quad \ldots\ldots\ldots\ldots (2.11)$$

where A stands for average atomic mass, N_A is Avogadro's number, and ρ is the density of the absorbing substance.

2.1.12 COMPTON SCATTERING

In this instance, the photon will release its energy to an electron. A new gamma photon with less energy absorbs the leftover energy. This brand-new photon is referred to as being scattered because it will travel in a different direction. Similar to a beta particle, the electron that was released from the atom causes ionizations.

In contrast to the photoelectric effect, this process:

- The photon only gives the electron a little portion of its energy and
- The process only involves the (basically) unbound electrons in the outer orbital.

The photon moves along with less energy when in relation to the line of incidence, it is dispersed at an angle. If the photon with energy E is envisioned as a wave with wavelength, then Compton scattering can be described:

$$\lambda - \lambda_o = \frac{h}{mc}(1 - \cos\theta) \quad \ldots\ldots\ldots\ldots (2.12)$$

where, $E_\lambda = h\upsilon = \frac{hc}{\lambda}$

When the scattering angle is known, conventional mechanics can be used to calculate:

- The direction the electron is travelling at an angle and
- The proportion of the electron to the dispersed photon when the energy is split.

When $\theta = 180^{o}$, a photon can transfer the most energy possible to an electron, when the photon is directly reflected rearward. This still falls short of the maximum amount of energy that a single photon can transport during a photoelectric contact.

Value can correspond to the scattering angle between 0^0 and 180^0. The quantity of energy delivered to the electron decreases with decreasing angle. Simply "grazing" an electron ($= 0^0$) results in no energy transfer.

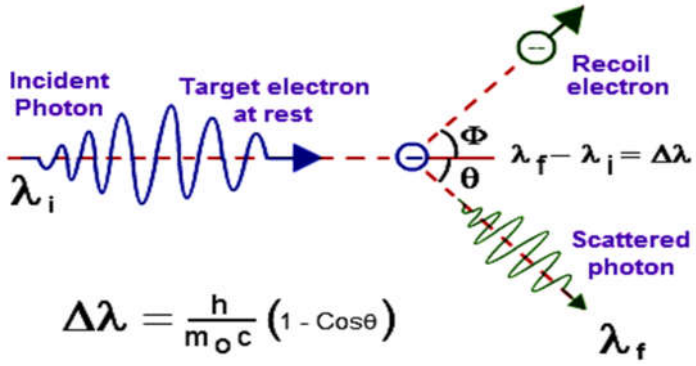

Fig. 2.5 Process of Compton scattering [168]

The absorber's atomic number and the input photon's energy both affect the likelihood of a Compton interaction occurring. This is best described by:

Compton scattering probability = $k \frac{Z}{A}$

For the geometric arrangements typically utilized for counting samples, an intriguing scenario arises:

The sample is put within a sizable shield that is close to the detector and is often composed of lead. As a result, the detector "sees" fewer photons that originated straight from the sample and less photons that were all reflected backwards by around 180^0 degrees from the absorber.

Regardless of the incident energy of the photons on the lead shield, this backscattering produces photons with almost the same energy. In the pulse height spectrum, the backscattered photons appear as a board peak at low energies.

2.1.13 PAIR PRODUCTION

Sometimes, high intensity gamma photons split into two electrons, one positive and the other negative. The positive electron is known as a positron. The interaction is called pair production. The effect may be explained by the relativity theory, which maintains that "matter" and "energy" are essentially two names for the same thing. According to the equation, an amount of energy E can be created from a particle of mass m, and vice versa:

$E = mc^2$ …… (2.13)

where c is the speed of light.

One effect of this idea is pair creation: Two particles with the same mass but opposing electrical charges are created from a photon with energy E.

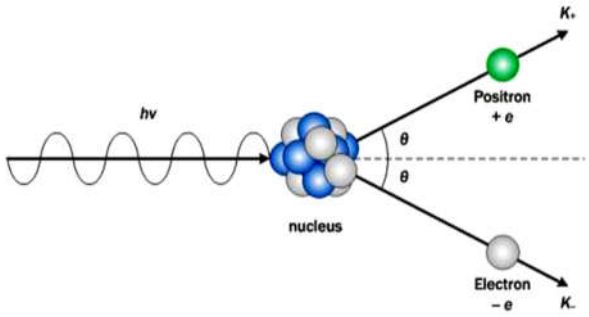

Fig. 2.6 Procedure for producing pairs [169].

The extra energy is split between the two particles as kinetic energy:

$E_\gamma = (m_+ + m_-)c^2 + \frac{1}{2}(m_+ + m_-)v^2$ …… (2.14)

The two participating particles are both electrons. One is the positively charged electron, or positron, while the other is the negatively charged electron. Although it has the opposite

electrical charge from the negative electron, it has the same mass and nuclear characteristics. The negative electron is sometimes referred to as a negatron to distinguish it from the positive electron.

The Einstein equation can be used to determine how much energy is equal to (9.11×10^{-28} g), which is the mass of an electron or positron. It is equal to 511 keV for a single particle and 1022 KeV for a pair of positrons and neutrons. Therefore, the above equation may be expressed as:

$$E_\gamma = 1022 \text{ keV} + \frac{1}{2}(m_+ + m_-)v^2 \quad \ldots\ldots\ldots\ldots (2.15)$$

When the positron is at rest, it is not a stable particle. Similar to a negatron, a positron formed by pair formation will lose energy through interaction with electrons in the absorbing materials. But when it has exhausted all of its kinetic energy, it is unable to coexist with other electrons, which leads to a nuclear reaction. In this reaction, two photons with energies of 511 keV each are created as a result of a positron and a negatron pair annihilating one another. (The positron and any electron may annihilate in this way; it need not be the one produced during the pair creation).

In order to maintain momentum during the reaction, there are two photons involved. It can be pictured as:

$$\beta_+ + \beta_- \rightarrow \gamma_1 + \gamma_2 \text{ and } E_{\gamma_1} = E_{\gamma_2} = 511 \text{ KeV} \quad \ldots\ldots\ldots\ldots (2.16)$$

Only when an input photon has enough energy (more than 1022 keV) to provide at least the mass of a pair of positron and negatron atoms can pair formation takes place. In actuality, it only matters for photon energies greater than 1.5 MeV. Pair formation is more likely to happen at higher photon energies.

2.1.14 INTERACTION OF NEUTRON WITH MATTER

When neutrons collide with atom nuclei, one of two outcomes is possible: either the neutrons scatter or the nuclei recoil with momentum conservation (elastic scattering), or the neutron loses kinetic energy and emits gamma radiation (inelastic scattering). Neutron capture can lead to the creation of new nuclei (transmutation), the nucleus's fragmentation (fission), or the emission of additional nuclear particles from the nucleus. Similar to photons, neutrons fall under the umbrella of indirectly ionizing radiation. They can range from as low as 10^{-8} eV for ultra-cold neutrons to as high as a few GeV for relativistic cosmic neutrons and their kinetic energy E_k^n is used in science, commerce, and medicine. An intermediate phase that enables neutrons to transmit energy to an absorber medium involves the transfer of energy from the neutron to a charged particle through Coulomb interactions between the released charged particle and orbital electrons of the absorber. As a result, protons, nuclear particles, and recoiling nuclei are secondary charged particles that the neutron beam uses to deposit energy into the absorber. Neutrons may experience elastic, inelastic, or non-elastic scattering as they enter an absorbing material, or they may start nuclear events such, as spallation, neutron capture and fission. In medical physics, two different kinds of neutrons are crucial: (1) Borion-neutron capture therapy (BNCT) employs thermal neutrons.

(2) Brachytherapy and external beam radiotherapy both use fast neutrons.

Thermal neutrons play a major role in the indirect production of radionuclide sources that are utilized in nuclear medicine imaging, external beam radiation, and brachytherapy. The warm, moderate, and fast neutron zones are three areas of neutron kinetic energy that are significant in neutron dosimetry.

Since neutrons are neutral particles and are not affected by nuclear charge like protons and electrons are, they can approach a target nucleus unaffected by a Coulomb attractive or

repulsive force. Short-range attractive nuclear forces allow neutrons to interact with the target nucleus once they are close to it and start a variety of nuclear reactions. There are five main ways that neutrons interact with absorber nuclei:

1) Neutron Capture
2) Elastic Scattering
3) Non-elastic Scattering
4) Capture of neutron
5) In-elastic Scattering
6) Fission

Here is a basic explanation of the interactions between neutrons and neutron capture:

The nuclear process in which a thermal neutron collides with a target nucleus and causes neutron absorption in the target nucleus; the production of a new nuclide that is different from the target nucleus in terms of atomic mass number and/or number; the emission of a proton is referred to as "neutron capture." [(n, p) reaction Gamma-ray or particle-emitting neutron capture [(n,γ) reaction: neutron capture with γ radiation emission] in the process] . Depending on the type of neutron capture product, even after the instantaneous emission of a particle or ray, neutron capture often results in the production of an unstable radionuclide that decays with a unique half-life that can range from a few nanoseconds to many years. Thermal neutron capture has been used to identify most man-made radionuclides created in the last few decades from stable samples fed into nuclear fission reactors. Neutron activation is more commonly employed instead of neutron capture when it is used to produce radionuclides or analyze trace elements in material samples.

CHAPTER 2: LITERATURE REVIEW

2.1.15 ION IRRADIATION

Ion irradiation involves directing energetic ions at a target material to start altering its structural, transport and physical properties. It has been discovered that a wide range of materials, including semiconductors, metals, insulators, ceramics, biological samples, and polymers are responsive to this type of material modification since it is non-equilibrium in nature and therefore fascinating. In the past ten years, attention has switched to the basic principles of ion-solid interaction. This change is the result of a growing requirement to use beams to alter materials for certain applications. Ion beam interactions with solids take place out of equilibrium. An energetic ion loses energy when it enters a target through two essentially distinct mechanisms:

(i) High-energy, inelastic collisions between matter's atomic electrons and highly charged, energetic ions [electronic energy loss $(dE/dx)_e$] and

(ii) Elastic scattering from the matter's atomic nuclei [nuclear energy loss $(dE/dx)_n$].

Energy is transferred from the projectile to the atoms of the matter in the inelastic collision (cross section $10^{-16}cm^2$) by the excitation and ionization of their surrounding electrons. Electronic energy lost in a collision ranges from a few eV/Å to a few keV/Å. This is the primary method for energy transfer to the material changing its properties for nanoparticles traveling at a rate comparable to the electron's Bohr velocity. The target materials electrical, thermal, and structural characteristics, the projectile ion's mass, and the irradiation settings all affect the type of change [17].

2.2 Survey of Earlier Works

$Ni_{1-x}Zn_xFe_{2-y}Dy_yO_4$ nanoferrites were examined by Veena et al. [18] using a unique, effective, and cost-effective combustion approach. X-ray diffraction analysis verified the phase formation. The lattice constant rises as Zn content rises and falls as Dy^{3+} ion content rises. The range of the typical crystallite size was between 11 and 31 nm. The loss tangent and dielectric constant both decrease as the frequency rises, whereas the ac conductivity increases. Electrical conductivity in the samples is hindered by the addition of Dy^{3+} ion. The resonance peaks may be seen between 5-7 MHz in frequency. The lattice constant, crystallite size, and dielectric characteristics of irradiated samples improved due to the formation of Fe^{2+} ions by radiation damage. With increasing Dy content and lower frequency in samples exposed to radiation, peak heights are reduced and peak positions are shifted toward higher frequencies. The complex impedance study demonstrates that the grain boundary is the conduction mechanism.

The citrate precursor auto combustion approach has been successfully used to produce Ni-Cu-Zn and Mg-Cu-Zn nanoferrites with the chemical formulas $Ni_{0.35}Cu_{0.15}Zn_{0.5}Fe_2O_4$ and (b) $Mg_{0.35}Cu_{0.15}Zn_{0.5}Fe_2O_4$, according to S.T. Assar et al. [7]. It has been investigated how exposure to ^{60}Co gamma rays at the effects of 1 and 2 Mrad doses are seen in the structural, electrical, and some magnetic properties.

The XRD findings show that in Ni-Cu-Zn ferrite samples, the ordered areas of the crystallites (grains) are displaced by the disordered grain boundary area, which leads to a drop in crystallite sizes as the irradiation dose rises. This phenomena also results in a reduction in densification and an increase in porosity, specific surface area, and microstrain. On the other hand, the increasing crystallite sizes of the Mg-Cu-Zn ferrite samples demonstrate how crucial the irradiation energy was in promoting well-ordered grain sizes and unit cell stacking, which in turn led to increased densification and lower porosity, specific surface area, and micro strain.

In addition, the little increase in lattice constant seen in all studied samples might perhaps be attributed to the conversion of some Fe^{3+} ions (0.67) to Fe^{2+} ions (0.76).

Cation redistribution, which primarily modifies the magnetic characteristics of the materials, is responsible for the observed increase in saturation and residual magnetism after irradiation. The distribution of cations in the samples under study has been suggested such that the magnetic moment rises with magnetization and is comparable in the theoretical and experimental values. The accuracy of the hypothesized cation distribution may also be assessed using the lattice constant values, which accord well with theory and experiment.

Similar to Ni-Cu-Zn ferrite samples, the DC conductivity values of Mg-Cu-Zn ferrite samples increase with increasing irradiation dosage; however, the additional impact of their microstructures, in addition to the cation redistribution, results in larger values.

Two overlapping incomplete semicircles are visible in the samples' Cole-Cole (Z″ vs Z') plots. The first occurs because the grain boundaries conduct at low frequencies, where it is impossible to know their electrical characteristics, and the second happens at high frequencies because of grain conduction; it exhibits a significant variation in values with radiation exposure and has larger capacitance and lower resistance than grain boundaries.

The semicircular Cole-Cole graphs of (M″ vs M') guarantee that the electric stiffness is the main characteristic of the examined samples both before and after the irradiation dose. Finally, it can be said that although $Mg_{0.35}Cu_{0.15}Zn_{0.5}Fe_2O_4$ samples exhibit balanced behavior with higher irradiation exposure, $Ni_{0.35}Cu_{0.15}Zn_{0.5}Fe_2O_4$ samples exhibit an enhancement in the magnetization and resistivity more than $Mg_{0.35}Cu_{0.15}Zn_{0.5}Fe_2O_4$ samples do when exposed to very high dose gamma irradiation.

All of the samples in the investigation have a single-phase cubic spinel structure, by Karim et al. [19]. Ni-Zn ferrites samples from both irradiated and non-irradiated samples showed all significant peaks. Due to ion-induced disorder, the irradiation samples in both systems exhibit

lower intensities and more line broadening. The Ni-Zn ferrite was exposed to gamma ray Co^{60} radiation, and the results demonstrate that stable induced flaws are present at ambient temperature. These flaws are anticipated to appear as a result of combining two or more effects. The observed particle sizes for the unirradiated and irradiated samples, as determined from the widening of the (311) XRD peak, are 52-30 μm and 10-24 μm, respectively. The observed increase in the Curie temperature and saturated magnetic moment after gamma irradiation is attributed to the partial formation of ferrimagnetic centers, cation rearrangement in the 1lattice, and ion-induced disorder. In a study by Kee-Nam Choo et al. [20], it was discovered that HANARO's irradiation facilities were mostly used for the various nuclear material irradiation experiments that consumer had requested. Despite the fact that most irradiation testing has been connected to national research & development (R & D) regarding nuclear power, the requirement for neutron irradiation of electro-magnetic materials is rapidly expanding at HANARO. After learning from the experience with HANARO, KAERI is currently building the KIJANG research reactor (KJRR), which is intended to increase the nation's capacity for the supply of radioisotopes as well as to the irradiation facilities, such as the NTD facilities for large-scale production of power semiconductors and the thermal neutron shielding facility for fast neutron irradiation. The investigation of the distinct effects of heat and fast neutron irradiations on the characteristics of electro-magnetic materials can be successfully conducted using the NTD and FNI capabilities of the KJRR reactor. The field of research on electro-magnetic materials appears to hold considerable promise for the foundation for the study of materials employing neutron irradiation.

Without undergoing additional heat treatment, M.A. Ahmed et al. [8] produced $MnFe_2O_4$ nanoferrite with a single spinel and cubic symmetry using the citrate method. The $MnFe_2O_4$ nanoferrite is subjected to gamma radiation, which reduces its particle size (L) while increasing the unit cell volume, TC and room temperature values of χ_M, ε', $tan\delta$ and σ. Finally, the

behavior of irradiation nanoferrites is mentioned for alternations using their magnetic and dielectric properties. This evidence supports the claim that our nanoferrite is utilized to detect nuclear pollution and has the greatest potential for usage as a radiation detector in commercial and technological applications.

Dogra et al. [21] investigated changes in the dielectric characteristics of Al^{3+} substituted Mg-Mn ferrite. The electrical characteristics had changed, and the X-ray diffraction studies indicated that the ion irradiation was the cause of compressive strain. Koops's theory and Maxwell-Wagner type interfacial polarization were used to explain the dielectric constant dispersion of unirradiated materials.

In situ monitoring of the electrical resistance of a $Li_{0.25}Mg_{0.5}Mn_{0.1}Fe_{2.15}O_4$ micro ferrite thin film exposed to 199 MeV Au^{14+} ions were examined by Ghosh et al. [22]. Utilizing the two-probe method, an in-situ measurement of electrical resistance was made to evaluate the rapidly occurring changes in the electrical properties of the film caused by heavy ions. It was shown that following exposure to radiation with a fluence of 1×10^{13} ions/cm^2, the resistivity value drops sharply from $1.5 \times 10^8\ \Omega$ cm to $1 \times 10^8\ \Omega$ cm.

The effects of 50 MeV Li^{3+} in ion irradiation on the structural and magnetic characteristics of Ti^{4+} substituted $Li_{0.5}Al_{0.1}Fe_{2.4}O_4$ were investigated by Chhantbar et al. [23]. The effects of 50 MeV Li^{3+} ion irradiation on the structural and magnetic properties of polycrystalline spinel ferrite samples have studied using XRD, magnetization and ^{57}Fe Mossbauer spectroscopy.

The central enhancement of the Mossbauer spectra after the irradiation was believed to be caused by the paramagnetic centers created by the SHI irradiation. XRD examination and Mossbauer Lorentzian intensity revealed that the partial formation of paramagnetic centers and the rearrangement of cations in the lattice were responsible for the decrease in the saturated magnetic moment following SHI irradiation. The development of localized paramagnetic

centers is the cause of the central amplification seen in the irradiated Mossbauer spectra materials, not amorphization.

The structural and magnetic characteristics of $Mg_{0.95}Mn_{0.05}Fe_2O_4$ nanoparticles were investigated by Kumar et al. [24] using impact of 100 MeV Si^{7+} irradiation. It was discovered that there was a modest increase in particle size after irradiation. Super paramagnetic relaxation effects were seen in both the clean and the irradiated samples using Mossbauer spectroscopy at room temperature. The room's temperature Ion irradiation did not considerably alter the Mossbauer spectra. All of the samples exhibited strongly defined magnetic ordering at 5 K, even though they were all in super paramagnetic condition at room temperature.

The saturation magnetization was found to be improved based on the results of the magnetization tests done on the irradiation samples. This was explained in terms of the creation of single domain particles under coercivity control, where the inability to reverse the magnetization was due to the absence of domain barriers. The surface state pinning of domains was released and the magnetization of the nanoparticles was enhanced by irradiation.

Both Darwish et al. [25] and Hemeda et al. [26] investigated the impact of ^{60}Co based impact of gamma irradiation on the electrical properties and composition of co-zinc ferrites. There was a shift in the XRD peak positions following irradiation. The ferric ions underwent a shift due to irradiation, becoming ferrous ions with a radius of 0.69Å instead of 0.59 Å.

As a result of the gamma irradiation, the crystal became larger. This was explained by the fact that more ferrous ions were present at the octahedral sites as a result of gamma irradiation, which increased the lattice parameter and caused more polarization when exposed to an electric field. All Zn^{2+} concentrations showed an increase in the diffusion coefficient following gamma irradiation. This was clarified in terms of how irradiation caused metal ions to move from their initial positions, leaving behind lattice vacancies that increased the diffusion coefficient.

Co-Zn-Mn ferrites structure and diffusion coefficient after gamma irradiation have examined by Hamada et al [16] and Dalal et al [27]. This served as a warning that the cubic structure had a little deformation. The irradiated samples were found to have a higher electron diffusion coefficient. The flaw that was created after gamma irradiation was also visible in the radiation spectra. After exposure to radiation during the initial stage of temperature increase, the activation energy of hopping electrons in reduced. In this system, hopping holes made up the majority of the carries at high temperatures.

$Co - Zn - Ce - Fe_2O_4$ ferrites were the subject of a similar investigation by Ateia et al. [28]. It was discovered that irradiated samples had higher estimated microstrain values than unirradiated samples, while unirradiated samples had larger crystallite sizes. After irradiation, the dielectric constant (ε') also rose. This rise in (ε') was attributable to the Fe^{2+} produced during irradiation as well as the creation of a few vacancies at various depths that served as trapping centers.

Ahmed et al. [29] investigated how gamma irradiation affected the structural and electrical characteristics of the $Mg - Ti - Er_2 - Fe_2O_4$ system. It was discovered that after irradiation, there was a discernible shift in the XRD peaks. This was attributed to the possibility that the $\frac{Fe^{2+}}{Fe^{3+}}$ ratio at the octahedral sites might vary as a result of $\gamma + Fe^{2+} \leftrightarrow Fe^{3+} + e^{-}$. The crystal size decreased as a result of this. The dielectric constant clearly increased, it has also been seen. The anions were shifted away from the closest tetrahedral cations as a result of the displacement, which was thought to cause some distortion to the tetrahedral sites. As the irradiation dose rose, the conductivity increased. This rise in σ was attributable to the hopping process, which caused an increase in the ratio of $\frac{Fe^{2+}}{Fe^{3+}}$ on the octahedral sites. As the irradiation dose was increased, the activation energy values fell.

By using gamma irradiation, Okasha et al. [30] were able to increase the magnetization of $Mg-Mn$ nano ferrite. As a result of ferric ions ionizing into ferrous ions with a larger ionic radius, it was discovered that increasing the lattice constant for the exposed materials occurred. At a higher applied magnetic field of 6kOe, it was discovered that the absence of hysteresis, saturation, remanence and coercivity indicated the presence of super paramagnetic activity. Additionally, irradiated samples had greater saturation magnetization (Ms) values than unirradiated samples. The internal cation disorder and the small particle surface effect were used to explain this phenomenon.

In a study by Karim et al. [31], the impact of gamma irradiation on the distribution of cations, structural composition, and magnetic properties of Ni-Zn ferrites was investigated. It was discovered that the peak intensities were reduced and the peak positions were moved to higher 2θ values.

Additionally, compared to the unirradiated samples, the peak breadth was wider. Lattice constant value dropped following irradiation. It was believed that it was caused by the lattice vacancies that resulted from the spinel cubic structures distortion and deviation following irradiation. The cation distributions showed that the A and B-sites had caused a redistribution of the cations. The production of Fe^{2+} ions at octahedral sites following irradiation was thought to be the cause of the shift in cation redistribution data. It was also noted that after irradiation, there was a rise in the Curie temperature and saturation magnetic moment. It was explained by the incomplete production of ferrimagnetic centers, cation lattice rearrangement and ion-induced disorder.

Cu-Mg-Zn ferrites were made using the sol gel auto-combustion approach by Zhenxing et al. [32]. Investigations have been done into how Cu ions affect electromagnetic characteristics. The ferrite phase may be sintered at temperatures lower than 950^0C thanks to the high sintering

activity of the produced powders, it was discovered. The manufactured samples were discovered. The manufactured samples were discovered to have fine-grained microstructures and good electromagnetic characteristics, making them an ideal material for high performance multilayer chip inductors. Copper content has a big impact on the electromagnetic properties, like dielectric constant, dc resistivity, quality factor, initial permeability, and dielectric loss tangent.

For the first time, using flame spray synthesis (FSS), Vital et al. [33] synthesized $Mg_{0.2}Cu_{0.2}Zn_{0.6}Fe_{1.98}O_{3.99}$, $ZnFe_2O_4$ and $Mg_{0.5}Zn_{0.5}Fe_2O_4$ and powder. It was discovered that the flame method produced crystalline spinel particles with primary particle sizes of 6-13 nm. The size of the particles and crystallites was affected by the precursor, its molarity and the pace of the atomizing gas. Without the use of eny sintering additives, a 2 hour firing at 900^0C resulted in a sintered density of 5.05 g/cm^3. The sintered Mg-Cu-Zn ferrite nano powder compacts had a saturation magnetization of 80 emu g^{-1} and a permeability of μ=600 at 1 MHz.

Microwave hydrothermal synthesis of Cu-Mg-Zn ferrites with PbO addition was studied by Raju et al. [34]. The samples produced at 1600C, a low temperature, were found to have large surface areas with particle sizes ranging from 10 to 20 nm after an hour of treatment. The effects of sintered materials on density, electrical resistivity, permeability at first and saturation magnetization changes were studied, and the findings were compared to those obtained using the conventional ceramic technique. PbO was discovered to enhance electrical resistivity, permeability and sintered density.

In a study by B.M. Sahanashree et al. [35], nanosized $Co_{1-x}Zn_xFe_{2-y}Nd_yO_4$ ferrites were produced using a combustion process. The ^{60}Co gamma ray source was used to irradiated each sample. The phase development of spinel ferrite was confirmed by XRD analysis. Between 12 and 39 nm in size on average, and 15 to 40 nm for samples that had been exposed to radiation.

The dielectric constant and dielectric loss reduced as the frequency increased, but ac conductivity increased. Similar differences in impedance characteristics have been seen with zinc concentration. Electrical conductivity is decreased with the addition of Nd^{3+} and increased in the samples following irradiation. The presence of many electrical responses was suggested by complex impedance spectra.

In the study of M. Veena et al. [36], Ni-Zn-Dy nano ferrite have fabricated using the combustion process. The production of cubic spinel ferrite was verified by the IR spectra and XRD patterns. The lattice parameter changes when Zn^{2+} content increases and Dy substitution decreases. Two zones have shown, respectively, in the graphs of paramagnetic and ferrimagnetic behavior at Curie temperature (TC) at $\log \sigma$ and 1000/T nano ferrites. Paramagnetic regions had higher activation energies than ferrimagnetic regions. It is clear that as Zn^{2+} ion concentration and Dy ion concentration increased, Tc values were pushed to lower temperatures. The magnetic investigation has proven the magnetic characteristics of nanoscale Zn ferrite. In samples with Dy^{3+} ion replacement, it was discovered that the values of magnetic properties decreased. On gamma irradiation, decrease in X-ray density and crystallite size and an increase in lattice parameter were seen. The observed increase in DC conductivity and magnetic characteristics upon irradiation is caused by the distribution of cations at tetrahedral and octahedral sites in the lattice.

3.1 General

There are several synthesis and analysis technique to prepare nanoferrite which explore various properties of nanoscale materials. Among them large categories to prepare nanoferrites are conventional ceramic method and non-conventional method. Most of the researchers use the conventional ceramic method (also called solid state reaction method). We used sol-gel method to prepare nanoferrite samples.

3.2 MATERIALS

By using the sol-gel method, Co-Cu-Cd and Ni-Cu-Cd nanoparticles with the compositional formulas $Co_{0.3}Cu_{0.2}Cd_{0.5}Fe_2O_4$ and $Ni_{0.3}Cu_{0.2}Cd_{0.5}Fe_2O_4$, respectively, have been prepared. The analytical grade of $Cu(NO_3)_2.3H2O$, $Co(NO_3)_2.6H_2O$, $Ni(NO_3)_2.6H_2O$, $Cd(NO_3)_2.4H_2O$, $Fe(NO_3)_3.9H_2O$ used as raw materials. The material stoichiometric compositions are dissolved in pure ethanol.

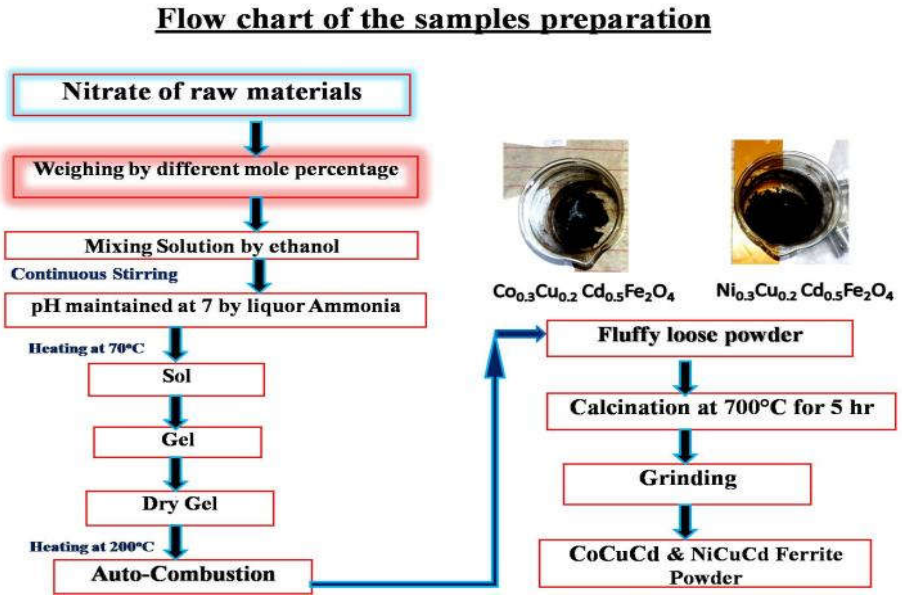

Fig: 3.1 Flow chart of the samples preparation.

The aforementioned solution is continuously stirred by a magnetic stirrer at 70°C till the gel formation. Using liquid ammonia, the pH of the mixture is kept at 7. The produced gel is annealed for 5h at 200°C. The gel self-ignites during this heating, and it is allowed to burn out completely to produce a fluffy loose powder.

The remaining organic components in the sample are removed by splitting the resulting powder into two portions and heating each portion for five hours at 600 ºC. The samples are compressed into circular disc-shaped pellets for use in electric measurements, and silver paste is put on the opposite faces to create a geometry of parallel plate capacitors with ferrite material acting as the dielectric medium. Co-Cu-Cd and Ni-Cu-Cd nanoferrite samples were introduced into the ^{60}Co gamma irradiator with energy 1.3325 MeV core at varied doses (1Mrad and 3Mrad) for gamma irradiation studies. Each sample was just briefly exposed to neutrons during the process. Standard was carried out individually for 60 seconds in the BAEC TRIGA MARK II research reactor's (BTRR) rabbit irradiation system at 250 kW reactor power and when it was going to carry out prolong irradiation. All of the samples and standards were placed in a single radiation vial, and they were all exposed to radiation simultaneously. The irradiation vial containing the samples, standards, and Al-Au foil was exposed to radiation in the BTRR rabbit-system for 7 minutes at 2.4 MW power. To lessen the radiation risk and give the short-lived radionuclides time to decay, the irradiated vial was stored in a lead container for two days after radiation exposure. The Bangladesh Atomic Energy Commission's (BAEC) Institute of Nuclear Science and Technology (INST), AERE, Savar is home to the radiation source.

The X-ray diffraction (XRD) patterns of the generated samples were recorded using a D8 advance diffractometer for X-rays employing CuK radiation (λ = 0.15418 nm) both before to and during exposure to neutron (η) and gamma (γ) radiation. This device was utilized in the Process Development Center of the BSCIR, located in Dhaka. Using the Debye Scherrer formula, the average particle size (L) was determined. $L = 0.89\lambda/\beta\cos\theta$ [37], where μ is the

matching diffraction angle, λ is the radiation wavelength, L is the particle size in nanometers (nm), and β is the full width at half maximum. A Micro Sense EV9 Vibrating Sample Magnetometer (VSM) was used at the Material Science Division of the Atomic Energy Commission (AEC), Dhaka, to study the magnetic properties of the current samples.

At room temperature, measurements of electrical and dielectric transport characteristics were made in the frequency ranges of 20Hz and 10MHz, and silver paste was applied to both of the pellet's surfaces, and their electrical conductivity was evaluated, additionally, computer-controlled methods were used to measure impedance. Wayne Kerr the pellet's two surfaces were coated in silver paste, and their appropriate electrical contact was checked.. At the postgraduate lab of Department of Physics, CUET, impedance measurements were done using a computer-controlled Wayne Kerr Precision Impedance Analyzer (6520A, UK). From room temperature up to 800K at various frequencies, the studied samples and dielectric loss ($tan\delta$), ac electrical resistivity and dielectric constant (ε') have been measured using the RLC Bridge (Hioki Model 3531, Japan).

3.3 EXPERIMENTAL TECHNIQUES

3.3.1 GENERAL

The frequency and lattice parameters dependent dielectric characteristics of ferrite nanoparticles are measured using simple experimental approaches that are described in this chapter. To characterize the samples, X-ray diffraction (XRD) was employed. A vibrating Sample Magnetometer (VSM) was used to measure DC magnetization. Two probe approaches were used to measure the transport parameters utilizing the impedance analyzer. An impedance analyzer and a specially designed sample holder were used to conduct the dielectric tests. Impedance and modulus spectroscopy in-depth examination are also done.

3.3.2 TRIGA MARK-II RESEARCH REACTOR

TRIGA (Training, Research, Isotope production, General Atomics) MARK II research reactor at AERE, Savar of Bangladesh Atomic Energy Commission (BAEC) was used for neutron irradiates of the nanoparticle samples for this investigation. As the sole nuclear reactor in the nation, BAEC TRIGA Research Reactor (BTRR) is only one of this kind in Bangladesh (Fig. 3.2). It is a research reactor in the tank form used for training, research, and isotope synthesis.

Fig. 3.2: Partial view of the TRIGA MARK II Research Reactor of BAEC.

Since its first use, the reactor has been put to use in a variety of research and practical applications, including neutron activation analysis (NAA), neutron radiography, neutron scattering investigations, radioisotope production, human resource development, and education. It should be noted that BTRR is a crucial facility for training the workforce that will be required for the nation's nuclear power program. The maximum continuous thermal power output of the BTRR is 3MW (Fig. 3.3).

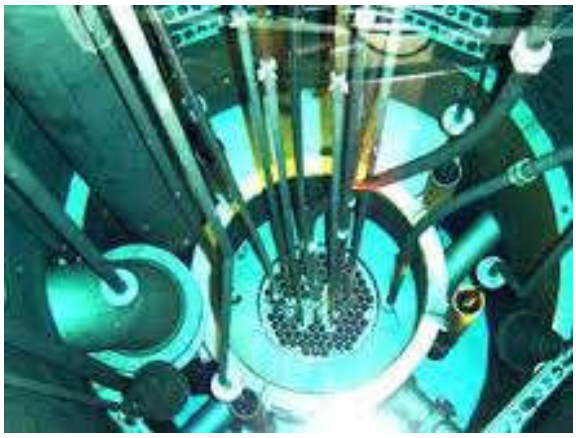

Fig 3.3 Inner view of the TRIGA MARK II Research Reactor.

Fig. 3.4 Pneumatic transfer (Rabbit) system for neutron irradiation of the samples.

Each sample was individually exposed to neutron radiation for 60 seconds in the rabbit irradiation system of thermal flux: 1.50×10^{12} $cm^{-2}s^{-1}$ and $6.10\times10^{13}cm^{-2}s^{-1}$ at 250 kW and 2.4 MW, respectively, in the reactor power of the BTRR at the AERE, Savar of Bangladesh Atomic Energy Commission (BAEC) (Fig. 3.4). To lower the risk of radiation, the irradiated vial was kept for two days after irradiation in a lead container. The nucleus is the sole part of an atom with which a neutron interacts. There are two different ways that nuclear interaction can happen: either through inelastic interaction, in which the neutron reacts with the nucleus and causes nuclear interaction (such as capture, (n,p) fission, or other reactions, etc.), or through

elastic interaction, in which the neutron hits the nucleus but only transfers some of its momentum and kinetic energy to it.

Fig.3.5 Depicts of the ^{60}CO gamma irradiator setup that was employed in this study.

Co-Cu-Cd and Ni-Cu-Cd nanoferrite samples were introduced into the ^{60}Co gamma irradiator with energy 1.3325 MeV core at varied doses (1Mrad and 3Mrad) for gamma irradiation studies at the Institute of Food and Radiation Biology (IFRB), AERE, BAEC (Fig. 3.5). The quantity of energy (from any sort of ionizing radiation) deposited in any medium, such as water, tissue, or air, is known as the radiation-absorbed dose (rad). An absorbed dosage of 1 Rad denotes that as a result of radiation exposure, 1 gram of material absorbed 100 ergs of energy, which is a negligible but quantifiable amount. Radiation absorbed dose is measured in terms of the rad, which is defined as 1 Rad = 0.01 Gy = 0.01 J/kg.

3.3.3 X-RAY DIFFRACTION ANALYSIS

Significant information on the crystal structure is provided by the X-ray diffraction (XRD). Utilizing Cu-K radiation with a wavelength of λ= 0.15418 nm, an X-ray diffractometer was used to characterize the structural composition. Thousands of granules in the powder are oriented randomly. In some of the grains with random orientations, it is expected that the

majority of the different atomic planes will be parallel to the surface. scanning in respect to different atomic spacings and at different angles. On a sample stage, a powdered sample was placed for X-ray exposure.

The X-ray powder diffractogram can provide the following details:

- The prepared samples' high quality and confirmation.
- The reflections inter-planer spacing (d).
- The reflections intensities.
- The lattice type and unit cell dimensions.

To identify the diffracted X-rays, an electronic detector was placed on the sample's opposite side from the X-ray tube and rotated the sample over a range of Bragg's angles. The detector counted the X-rays it found in counts/sec and sent the data to the computer, while the goniometer monitored the angle (θ).

Using a step size of 0.01^0, the XRD patterns of every sample have compiled over 2θ range of 15^0–60^o for phase identification and preferred orientations. After the sample was scanned, the X-ray intensity (counts/sec) was plotted versus the angle theta (2θ). The Bragg's rule, which states that $n\lambda = 2d\ sin\theta$, where n is the order of diffraction, was then used to convert each diffraction peaks 2θ to d-spacing [38].

Utilizing the procedure, for every peak in every sample, the lattice parameter was calculated [39]:

$$a = d\sqrt{h^2 + k^2 + l^2} \quad \ldots\ldots\ldots\ldots (3.1)$$

where the crystal plane indices are h, k, and l. The Nelson-Riley approach was applied to calculate the precise lattice parameter for each sample. The Nelsion-Riley function *F (θ)* is provided as [40]:

$$F(\theta) = \frac{1}{2}\left[\left(\frac{cos^2\theta}{\sin\theta}\right) + \left(\frac{cos^2\theta}{\theta}\right)\right] \ldots\ldots\ldots\ldots (3.2)$$

Plotted against F (θ) are the lattice constant 'a' values for each peak in the sample. The precise lattice parameter 'a_o' is then obtained using the least square fit approach. The true lattice parameter can be found at F (θ) = 0, which is the intersection of the y-axis with the least square fit straight line.

3.3.4 WAYNE KERR PRECISION IMPEDANCE ANALYZER

For precise measurement and research of impedance in a range of electrical devices, including circuits and components, as well as non-electronic materials, the Wayne Kerr impedance analyzer is an invaluable instrument. Additionally, it is a helpful tool for materials research and development (both for electronic and non-electronic materials) and circuit design and development.

- Accurate measurement across a broad impedance range and 20 Hz–15 MHz frequency range;
- Effective impedance analysis features;
- Simple operation and flexible PC connectivity.

The coil's complex impedance [42] can be represented as follows.:

$$Z = R + jX;$$

where the R denotes the resistive part and the reactive part is X.

3.3.5 MAGNETIC HYSTERESIS MEASUREMENT

Through the application of force in a field gradient, saturation magnetization was computed for the ferrite specimen. The instrument used to measure it was the vibrating sample magnetometer (VSM) (Micro Sense, model EV9) shown in Fig. 3.6. Measuring the electromotive force a magnetic sample produces when it vibrates at a constant frequency while being surrounded by a static, homogeneous magnetic field is the foundation of the VSM theory.

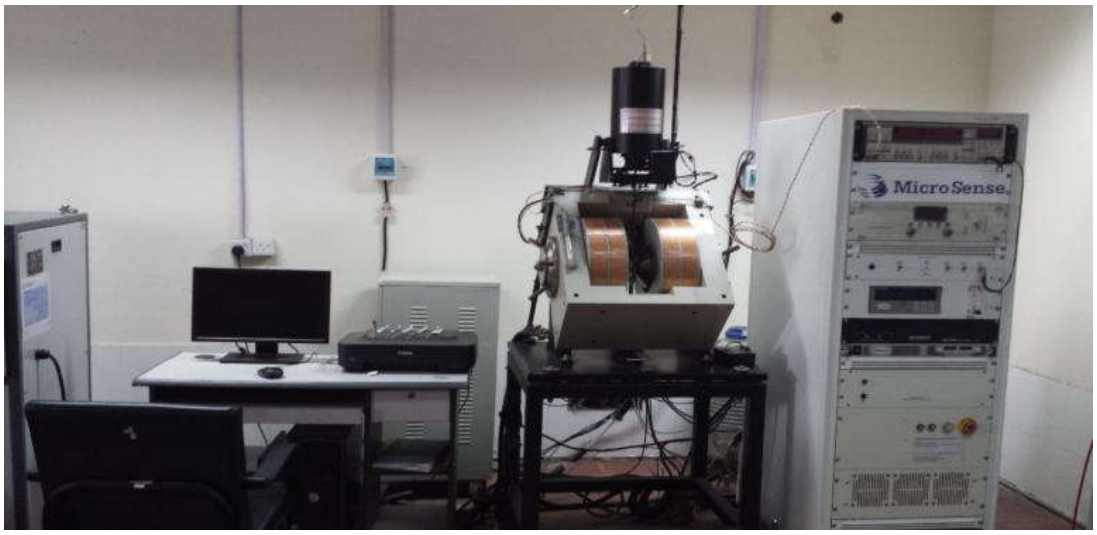

Fig. 3.6 Vibrating Sample Magnetometer (VSM) at the Atomic Energy Commission, Dhaka.

To prevent movements inside the sample container, a small portion of nanocrystalline materials (10–11 mg) was weighed and manufactured. The VSM was run at 82 Hz vibration frequency up to 3 T. A Ni standard (spherical) with a known magnetization (Ms = 6.92 emu at 5 kOe) was used to calibrate it. With the temperature chamber in place, the EV9 VSM can reach fields of up to 21.5 KOe at a sample spacing of 5 mm. Up to one Tesla of fields might be delivered by the VSM. The VSM could identify magnetic moments as small as 0.5 emu.

3.3.6 DIELECTRIC MEASUREMENTS

There are different kinds of polarizations, and each one has a unique physical mechanism that may be explained. Electronic, ionic, and orientation are the three fundamental categories of polarization. The atoms' electrons are slightly displaced from their nuclei in the presence of an insulator, or external electric field, which causes electronic polarization and the production of induced dipole moments. When atoms in a molecule do not exchange electrons symmetrically, the electron clouds will flow eccentrically toward the direction of the atom that is more strongly attached. The ions then pick up charges with the opposite polarity. Under the influence of an external electric field, these net charges will typically cause the ions' equilibrium positions to shift. A second type of induced dipole moment is produced by the displacement of charged ions or clusters of charged ions relative to one another. There are also persistent dipole moments that exist even when there is no external electric field, it indicates the ionic polarization of the oppositely charged partners of molecules. Such dipoles encounter a torque in an electric field that causes them to naturally point in the field's direction. An orientation (or dipole) polarization may result as a result. These three polarization mechanisms are caused by locally bonded charges in atoms, molecules, or the structure of solids. In addition to all of these, charge carriers typically exist and can go a fair distance across the dielectric.

Wayne Kerr impedance analyzer (6500B) under computer control was used to measure dynamic (electrical and dielectric) transport parameters. To get rid of any contamination from other oxides that might have formed on the surface during sintering, the pellet-shaped samples underwent rigorous polishing. Silver paint was applied to both of the pellets' surfaces as a contact material. The dielectric and ac conductivity, as well as the impedance (real and imaginary components directly), were measured at room temperature using the Wayne Kerr impedance analyzer. Using the formula, the real portion of the dielectric constant was measured [43-45]:

$$\varepsilon' = \frac{Cd}{\varepsilon_0 A} \quad \ldots\ldots\ldots\ldots\ldots (3.3)$$

where C denotes the pellet capacitance in Farad, d express the pellet thickness in meter (m), A represents cross sectional area of the selected paint region in m^2 and ε_0 the free space permittivity constant.

Utilizing relation, the imaginary portion of the sample's dielectric constant (ε'') was computed: $\varepsilon'' = \varepsilon' \tan\delta$; where tanδ denotes the dielectric loss tangent.

The relation was used to compute the ac conductivity, $\sigma_{ac} = d/(A \times R_{ac})$; here R_{ac} for the ac resistance. The majority of materials' electrical conductivity can be characterized as: $\sigma(\omega, T) = \sigma_{dc}(T) + \sigma_{ac}(\omega, T)$; where The sole factor that influences σ_{dc} conductivity is temperature. The second σ_{ac} ac component, which depends on both temperature and frequency, is called ac conductivity. The empirical formula represents the frequency-dependent ac: $\sigma_{ac}(\omega, T) = A\omega^n$; where A and n are constants that are temperature- and composition-dependent; n defined dimensionless, whereas A for units of σ_{ac}.

3.3.7 IMPEDANCE SPECTROSCOPY

Investigating the electrical properties of the complex oxides can be done well with the help of complex impedance spectroscopy. The technique's principal benefits include i) It entails comparatively straightforward electrical measurements that are easily mechanized, ii) Any electrodes can be used to carry out the measurements, iii) It is frequently possible to link the sample's composition, microstructure, defects, dielectric properties, chemical reactivity, etc. with the outcomes and iv) In the majority of polycrystalline samples, the resistance of the grain borders and that of the grains may be easily distinguished. In a Wheatstone-bridge-style device (impedance analyzer or LCR meter) used for AC measurements, the resistance R and capacitance C of the sample are measured and balanced against variable resistors and

capacitors. Impedance spectroscopy measures both electrical properties by measuring the phase difference (θ) and the impedance |Z| between the current and the voltage as a function of frequency for the given sample. The impedance plot, a complex plane known as the impedance plane, is used to analyze the data by graphing the imaginary component of the impedance $Z' = |Z|cos\theta$ as well as the real part $Z'' = |Z|sin\theta$. The equivalent circuit is examined using a linear scale impedance plot as shown below. A pure capacitor's impedance plot is a straight line parallel to the imaginary axis, but a pure resistor's is a point on the real axis. The relation below can be used to express the impedance of the parallel RC combination:

$$Z^* = Z' - jZ'' = \frac{R}{(1+j\omega RC)}$$

One obtains after simplification, $(Z' - R/2)^2 + Z''^2 = (R/2)^2$,

This provides the equation for a circle whose center is at (R/2,0) and whose radius is R/2. Because of this, a semicircle with a radius of R/2 will be produced by plotting Z' vs Z″ (as a parametric function of). The simple circuit's time constant is given by the formula $t = RC = \frac{1}{\omega_m}$. This is consistent with the sample's relaxation duration, and the characteristic frequency is located at the semi-circle's peak. Three distinct patterns can be seen in the impedance curve of a perfect polycrystalline sample: a low frequency arc resulting from the behavior of the grain boundaries, a low frequency spike related to the electrode effect, and a high frequency arc corresponding to the bulk property of the sample.

3.3.8 MODULUS SPECTROSCOPY

The study of complex modulus spectroscopy is a powerful and practical technique in materials research that offers crucial details on the distribution parameters of different nanoregions in nano-crystalline materials, including grain, grain boundary, and electrode interface. By graphing the modulus at various frequencies in a complex plane, distinct

mechanisms involved in the relaxation and ac conduction process may be elucidated. This method is also particularly successful in differentiating the contributions of the grain and grain boundary effect. Additionally, the separation of components with identical resistance but varied capacitance can be accomplished with the help of a modulus spectroscopic plot. The electrode effect is reduced, which is another benefit of the electric modulus formalism. Complex electric modulus formalism has been selected for the reasons listed above. Studies on dielectric relaxation using the complex modulus M' formalism have been done. Impedance measurements were used to derive the real and imaginary components of the electric modulus in line with the relationship:

$$M' = {\varepsilon'}/{(\varepsilon'^2 + \varepsilon''^2)} = \omega C_0 Z'' \text{ and } M'' = {\varepsilon''}/{(\varepsilon'^2 + \varepsilon''^2)} = \omega C_0 Z' \quad \ldots\ldots\ldots (3.4)$$

CHAPTER 4: RESULTS AND DISCUSSION

4.1 GENERAL

The study, results are shown in this part along with discussion of their significance. Within the framework of the study goals, the findings are interpreted such as XRD as well as Rietveld Refinement, magnetization, dielectric Studies, Modulas Studies and Dynamic Conductivity before and after gamma and neutron irradiation. Every segment is circumstantially discussed with scientific reference.

4.1.1 RESULTS AND DISCUSSION OF $Co_{0.3}Cu_{0.2}Cd_{0.5}Fe_2O_4$

4.1.2 STRUCTURAL ANALYSIS

The XRD patterns for $Co_{0.3}Cu_{0.2}Cd_{0.5}Fe_2O_4$ with and without neutron and gamma irradiation are shown in Fig. 4.1(a) and Fig. (b). The single phase of spinel is seen in both of these figures for every sample. The decrease in the (400) and (511) peaks relative intensity have been found for the gamma and neutron irradiated samples. In contrast, increase in the (222). (440) and (311) peaks relative intensity have been found for the same samples.

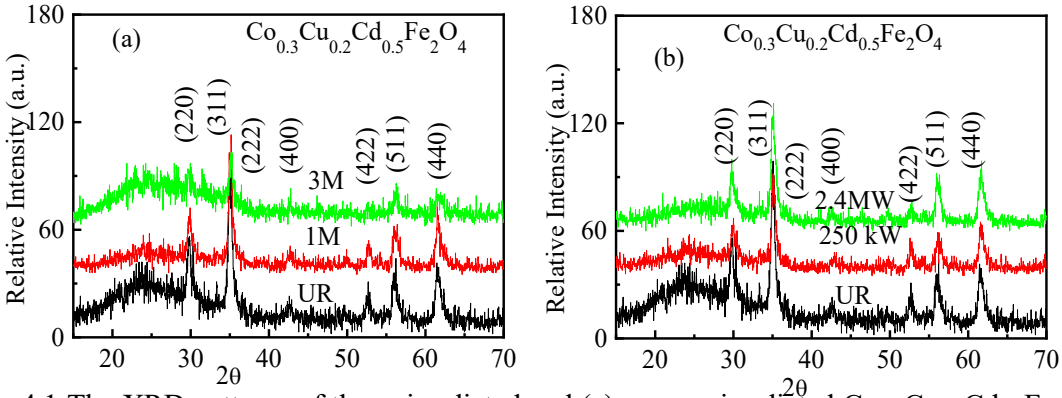

Fig. 4.1 The XRD patterns of the unirradiated and (a) gamma irradiated $Co_{0.3}Cu_{0.2}Cd_{0.5}Fe_2O_4$ and (b) the neutron irradiated $Co_{0.3}Cu_{0.2}Cd_{0.5}Fe_2O_4$ samples.

A comparison of these results shows that (440) peaks intensity is less than (311) peaks while becoming denser after the irradiation process. The decrease is also observed in the case of

(400), (440) and (220) peak intensities. All of the samples confirm the FCC structure in the patterns of XRD without any secondary phase. The materials under investigation are shown in Table 4.1 along with their average crystallite size (DXRD), lattice constant (A), measured density (ρm), X-ray density (ρx), specific surface area (S), and microstrain (η). Because of the growth of grain boundary disorder at the ordered expense of crystallite portions, the crystallite sizes decrease with increasing irradiation dosage. On the other hand, an increase in the crystallite sizes has been observed for the Ni-Cu-Cd ferrites due to the irradiated energy role on the unit cells. Also, a slight increase is noticed in the lattice constants between two irradiated ferrites samples for the interacted γ-rays dominant effect with external electrons from iron where the conversion of larger size Fe^{2+} (0.76 Å) from the smaller Fe^{3+} (0.67 Å). Similar reports have been published frequently [46-48]. The inverse trends are found in the X-ray density (ρ_x) for the increasing dose of irradiation which is accepted logically due to the inverse proportional relation between ρ_x and lattice volume. The behavior of measured density is the same as the crystallite size for the Co-Cu-Cd ferrites and tends to decrease as irradiation dose increase whereas the increase is found for other ferrites [49]. In comparison, opposite behavior is found for the case of specific surface area and porosity rather than their definition expectations. However, the microstrain of Co-Cu-Cd samples is estimated from the equation of Williumson-Hall [50] and found to follow the irradiation dose. As imperfections in crystallite lattice, dislocations, including vacancies, stacking faults etc. give rise to the microstrain, so the increasing microstrain denotes the larger disordered regions of grain boundary and smaller well-ordered regions of grain in the present investigation.

In some literatures, a similar trend for the lattice constant had been reported [51, 52]. Furthermore, the shifting to the greater values of 2θ is evident from the irradiated peaks and their intensities become lower as shown in Fig. 4.1. The peaks width becomes broader due to the irradiation dose on the samples.

Table 4.1 depicts the decrease in lattice constant due to the irradiation dose which occurs for the generation of vacancies that causes distortion along with deviation from the structure of cubic spinel [53]. The reason might lie in the compressive strain produced by the irradiation as indicated by the peak positional shift to a higher value of 2θ and structural disorder in lattice generation as indicated by the peak broadening with reduced intensities [54].

The similar increasing nature of ρ_x and lattice constant are attributed to the mass increase over the lattice constant increase. The investigated values of lattice constant, particle size (t) and X-ray density (ρ_x) for all samples with irradiation and without irradiation by gamma rays are listed in Table 4.1 and those of neutron are listed in Table 4.2 for the purpose of comparison. The N-R function plot for gamma-irradiated and neutron-irradiated samples are shown in Fig. 4.2.

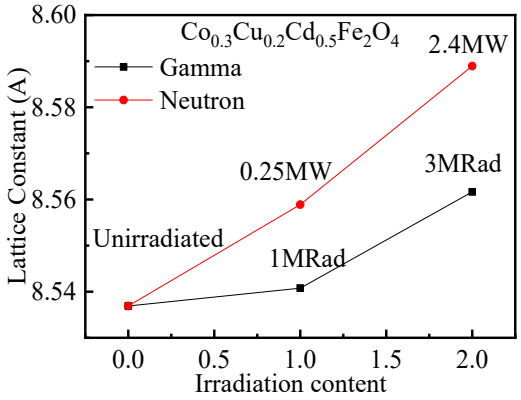

Fig. 4.2 Typical N-R function of the unirradiated and irradiated sample of gamma and neutron irradiation of $Co_{0.3}Cu_{0.2}Cd_{0.5}Fe_2O_4$

The reason for the decrease in particle size is the penetration of energy-rich ions along ion beam trajectory by the irradiation and lead-modified material through the pushing of the atoms from normal positions of them and splitting the molecules into many pieces. The generation of defects is turned by losing the energy of heavy ions and thus results in partial amorphization in the decrease of average particle size [55]. Thus, the migration of ionic interstitial positions attributes the reorganization of cations among A sites and B sites respectively. The irradiation

by gamma and neutron interacts with site preferences of ions by giving rise to more ionized Fe^{2+} to Fe^{3+} transition as

$$Fe^{2+} + \text{irradiation} \longrightarrow Fe^{3+} + e^{-} \quad \ldots\ldots\ldots\ldots \quad (4.1)$$

This process of irradiation will help to the valence change between Fe^{2+} an Co^{3+} as

$$Fe^{3+} + Co^{2+} \longleftrightarrow Fe^{2+} + Co^{3+} \quad \ldots\ldots\ldots\ldots\ldots \quad (4.2)$$

Thus, this process leads to the particle size and lattice parameter change due to the irradiation [56, 57]. Hence it can be said from Table 4.1 that the variation of particle size by the irradiation type occurred for the vacancy formation of cluster pairs in the sample through neutron irradiation and the exchange of valency in irradiated samples of gamma and neutron. The ions of the compound are expected to be affected by the neutron irradiation and outermost shell electrons are not affected by the process of irradiation. Accordingly, the vacancy pairs of cluster formation get a favor. In the samples with neutron irradiation, Fe_2O_4 small intensities appeared as a new phase. Moreover, the formation of vacancy cluster pairs is also enhanced by the disappearing planes such as 222 and 533. From a deeper perspective, it is evident from the XRD of both cases that irradiation through neutron shifts planes more than that of gamma irradiation. Thus, it confirms the ionization and displacement type damage production by the radiation in spinels [58]. Due to the disorder in cation, both octahedral vacancies and tetrahedral vacancies of cations are possible however octahedral vacancies of cations are proposed only for the inverse spinels [59, 60]. The generation of cation vacancies is caused by the irradiation through fast neutron necessarily for neutral charge maintenance. There is a possibility of spinel inversion increment and lattice parameter decrement by neutron irradiation [61]. The outcomes of the present works have good agreement with the possible reflection of

irradiation as the lattice parameter is found to decrease along with the increasing inversion parameter by the neutron irradiation on the samples.

4.1.3 RIETVELD REFINEMENT AND CATION DISTRIBUTION

The XRD data are further analyzed using the Rietveld refinement technique, and the output patterns are shown in Fig. 4.3, which contains the patterns of samples both before and after gamma and neutron radiation.

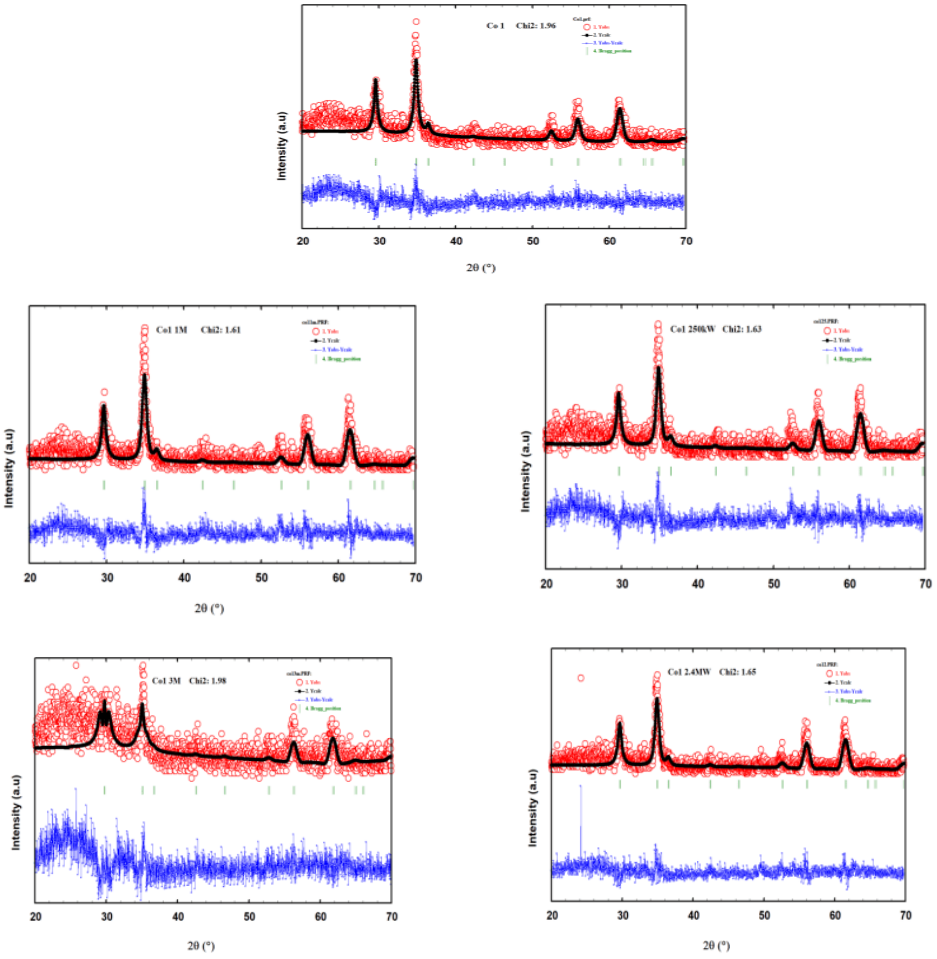

Fig. 4.3 The Rietveld refinement output patterns of the unirradiated and irradiated samples of gamma irradiation and the neutron irradiation of the $Co_{0.3}Cu_{0.2}Cd_{0.5}Fe_2O_4$.

Rietveld refinement is the process of fitting experimentally obtained data with the calculated data. In this investigation, the refinement of Rietveld method is performed with the help of Full Prof. suit software.

The symmetry is chosen as Fd-3m which is the basic space group for cubic ferrites. The whole system is analyzed under the peak function of pseudo-voigt. The atomic position of oxygen is taken as an open parameter whereas the remaining is taken as fixed parameters.

The least-square formulism has been introduced for the pattern-fitting process. The refinement process continues till the value of χ^2 becomes as low as possible. It is well known that, the value of χ^2 less than 4 is considered as good fitting while the value of the same parameter less than 1 is considered as best fitting. Hence, the refinement in the present investigation is performed till the value of χ^2 comes down below 2. The final χ^2 values of unirradiated, gamma irradiated and neutron irradiated samples are 1.96, 1.61, 1.98, 1.65 and 1.63, respectively.

Table 4.1: Cation distribution of the $Co_{0.3}Cu_{0.2}Cd_{0.5}Fe_2O_4$ unirradiated and irradiated samples for gamma and neutron irradiation.

Samples		A sites	B sites
Before irradiation		$Co_{0.284}Cu_{0.152}Cd_{0.329}Fe_{0.236}$	$Co_{0.016}Cu_{0.048}Cd_{0.171}Fe_{1.764}$
After gamma irradiation	1 M	$Co_{0.129}Cu_{0.088}Cd_{0.497}Fe_{0.286}$	$Co_{0.171}Cu_{0.112}Cd_{0.003}Fe_{1.714}$
	3 M	$Co_{0.149}Cu_{0.095}Cd_{0.481}Fe_{0.275}$	$Co_{0.151}Cu_{0.105}Cd_{0.019}Fe_{1.725}$
After neutron irradiation	250 kW	$Co_{0.149}Cu_{0.044}Cd_{0.478}Fe_{0.330}$	$Co_{0.151}Cu_{0.156}Cd_{0.022}Fe_{1.670}$
	2.4 MW	$Co_{0.150}Cu_{0.043}Cd_{0.476}Fe_{0.331}$	$Co_{0.150}Cu_{0.157}Cd_{0.024}Fe_{1.670}$

These obtained values of χ^2 are directly labeled on the output pattern as seen in Fig. 4.3. Hence, the refinement processes of all samples show best-fitted curve between observed and calculated

data. Below the fitted curves, the Bragg position and the variation between the predicted and observed values are shown individually. The output data of Rietveld refinement process has been used to determine the cation distribution of all investigated samples including irradiated and without irradiated ferrites and listed in Table 4.1. From Table 4.1, it is evident that Co, Cu and Cd go to the A site more than B site in the case of samples before irradiation. But, as the irradiation applied on the samples, the preferences of Co and Cu changes and they moves towards the B sites whereas Cd attains its general occupation in A site only. There is no change in the case of Fe also. The distribution of cations among two different sites can be understood on the basis of magnetic moment of ions. The magnetic moments of Fe^{3+}, Ni^{2+}, Cu^{2+} and Cd^{2+} are 5 μ_B, 2 μ_B, 1 μ_B and 0 μ_B respectively. Due to the differences in the magnetic moment, preferences between these cations have been changed towards the sites. These site occupancies are in good agreement with the magnetization analysis as discussed below.

4.1.4 DC MAGNETIZATION

Fig. 4.4 displays the change in magnetization (M) in Am^{-1} with respect to the applied magnetic field (H) in T, up to a maximum of 1×10^4 T. The data comprises both irradiated and unirradiated samples at room temperature by gamma and neutron radiation. The usual tendency of ferrite is to exhibit a rise in magnetization, which is shown by a growing magnetic field.

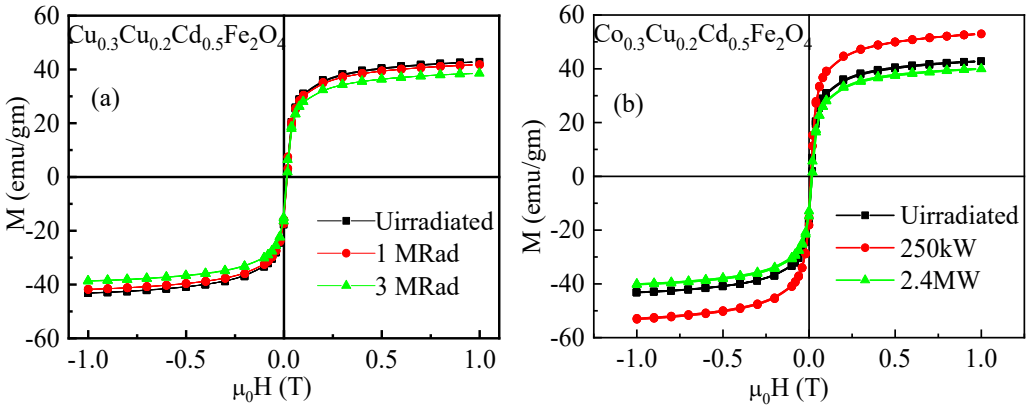

Fig. 4.4 Variation of M with H for different compositions of $Co_{0.3}Cu_{0.2}Cd_{0.5}Fe_2O_4$ before and after (a) gamma and (b) neutron irradiation by different dose.

The origin of magnetic properties as well as magnetism essentially results from the electron motion of spin and orbital, electrons magnetic moment and atomic and ionic magnetic moment. The reason for the atomic magnetic moment is the electrons motion in its own orbits and the motion of its spin (Fig. 4.5).

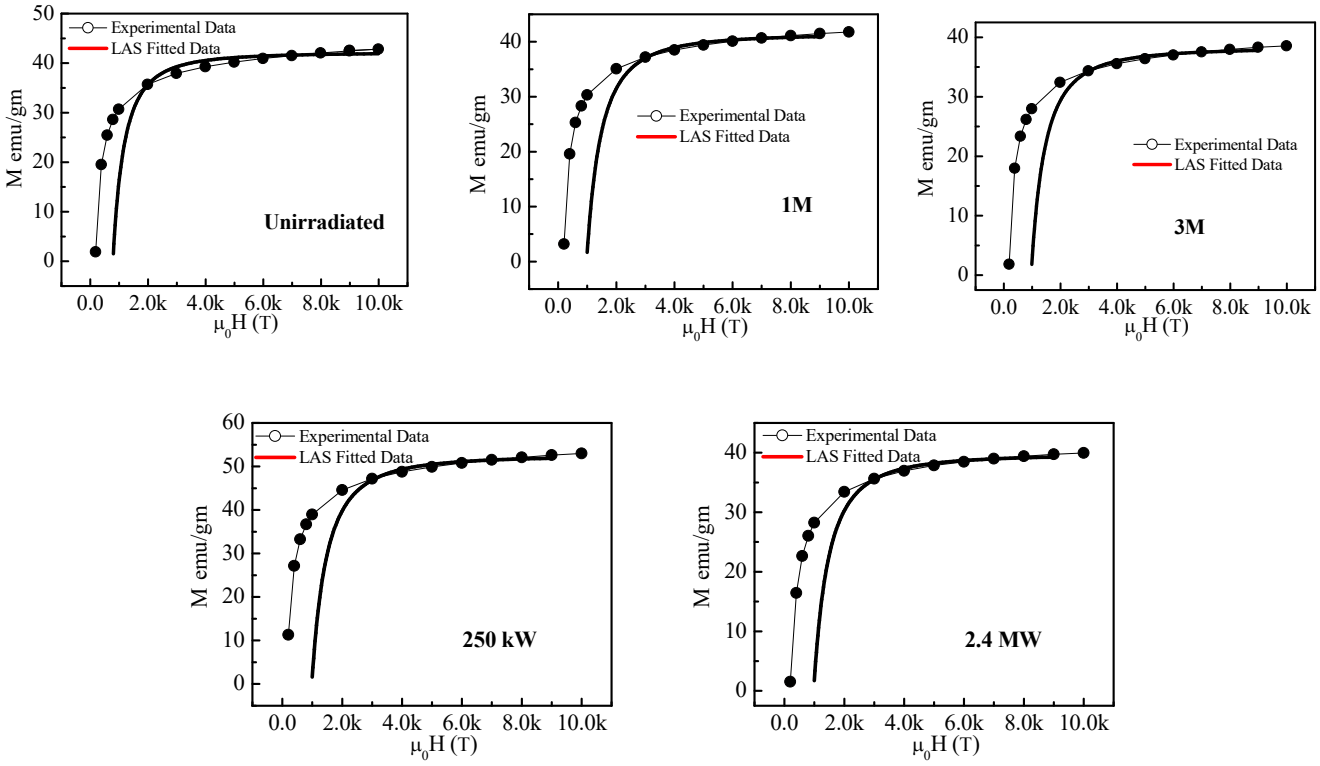

Fig. 4.5. Variation of M with H for different compositions of $Co_{0.3}Cu_{0.2}Cd_{0.5}Fe_2O_4$ before and after (a) gamma, (b) neutron irradiation by different dose and (c) LAS fitted curves for every samples.

The increasing nature of M is observed till to value of μ_0H as 0.25 T and slow rise is observed beyond that and finally attains saturation. The determination of saturation magnetization M_s is done by extrapolating magnetization plots for $1/(\mu_0H) = 0$. Depending on the distribution of cation and exchange interaction, this typical behavior of M_s with the content of Cu^{2+} can be explained. It is well known that site preference of cations influences the properties of magnetic ferrites. The ionic competition of ferromagnets such as Fe^{3+} (5 μ_B), Ni^{2+} (2 μ_B), Cu^{2+} (1 μ_B),

and Cd^{2+} (0 μ_B) preference towards A and B sites could be the cause of the magnetic properties of the synthesized samples. The distribution of cations among A and B site has been obtained from the Rietveld refinement and listed in Table 4.2. Belavi et al [62] and Hemeda [63] also reported similar results. Moreover, improved magnetic properties are expected for ferrites samples due to being a Jahn-Teller ion, Cu leads to the enhanced distortion of lattice which probably produces larger strain in lattice and thus attributes magnetic improvement [64]. The coercivity of the M vs H curve is found very low for synthesized samples and thus confirming the nature of soft ferrites for investigated samples.

Table 4.2: LAS fitted parameters for the unirradiated and irradiated samples of the $Co_{0.3}Cu_{0.2}Cd_{0.5}Fe_2O_4$ for gamma and neutron irradiation.

Irradiation type	Dose	M_s, emu/gm	B, μT
Before irradiation		42.15276	614008.2
Gamma Irradiation	1 M	41.43421	959628.2
	3 M	38.22124	925851.6
Neutron Irradiation	250 kW	52.51672	969752.2
	2.4 MW	39.73691	954970.7

It has been discovered that the M_s lags behind the bulk ferrites' equivalent values. The values of M_s decrease because of the presence of the morphological core shell, which has aligned spins in the ferrimagnet's core and a surface layer similar to spin-glass. Therefore, the disorder is caused by broken super exchange bonds, canting of the surface layer's spins, and atomic symmetry of an unlike local type closer to the surface layer, which results in a reduced value of M_s for the nanocrystals.

As the super exchange interactions are present in the ferrites, the above effects are dominant especially. Thus, the interaction of A-B exchange is reduced and causes subsequent decrease in the values of M_s for all investigated samples of Co-Cu-Cd nanoferrites.

4.1.5 DIELECTRIC STUDY

Frequency Dependence of The Real Part of The Dielectric Constant

Fig. 4.6 displays the fluctuation of the real component of the dielectric constant (ε') for $Co_{0.3}Cu_{0.2}Cd_{0.5}Fe_2O_4$ nanoferrites, which includes both unirradiated and irradiated gamma and neutron samples. The dispersion behavior has been observed for the ε' at the frequency range of 20 Hz to 1 kHz or lower range and becomes dependent on frequency almost at both temperatures of annealing. At the range of higher frequency, ε' decreases more sharply than the lower range of frequency. This can be observed for both types of irradiation processes. The lower values of ε' is actually displaying the lower loss in dielectric materials which plays an important role in the case of application. Other researchers also observed the similar behavior [65-71].

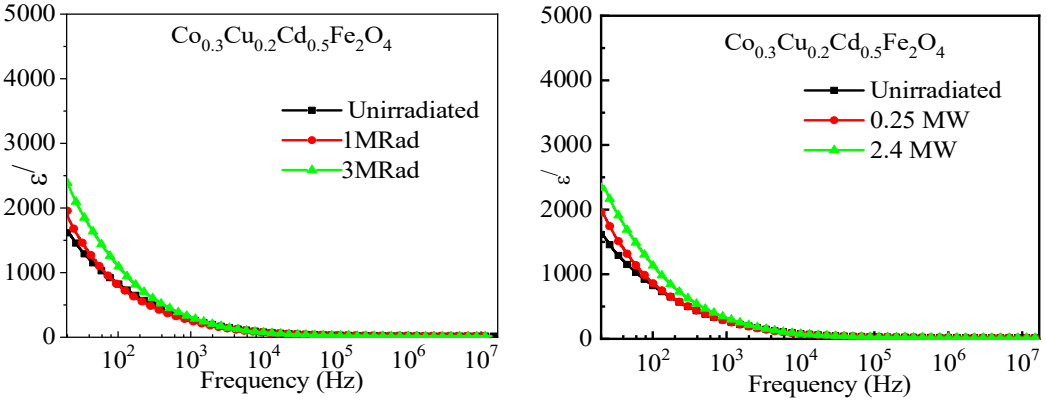

Fig. 4.6. Show the frequency dependence of the real part of the dielectric constant (ε') at room temperature for $Co_{0.3}Cu_{0.2}Cd_{0.5}Fe_2O_4$ nanoparticles before and after gamma and neutron irradiation.

The initial decrease of ε' is rapid by the increasing frequency and this is not followed at the higher frequencies which simplifies the high dispersion in the lower region of frequency as evident in the previous reports [72-73]. The observed behavior is explained depending on the conduction mechanism which governs the space charge polarization and dielectric polarization of ferrites [74]. The hopping of electrons takes place at the favorable lower field of applied frequency. Therefore, large values of ε' is occurs at low frequencies. Along the applied electric field direction, local displacement of Fe^{3+} to Fe^{2+} electron exchange induces ferrites polarization. The dielectric constant becomes static with smaller values due to the inability of exchange electrons to align toward the alternating field beyond a specific frequency [75-79]. Fig. 4.6 also reveals a slight increase in ε' after both types of irradiation process. In a view of explanation, the interaction between matter and gamma rays / matter and fast neutron are the cause for that slight decrease. These interactions can be written as,

$Fe^{3+} + \gamma \rightarrow Fe^{2+} + e^{-}$ …… (4.3)

$Fe^{3+} + {}_0n^1 \rightarrow Fe^{2+} + \text{Energy}$ …… (4.4)

This interaction creates ferrous ions at the B sites and increases the ratio Fe^{2+}/Fe^{3+} at these sites [80-84]. The jumping electrons oriented in the field direction and consequently are given a risen in the value of ε'.

Frequency dependence of imaginary part of dielectric constant:

The variation of an imaginary portion of dielectric constant (ε'') for $Co_{0.3}Cu_{0.2}Cd_{0.5}Fe_2O_4$ nanoferrites are shown in Fig. 4.7 including unirradiated and irradiated samples of gamma and neutron. A continuous decrease has been found in the case of ε'' up to a certain increase in frequency and then shows frequency independent nature. Due to the irradiation process of

gamma and neutron, ε'' increases for all studied samples. Similar results had been reported by other investigator with other ferrites [85-89].

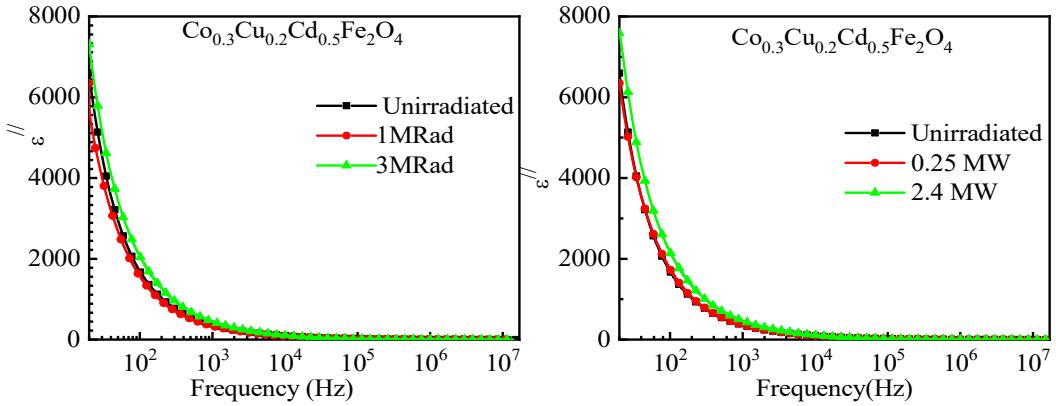

Fig. 4.7 Variation of the imaginary part of dielectric constant as a function of frequency for $Co_{0.3}Cu_{0.2}Cd_{0.5}Fe_2O_4$ nanoparticles before and after irradiation of (a) gamma and (b) neutron by different doses.

The ferrites core loss usually consists of eddy current loss and the additional loss of dipole with hysteresis loss. These are the reason for the decrease of ε''. For ferrite materials, resistivity and eddy current loss have an inverse relationship. Hence, the effect of decreasing resistivity ultimately increases the loss of eddy current. On the other hand, the incapacity to track the applied field's frequency resulted in a decrease in dipole loss at high frequencies. Furthermore, the direct proportional relation between hysteresis loss and frequency was reported [90]. Thus, the way the core loss is increased by the effect of hysteresis loss and eddy current loss effects while decreased by the loss of dipole. These losses from variation sources compete with each other and loss constancy for the ε'' is observed at higher frequencies. In fact, peak is also found in the case of some ferrites for the ε'' variation [91]. The observed peak condition in the ε'' vs frequency (f) spectrum is expressed by the following relation [92],

$\omega\tau = 1$ …… (4.5)

where, $\omega = 2\pi f_{max}$ as angular frequency and τ as the time of relaxation which is related to P as jumping probability per unit time (given by $\tau = \frac{1}{2}$Pi.e.$f_{max} \propto$ P) [93]. A low probability of hopping is implied by the disappearing f_{max} for the studied samples due to the higher resistivity. A maximum loss for the composition of low resistive particles for Li-Mg-Ti ferrites was reported earlier [94]. Moreover, larger relaxation times are seen by the lower hopping probability at room temperature and thus the peak position at a smaller frequency is less than the measurement range (45 Hz–5MHz). The increase by the irradiation process is well explained by the following relation [95],

$$\rho_{AC} = \frac{1}{\frac{\varepsilon}{\varepsilon_0}\omega} \quad \ldots\ldots\ldots\ldots\ldots\ldots \quad (4.6)$$

4.1.6 LOSS TANGENT

The variation of dielectric loss factor $tan\delta$ for $Co_{0.3}Cu_{0.2}Cd_{0.5}Fe_2O_4$ nanoferrites are shown in Fig. 4.8 including unirradiated and irradiated samples of gamma and neutron. There are a several processes that cause the variations in $tan\delta$, including electron hopping and charge defect dipoles and $tan\delta$ behavior at low frequencies is influenced by the first one, and its reaction at high frequencies is influenced by the second. Due to the cationic change in sites, namely Fe^{3+}/Fe^{2+}, the formation of dipoles occurs in ferrites at the time of annealing. On the basis of the phenomenological theory of Koop's, the decrease of $tan\delta$ at initial frequencies can be explained [96]. Due to the hopping charges phase delay for the requisition of excessive exchange energy, higher loss factors are observed at low frequencies. However, low resistance grains at high frequencies and minimum required exchange energy are shown to result in negligible energy loss. As the dose of irradiation goes higher, the peak height goes lower. Depending on the Rezlescu model [97], the existence of peak in $tan\delta$ spectrum can be

explained clearly. According to this model, if the charge hopping frequency of two valance states fits well with the applied field frequency, then this type of behavior has appeared.

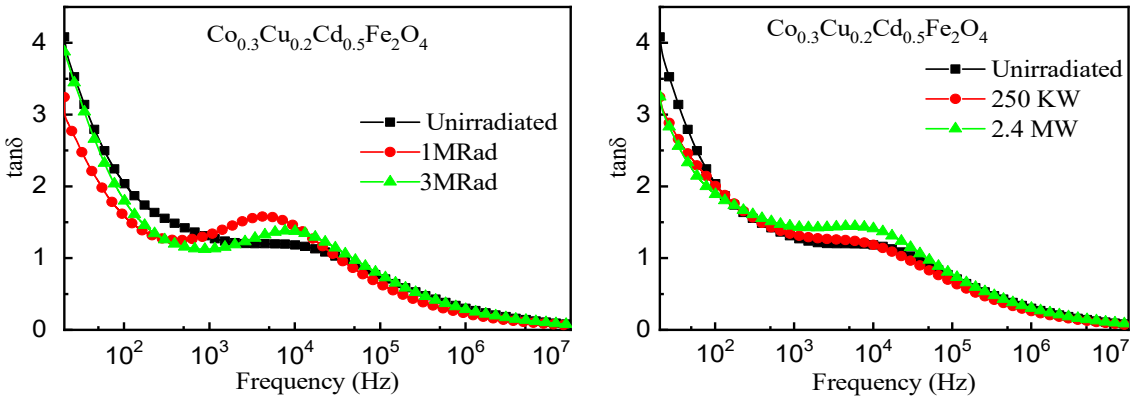

Fig. 4.8. Variation of dielectric loss factor as a function of frequency for $Co_{0.3}Cu_{0.2}Cd_{0.5}Fe_2O_4$ nanoparticles before and after irradiation of (a) gamma and (b) neutron by different dose.

The position of the peak shift towards the region of low frequency as the dose of irradiation of both types increases. This is the indication of decreasing jumping probability with increasing doping content. This decrement attributes the decrease of Fe^{3+} at B-sites and thus causes polarization. The peak height decrement can be explained by the resistivity increase which decreases the Fe^{3+} at B-sites. When the carrier frequency coincides with the applied field frequency then a broad peak as obtained in the present research appears. Because at this situation, the maximum amount of electrical energy has been transferred to oscillating ions which causes maximum loss in power and the peak is then the dominant product. The observed peak relates the relaxation phenomenon of dielectric with satisfying condition $\omega\tau = 1$ and grain to-grain boundary contribution of domain wall resonances also relates to the peak appearance [98]. Other experiments discovered similar results with the dielectric constant [66-69]. The low values of dielectric within both temperatures of annealing declare the ideality of investigated samples for the application in high frequency.

4.1.7 ELECTRIC MODULUS STUDY

In order to determine, analyze, and explain the dynamical features of electrical processes in materials, the formalism of complex modulus is a helpful and essential tool. This includes the rate of the carrier or hopping ion, the relaxation time of conductivity etc. which turns capacitance small at high frequencies and large at low frequencies in a dielectric system. The modulus formalism has renewed its interest in the analysis of materials that are ionically and electronically conducting. In addition to the insight electrical process, the undesired effects are suppressed by this characterization in extrinsic relaxation. Also, the formalism of modulus M can suppress the polarization effect of electrode [99]. The interaction between complicated initial permeability and electric modulus is as follows [100],

$$M^* = (\varepsilon^*)^{-1} = \frac{\varepsilon'}{\varepsilon'^2+\varepsilon''^2} + i\frac{\varepsilon''}{\varepsilon'^2+\varepsilon''^2} = M' + iM'' \quad \ldots\ldots\ldots\ldots (4.6)$$

$$M_\infty = \left[1 - \int_0^\infty e^{-i\omega t}\left\{\frac{d\varphi}{dt}\right\}\right] \quad \ldots\ldots\ldots\ldots\ldots (4.7)$$

Where, M′ is indicating the real parts of electric modulus and M′′ is representing the imaginary parts of the same parameter, $M_\infty = 1/\varepsilon_\infty$ is reciprocal to the dielectric permittivity at high frequency. The function of time evolution φ(t) in the dielectric materials along with the decay functional relaxation time is given by [100],

$$\varphi(t) = EXP\left[-\left(\frac{\tau}{\tau_{M''}}\right)\beta\right] \; 0 < \beta < 1 \quad \ldots\ldots\ldots\ldots (4.8)$$

Where, $\tau_{M''}$ and β are the stretched exponent parameter, which indicates whether the material's relaxation is Debye-type or non-Debye in nature, and the most likely relaxation time.

The real part M' typically include a peak with broad asymmetry with the frequency function in the imaginary part and a sigmoidal behavior is typical in the real part [101-103]. The electrical field relaxation is corresponded by the electrical modulus for steady electric displacement.

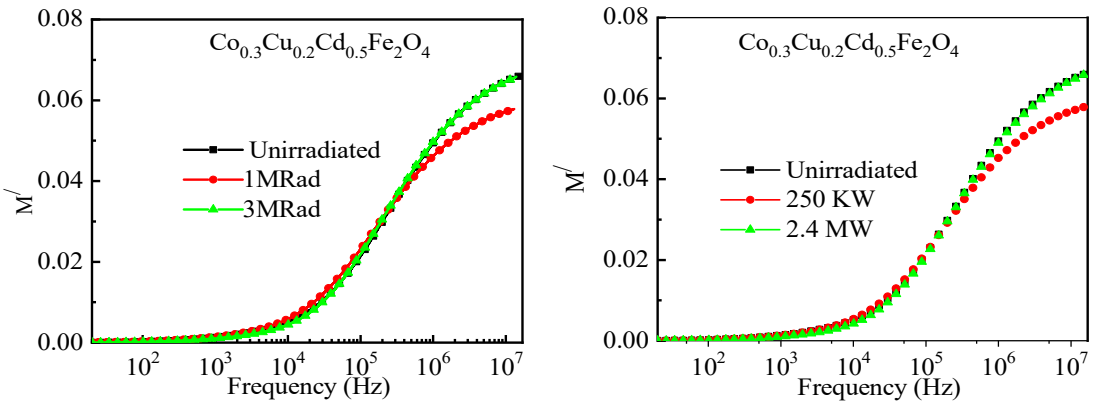

Fig.4.9. Variation in real part of electric modulus as a function of frequency for $Co_{0.3}Cu_{0.2}Cd_{0.5}Fe_2O_4$ nanoparticles before and after irradiation of (a) gamma and (b) neutron by different dose.

The variation of M' and M'' for $Co_{0.3}Cu_{0.2}Cd_{0.5}Fe_2O_4$ nanoferrites are shown in Fig. 4.9 and Fig. 4.10 respectively including unirradiated and irradiated samples of gamma and neutron. According to Fig. 4.9, for the unirradiated and irradiated samples with varying doses, there is initially a minor rise in the area of low frequency and then a large increase up to a specific value in the region of high frequency. The saturation at high frequency might occur for the restoring force unavailability [104]. Because of the long-range travel of the charge carriers during the conduction process and the insignificant contributions of electrode polarization in materials, M' initially seems low [105]. On the other hand, a gradual increase is seen for M'' from Fig. 4.10 which is continued till the M''_{max} value is reached and a decrease is seen afterwards. Relaxation frequency assigns the characteristic frequency as indicated by f_M'' at which M''_{max} occurs. This phenomenon is frequently used to evaluate the time of relaxation τ_M''. The maximum loss of conduction is exhibited by M' [106] in the region of dispersion with

M''_{max} at the central position. Thus, the relation between M'' and dissipated energy takes place in the process of irreversible conduction.

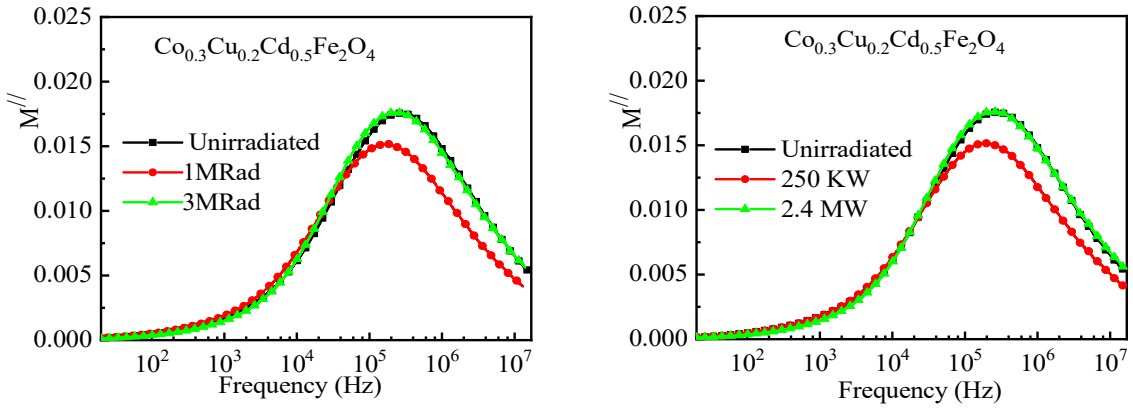

Fig. 4.10. Variation in imaginary part of electric modulus as a function of frequency for $Co_{0.3}Cu_{0.2}Cd_{0.5}Fe_2O_4$ nanoparticles before and after irradiation of (a) gamma and (b) neutron by different dose.

The variation of M' with M'' for $Co_{0.3}Cu_{0.2}Cd_{0.5}Fe_2O_4$ nanoferrites are shown in Fig. 4.10 including unirradiated and irradiated samples of gamma and neutron. A single semicircle is observed in both cases which the center lies under the real axis slightly.

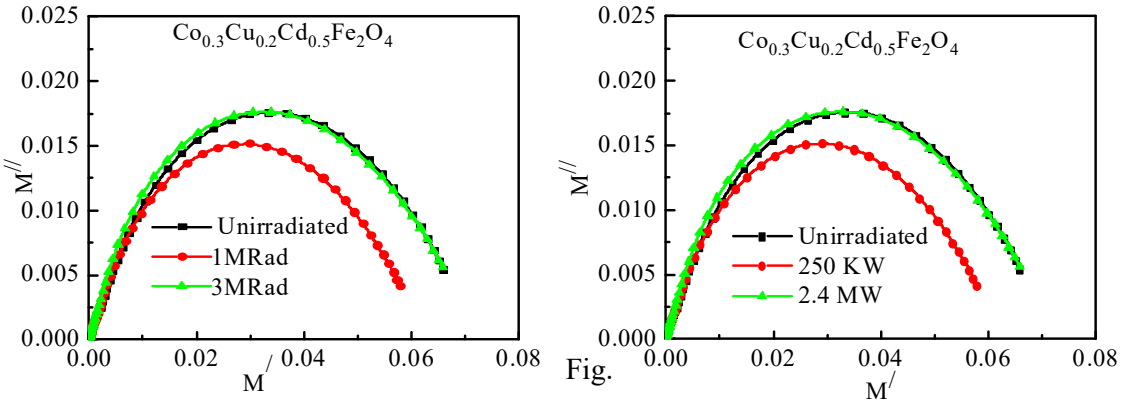

Fig. 4.11. Cole-Cole plots of electric modulus $Co_{0.3}Cu_{0.2}Cd_{0.5}Fe_2O_4$ nanoparticles before and after irradiation of (a) gamma and (b) neutron by different dose.

The appearance of such semicircles indicates the grains conduction process at low frequencies and the grain boundary's conduction process is invisible. The diameters of the semicircles are

different from each other which implies that the values of electrical parameters equivalent to grain are different. Besides, β denotes the circular arc tilt angle with horizontal axis which can extends from 0 to 1 but is usually obtained as lower than 0.25. The corresponding values of β are found less than 1 which is the reflection of non-Debye type relaxation of dielectric with the significant interaction of dipole-dipole in the present investigation. In fact, literatures [107, 108] gives the implication of Cole-Cole plots for electric modulus for the dominating property indication in the material. Electric stiffness can be determined by analyzing cole-cole plots which is the measurement of the difficulty level of dipoles creation or orientation in the solid material. The semicircular arcs from Fig. 4.11 (a) and Fig. 4.11 (b) dominate the electric stiffness of studied materials. The dominant property is assured as electric stiffness by the Cole-Cole semicircular formation before and after the dose of irradiation.

Finally, it is easily concluded that very high gamma rays irradiation and neutron irradiation enhance the magnetization and resistivity of $Co_{0.3}Cu_{0.2}Cd_{0.5}Fe_2O_4$.

4.1.8 IMPEDANCE ANALYSIS

A powerful and most effective technique for correlating the dielectric properties with the microstructure and materials unravel complexity is impedance spectroscopy. The separation phenomenon of grain impedance from other impedance source such as electrode effects and grain boundaries make analysis of impedance the most useful technique of investigation [109]. This analysis is dependent on the discrete components contained idealized model of the electrical circuit. The accomplishment of this analysis is done by the fitted circuit with data for representing the investigating materials [110].

The disparity between the real and imaginary parts of impedance's for $Co_{0.3}Cu_{0.2}Cd_{0.5}Fe_2O_4$ nanoferrites are shown in Fig. 4.12 and Fig. 4.13 respectively including unirradiated and irradiated samples of gamma and neutron.

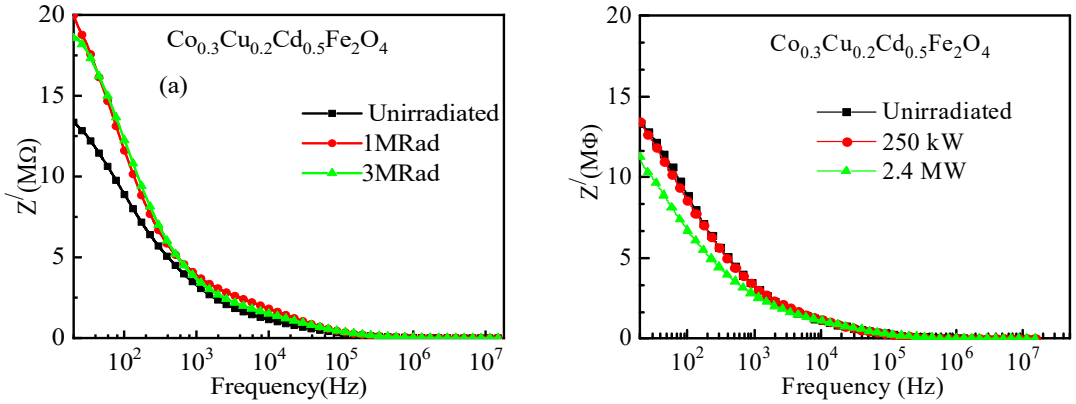

Fig. 4.12. Variation in frequency dependent real part of impedance of $Co_{0.3}Cu_{0.2}Cd_{0.5}Fe_2O_4$ nanoparticles before and after irradiation of (a) gamma and (b) neutron by different dose.

From the variation of Z' of Fig. 4.12, decreasing nature is clearly obtained as frequency increases which causes the ac conductivity to increase at higher frequencies. Impedance is measured at room temperature within the frequency range of 1 kHz to 10 MHz. The variation of Z'' of Fig. 4.13 shows the decreasing nature continuously as the frequency increases due to the decrease in polarization for not following the alternation frequency of the applied field. The Z' values of irradiated samples at 1 MRad dose and 250 kW power are found to decrease whereas increases afterwards at the dose of 2 MRad and 2.4 MW. The same patterns are evident in the case of Z''. The observed patterns are desired from the behavior of the dielectric constant as discussed above and the analysis of ac conductivity which will discussed later. In all cases, two incomplete overlapped semicircles are clearly observed for the samples under investigation. Philippe Knauth et al. [111] reported such large overlapped semicircles for the nano size attribution with the similar tendency of grain and grain boundary.

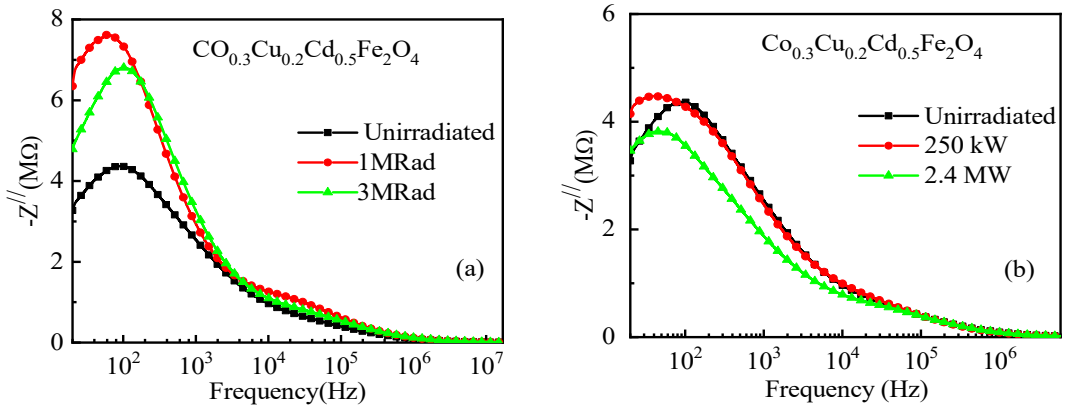

Fig.4.13. Variation in frequency-dependent imaginary part of impedance of $Co_{0.3}Cu_{0.2}Cd_{0.5}Fe_2O_4$ nanoparticles before and after irradiation of (a) gamma and (b) neutron by different dose.

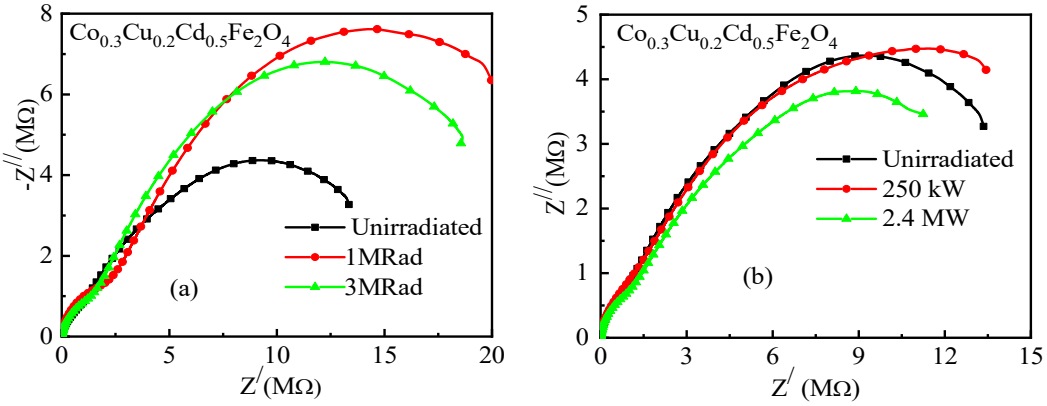

Fig.4.14. Cole-Cole plots of impedance for $Co_{0.3}Cu_{0.2}Cd_{0.5}Fe_2O_4$ nanoparticles before and after irradiation of (a) gamma and (b) neutron by different dose.

Making a plot the imaginary portion of impedance Z'' in opposition to the real component of impedance Z'yields the cole-cole plot for impedance, which is displayed in Fig. 4.14. This plot is particularly convenient to identify the process of relaxation with identical magnitudes to obey the functional forms of cole-cole. Two semi-circles can be evident in the plots with the dependence on electrical properties. The first semicircle is evident because of the resistance of grain boundaries while the second one is due to the grain resistance or bulk resistance [112].

In some cases, a third very small semicircle can be evident due to the electrode or interface contribution at sufficient lower frequency [113].

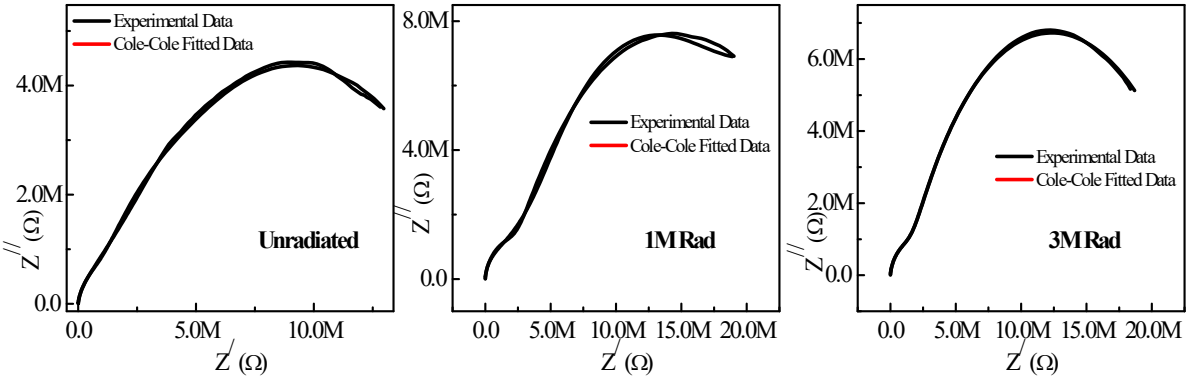

Fig.4.15(a) Cole-Cole fitted plots of impedance for $Co_{0.3}Cu_{0.2}Cd_{0.5}Fe_2O_4$ nanoparticles before and after gamma irradiation.

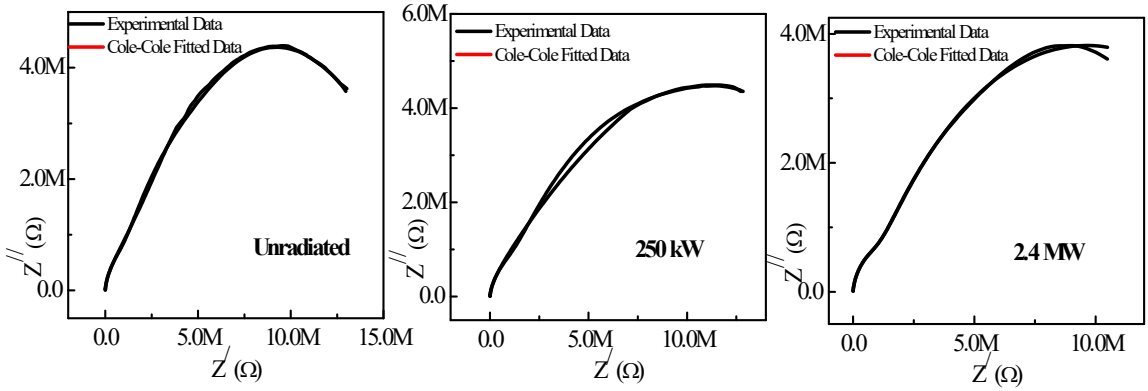

Fig. 4.15(b) Cole-Cole fitted plots of impedance for $Co_{0.3}Cu_{0.2}Cd_{0.5}Fe_2O_4$ nanoparticles before and after neutron irradiation

Theoretical fitted Cole-Cole plots are shown in Fig. 4.15(a) for gamma-irradiated samples and Fig. 4.15(b) for neutron-irradiated samples.

The fitted parameters such as grain resistance (R_g), grain boundary resistance (R_{gb}), grain capacitance (C_g), grain boundary capacitance (C_{gb}) and time constants for grain (τ_g) and grain boundary (τ_{gb}) are listed in Table 4.3. It is evident from Table 4.3 that, the value of R_g increases first for the 1M gamma irradiation and then decreases for 3M gamma irradiation, whereas

reverse nature is found for neutron irradiated samples. Similar tendency is also found in the case of R_{gb}.

Table 4.3: Cole-Cole fitted parameters for the $Co_{0.3}Cu_{0.2}Cd_{0.5}Fe_2O_4$ irradiated and unirradiated samples for neutron irradiation.

Irradiation type	Dose	R, MΩ	C_g, μF	R_g, MΩ	τ_g, μs	α_g	C_{gb}, μF	R_{gb}, MΩ	τ_{gb}, μs	α_{gb}
Before irradiation		9.41	0.63	0.71	2.09	0.47	1.01	0.87	0.45	0.43
Gamma Irradiation	1M	13.83	0.61	1.09	2.01	0.50	1.04	1.39	0.47	0.45
	3M	13.66	0.57	0.99	2.09	0.47	1.08	1.18	0.44	0.41
Neutron Irradiation	250kW	9.27	0.63	0.69	2.09	0.48	1.03	0.88	0.46	0.44
	2.4MW	1.00	0.005	1.09	0.06	0.18	0.003	47.75	0.11	0.002

The interesting thing that is found from these parameters that τ_g and τ_{gb} remains almost same for every observation excepts for the 2.4 MW neutron-irradiated samples. These fitting systems are also reported in previous works [114].

4.1.9 AC CONDUCTIVITY STUDY

The difference in ac conductivity for $Co_{0.3}Cu_{0.2}Cd_{0.5}Fe_2O_4$ nanoferrites are shown in Fig. 4.15 including unirradiated and irradiated samples of gamma and neutron. The ac conductivity values are (σ_{ac}) show slow increase in comparison with the increase in frequency till 10^3 kHz and show rapid rise afterwards for both type of irradiation dose. The rate of increase in the case of gamma irradiation is comparatively lower than that of neutron irradiation at a low dose. Hopping electrons are mainly responsible for the electrical conductivity because the same

elemental ions hopping present more than the singular valence state and are arbitrarily distributed over the lattice sites of equivalent crystals.

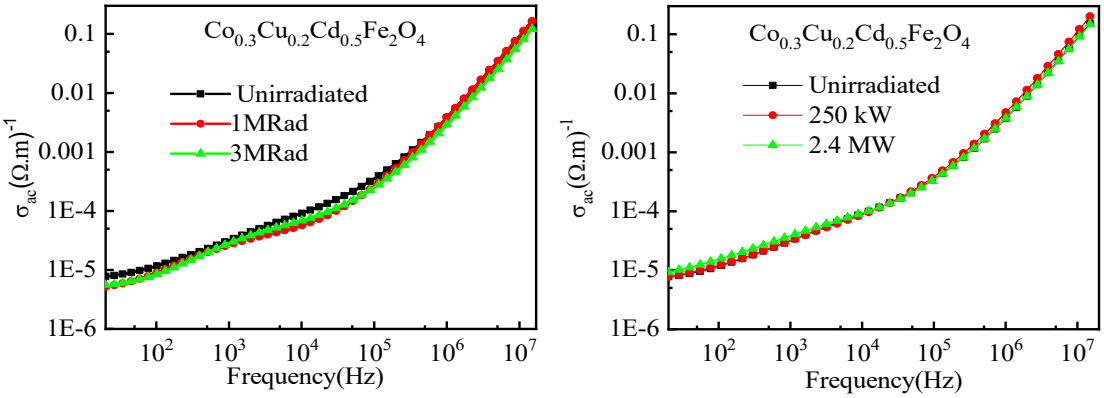

Fig.4.16. Variation in ac conductivity of $Co_{0.3}Cu_{0.2}Cd_{0.5}Fe_2O_4$ ferrite nanoparticles before and after gamma and neutron irradiation by different dose.

In the closed-packed cubic lattice of oxygen, the ionic distances between two metal ions at the A-sites, denoted as A-A (0.357 nm), are greater than those of the B-B sites (0.292 nm). As a result, the likelihood of electron hopping between A⇔B sites is lower than that of B⇔B sites. The reason for less probability of A⇔A is the largest distances between Fe^{3+} and Cd^{2+} at A-sites. Hence, any formed Fe^{2+} during the process of sintering occupies preferentially in the B-sites only [115]. The σ_{ac} variation against the application of frequency is understood by Koop's model [116]. On the basis of this model, the grain boundaries conduct the σ_{ac} at lower frequencies whereas the grains conduct the σ_{ac} at high frequencies [117]. The linear increase of σ_{ac} with the frequency due to the conduction of small polarons was reported by Alder and Feinleib [118]. Due to the contribution of grains at higher frequencies, the mechanism of conduction occurred. The Austin-Motto [119] hopping model of polaron may explain the conductivity as a function of frequency. The conductivity as a function of frequency might be explained by the Austin-Motto [119] hopping model of polaron. This model implies that the increase in σ_{ac} is observed for the small hopping range of polaron while the decrease is due to the long hopping range of polaron as the frequency increases. If band conduction occurs then

the σ_{ac} loose the dependency on frequency and becomes frequency independent [120]. The overall electrical conductivity for the ferrite is expressed as follows:

$\sigma(f, T) = \sigma_{dc}(T) + \sigma_{Ac}(f, T)$ …… (4.9)

Where, σ and σ_{dc} are the total conductivity and temperature dependent dc conductivity respectively. σ_{ac} is dependent on the frequency and temperature and thus hopping mechanism is attributed at the B site. The σ_{ac} with the dependence on frequency is given by the following empirical formula,

$\sigma_{ac}(f) = Af^n$ …v…… (4.10)

where A and n are constants that depend on composition and temperature; n is dimensionless whereas A has units of ac.

4.2.1 RESULTS AND DISCUSSION OF $Ni_{0.3}Cu_{0.2}Cd_{0.5}Fe_2O_4$

4.2.2 STRUCTURAL ANALYSIS

The patterns of XRD for $Ni_{0.3}Cu_{0.2}Cd_{0.5}Fe_2O_4$ with and without gamma irradiation and neutron irradiation are shown in Fig. 4.17 (a) and Fig. 4.17 (b). For every sample, these two figures show the spinel's single phase. All of the samples confirm the FCC spinel structure in the patterns of XRD without any secondary phase. The lattice constant (a) of the investigated samples is displayed in Table 4.4. As the irradiation dose increase, an increase in the crystallite sizes has been observed for the Ni-Cu-Cd ferrites due to the irradiated energy role on the unit cells. Without any secondary phase, every sample verifies the FCC spinel structure in the XRD patterns. Table 4.4 shows the lattice constant (a) for the samples under investigation. Because of the irradiated energy effect on the unit cells, a rise in the crystallite sizes for the Ni-Cu-Cd ferrites has been seen when the irradiation dosage increases. Also, a slight increase is noticed in the lattice constants between two irradiated ferrites samples for the interacted gamma rays dominant effect with external electrons from iron where the conversion of larger size Fe^{2+}(0.76 Å) from the smaller Fe^{3+}(0.67 Å).

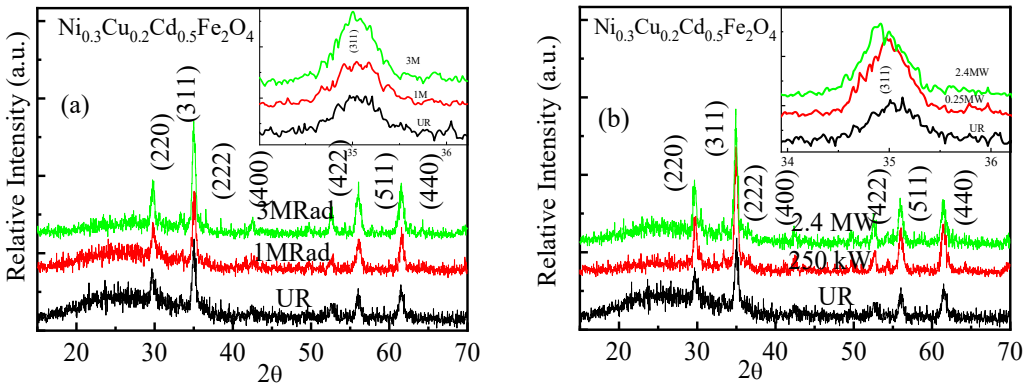

Fig. 4.17 The XRD patterns of the unirradiated and (a) gamma irradiated $Ni_{0.3}Cu_{0.2}Cd_{0.5}Fe_2O_4$ and (b) the neutron irradiated $Ni_{0.3}Cu_{0.2}Cd_{0.5}Fe_2O_4$ samples.

Furthermore, the shifting to the smaller values of 2θ is evident from the irradiated peaks and intensities them become lower as shown in Fig. 4.17. The peaks width becomes broader due to the irradiation dose on the samples. Table 4.4 depicts the increase in lattice constant due to the irradiation dose which occurs for the generation of vacancies that causes distortion along with deviation from the structure of cubic spinel [123]. The reason might be lie in the compressive strain produced by the irradiation as indicated by the peak positional shift to a shorter value of 2θ and structural disorder in lattice generation as indicated by the peak broadening with enhanced intensities. The structural effects are observed due to the expectation of ions of the compound to get affected by the neutron irradiation and outermost shell electrons are not affected by the process of irradiation. Accordingly, the vacancy pairs of cluster formation get a favor.

Table-4.4: Grain and grain boundary parameters

Radiation	Dose	A (Å)	M_s(emu/gm)	R_g (kΩ)	C_g (pF)	R_{gb}(kΩ)	C_{gb}(pF)
Unirradiated		8.54526	35.28523	1221.11	81.8927	5650	1.7699
Gamma	1M Rad	8.55182	32.61652	1523	65.6598	14990	0.6671
	3M Rad	8.55249	37.04163	2342	42.6985	8842	1.1309
Neutron	250kW	8.55221	29.61294	1389.1	71.9890	10432	0.9585
	2.4 MW	8.55362	51.02496	1458	68.5871	9318	1.0731

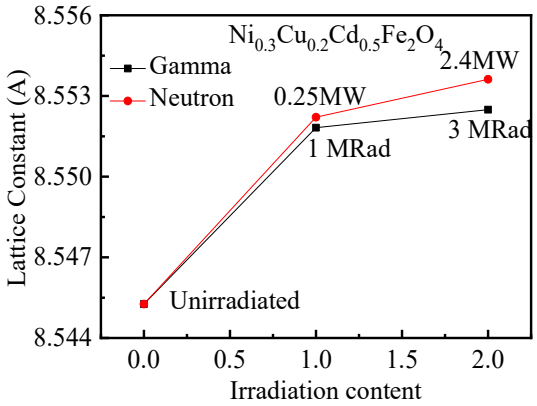

Fig. 4.18 Typical N-R functions of the unirradiated and irradiated samples of gamma and neutron irradiation of the $Ni_{0.3}Cu_{0.2}Cd_{0.5}Fe_2O_4$.

Small intensities of Fe_2O_4 emerged as a new phase in the samples subjected to neutron irradiation. Moreover, vacancy cluster pairs are also created by the disappearing planes 222 and 533. From a deeper perspective, it is evident from the XRD of both cases that irradiation through neutron shifts planes more than that of gamma irradiation. Thus it confirms the ionization and displacement type damage production by the radiation in spinels [124]. Due to the disorder in cations, both octahedral vacancies and tetrahedral vacancies of cations are

possible however octahedral vacancies of cations are proposed only for the inverse spinels [125, 126]. The generation of cation vacancies is caused by the irradiation through fast neutron necessary for neutral charge maintenance. There is a possibility of spinel inversion increment and lattice parameter decrement by neutron irradiation [125]. Since the lattice parameter decreases as the inversion parameter increases due to neutron irradiation on the samples, the results of the current investigation are in excellent accord with the potential reflection of irradiation.

4.2.3 RIETVELD REFINEMENT AND CATION DISTRIBUTION

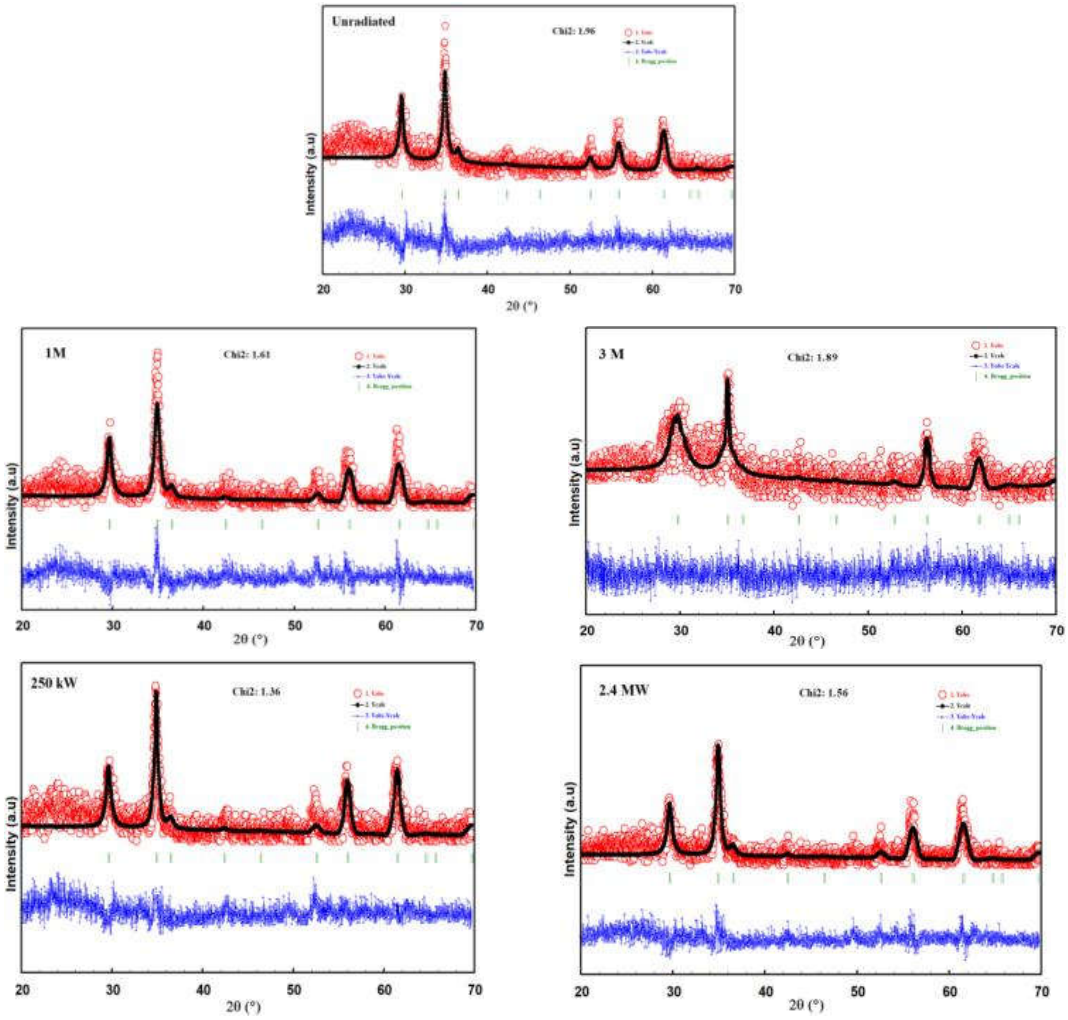

Fig. 4.19. The Rietveld refinement output patterns of the unirradiated and irradiated samples of gamma irradiation and the neutron irradiation of the $Co_{0.3}Cu_{0.2}Cd_{0.5}Fe_2O_4$.

The XRD data are subjected to additional analysis using the Rietveld refinement method. The resulting patterns, which comprise the patterns of samples both pre- and post-irradiation with gamma and neutron radiation, are displayed in Figure 4.19. Rietveld refinement is the process of fitting experimentally obtained data with the calculated data. In this investigation, the refinement of the Rietveld method is performed with the help of Full Prof. suit software. The symmetry is chosen as Fd-3m which is the basic space group for cubic ferrites. The whole system is analyzed under the peak function of pseudo-voigt. The atomic position of oxygen is taken as an open parameter whereas the remaining is taken as fixed parameters. The least-square formalism has been introduced for the pattern-fitting process. The refinement process continues till the value of χ^2 becomes as lower as possible. It is well known that the value of χ^2 less than 4 is considered good fitting while the value of the same parameter less than 2 is considered as best fitting. Hence, the refinement in the present investigation is performed till the value of χ^2 comes down below 2. The final χ^2 values of unirradiated, γ irradiated and neutron-irradiated samples are 1.96, 1.61, 1.89, 1.36 and 1.56, respectively. These obtained values of χ^2 are directly labeled on the output pattern as seen in Fig. 4.18. As a result, all sample refinement methods display the best-fitted curve between computed and observed data. Below the fitted curves, the Bragg position and the discrepancy between the predicted and observed values are shown individually.

4.2.4 MAGNETIC HYSTERESIS

Fig. 4.20 displays the change in magnetization (M) in $A.m^{-1}$ as a function of applied magnetic field (H) in T up to the limit of 1T. This data comprises samples that were both irradiated and unirradiated by γ and neutron at room temperature. As is typical for ferrite, a rise in magnetization is indicated by a growing magnetic field. In essence, electron mobility of spin

and orbital, electron magnetic moment, and atomic and ionic magnetic moment are the sources of magnetic characteristics and magnetism. The reason for the atomic magnetic moment is the electrons' motion in their own orbits and the motion of their spin.

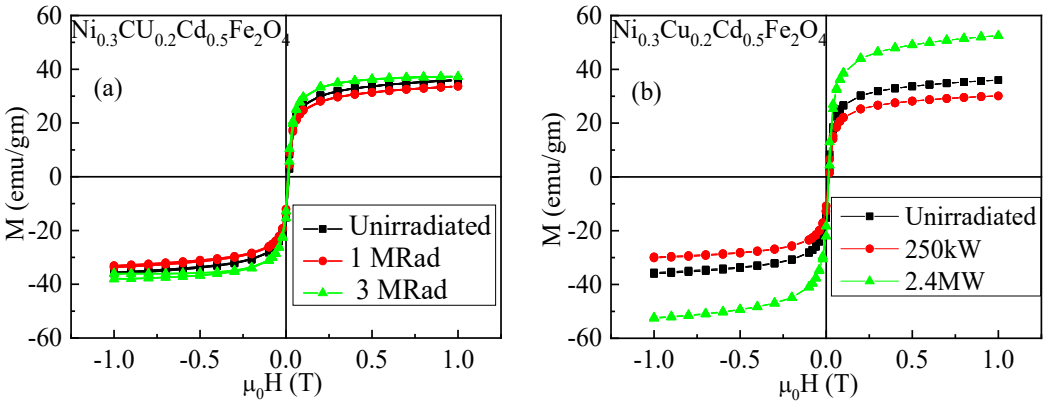

Fig. 4.20 Variation of M with H for different compositions of $Ni_{0.3}Cu_{0.2}Cd_{0.5}Fe_2O_4$ before and after (a) gamma and (b) neutron irradiation by different dose.

The increasing nature of M is observed until the value of μ_0H as 0.25 T and a slow rise is observed beyond that and finally attains saturation. The determination of saturation magnetization M_s is done by extrapolating magnetization plots for $1/(\mu_0H) = 0$. Depending on the distribution of cation and exchange interaction, this typical behavior of M_s with the content of Cu^{2+} can be explained. It is well known that the site preference of cations influences the properties of magnetic ferrites. One possible explanation for the magnetic properties of synthetic samples is the ionic competition of ferromagnets such as Fe^{3+} (5 μ_B), Ni^{2+} (2 μ_B), Cu^{2+} (1 μ_B) and Cd^{2+} (0 μ_B) preference towards A and B sites. Belavi et al [62] and Hemeda [63] also reported similar results. Moreover, improved magnetic properties are expected for ferrites samples due to being a Jahn-Teller ion, Cu leads to the enhanced distortion of the lattice which probably produces larger strain in the lattice and thus attributes magnetic improvement [128]. The coercivity of the M vs H curve is found very low for synthesized samples and thus

confirming the nature of soft ferrites for investigated samples. The M_s has been found lower than the corresponding values of bulk ferrites. Due to the existence of morphological core-shell, containing surface layer like spin-glass and aligned spins core of ferrimagnet, the values of M_s become low. As a result, broken bonds of super exchange cause the disorder and canting of spins of the surface layers and atomic symmetry of unlike local type closer to the surface layer gives the smaller value of M_s for the nanocrystals.

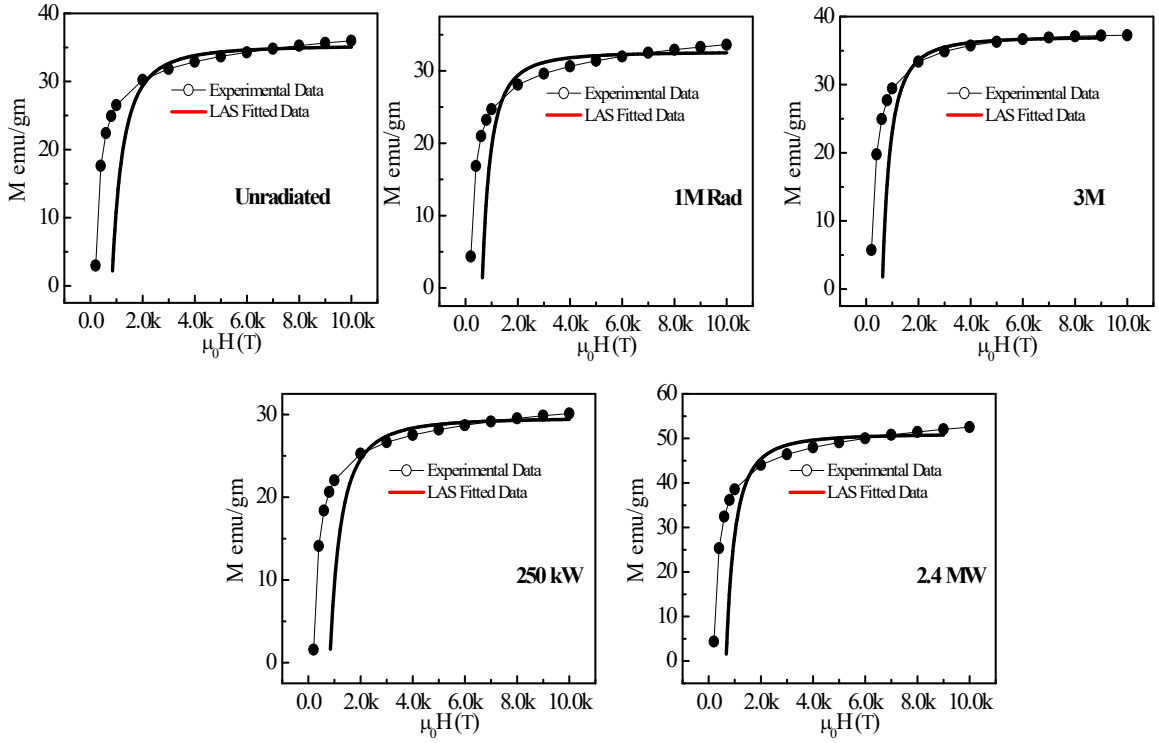

Fig. 4.21. Variation of M with H for different compositions of $Co_{0.3}Cu_{0.2}Cd_{0.5}Fe_2O_4$ before and after (a) gamma, (b) neutron irradiation by different dose and (c) LAS fitted curves for every samples.

As the super exchange interactions are present in the ferrites, the above effects are dominant especially. Thus, the interaction of A-B exchange is reduced and causes a subsequent decrease in the values of M_s for all investigated samples of Ni-Cu-Cd nanoferrites. The well-known rule of approach to saturation process was used to the experimental data to generate well-fitting

lines for high-field analysis. Fig. 4.21 displays the LAS fitted curves, and Table 4.4 lists the fitted parameters.

4.2.5 DIELECTRIC STUDY

The degree of polarization in a ferrite material could be observed with a dielectric constant. In a frequency-dependent case, the dielectric constant can be expressed as,

$\varepsilon = \varepsilon^{'} - j\varepsilon^{''}$ ..... (4.11)

Where the real part (ε') and complex part (ε'') present the stored energy and energy dissipation respectively. The dielectric loss tangent ($tan\delta$) is obtained with the ratio, $\frac{\varepsilon''}{\varepsilon'}$. Fig. 4.22 and Fig. 4.22 represent the frequency-dependent ε' and ε'' respectively with gamma and neutron irradiation effects.

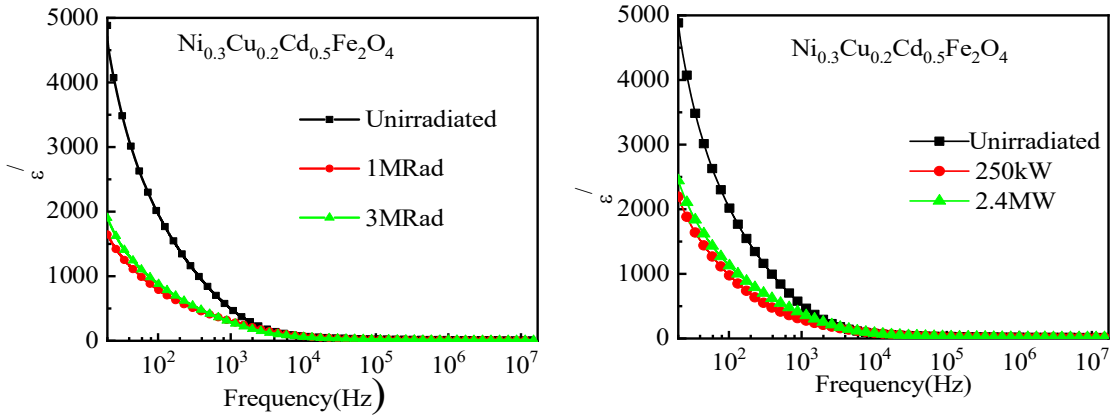

Fig. 4.22 Variation of real part of dielectric constant as a function of frequency for $Ni_{0.3}Cu_{0.2}Cd_{0.5}Fe_2O_4$ nanoparticles before and after irradiation of (a) gamma and (b) neutron by different doses.

The values of ε' and ε'' reveal maximum magnitudes at a lower frequency while the values fall gradually with increasing frequency and become minimum at the higher frequency. A sharp decreasing nature of the dielectric characteristics can be observed initially while it becomes almost frequency invariant after 10 kHz at both the irradiation cases. The Maxwell–Wagner

[129] concept of interfacial polarization explains the observed dielectric dispersion in the present study which is also well consistent with Koop's phenomenological view [130]. In such prospects, ferrite materials with a polycrystalline structure are usually treated with the concept of grains, a regular piled up of parallel semiconducting phases, which are separated by thin resistive interfaces called grain boundaries. Upon applying an external field, interfacial polarization can be observed by the localized accumulation of charges. The contribution of interfacial polarization varies with the field frequency and the highest role can be observed at lower frequency [121]. Thus, the highest dielectric magnitudes can be observed initially in the study.

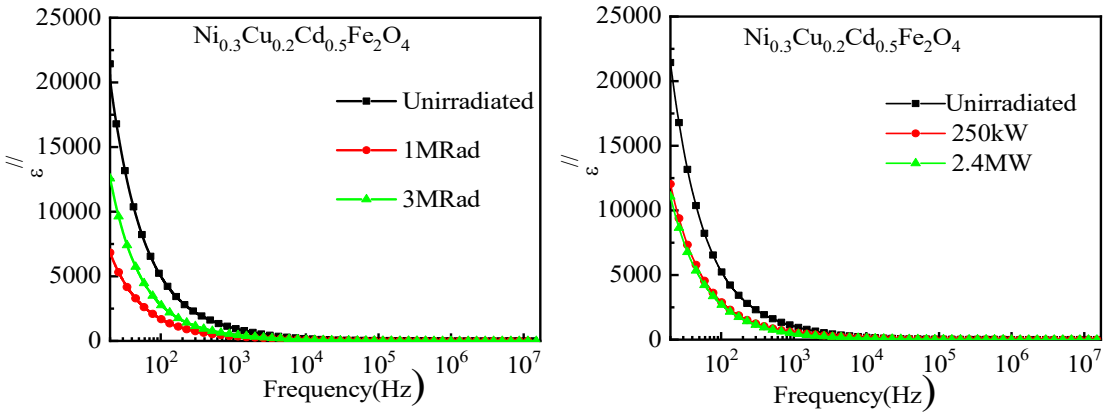

Fig. 4.23 Variation of the imaginary part of dielectric constant as a function of frequency for $Ni_{0.3}Cu_{0.2}Cd_{0.5}Fe_2O_4$ nanoparticles before and after irradiation of (a) gamma and (b) neutron by different doses.

The largest dielectric magnitudes at the lower frequency are also attributed to oxygen vacancies, dislocation pile-ups, Fe^{2+}, and grain boundary defects [122]. The space charge carriers are able to keep their axes initially aligned regularly with the applied field. The dielectric values decrease dramatically with rising frequency and become almost frequency invariant at higher frequencies as a result of the charge carriers' inability to follow the field as before owing to a lack of time when the field frequency increases gradually [131,132]. The

dielectric characteristics having decreasing nature with the field frequency can usually be observed in ferrite investigations. Similar dielectric behaviors can also be seen in Ni-Cu [128], Ni-Cd [133], Ni-Cu-Zn [134] and Mg-Cu-Zn [134] ferrites. Effects of gamma and neutron irradiation on ε′ and ε″ can be observed clearly in Fig. 4.22 and Fig 4.23. In both the irradiation cases, the initial dielectric values possess lower magnitudes compared to the unirradiated ones. These lower dielectric values due to gamma and neutron irradiation represent the lower contribution of polarization processes initially [121]. Besides, smaller and uniform grains, homogeneity and better symmetry also attributed to the lower dielectric values in the ferrites [122, 135]. Ferrites with higher dielectric magnitudes as well as lower dielectric magnitudes show useful technological applications. Capacitive components utilize ferrites with higher dielectric magnitudes while electronic insulation applications expect ferrites with lower dielectric magnitudes [136]. Fig. 4.24 shows the frequency-dependent dielectric loss tangent with gamma and neutron irradiation effects. The energy dissipation at different frequencies within a dielectric medium can be observed with the dielectric loss tangent. In ferrites, the loss tangent determines the total core loss. Therefore, low loss values are highly expected for low core loss in technological applications, which is achieved by our investigated ferrite. In Fig. 4.24, the dielectric loss values are observed with higher magnitudes at lower-frequencies while the magnitudes decrease with increasing frequency and become minimum at higher frequency. At lower frequencies, electron exchange between Fe^{2+} and Fe^{3+} ions require more energy and hence, higher magnitudes of dielectric loss can be observed initially. On the other hand, electron exchange happens with a minimum amount of energy at a higher frequency and therefore, the lower magnitudes of dielectric loss [137]. Different parameters like stoichiometry, structural homogeneity, heat treatment environment and ferrous ion content also show noticeable effects on dielectric loss [138]. The dielectric loss studies reveal peaks at both the irradiation cases as shown in Fig. 4.24. Such peaking nature appears in the dielectric loss

study when applied field frequency coincides with the electron hopping frequency and thus resonance occurs [139]. At both the irradiation cases, the resonant peaks move downward showing lower dielectric loss.

4.2.6 LOSS TANGENT

Two processes are thought to be responsible for the fluctuation of $tan\delta$ in ferrites: (1) electron hopping, and (2) charged defect dipoles. The defect dipoles' reaction to the applied ac field in the high-frequency zone is the cause of the first mechanism, which contributes to the dielectric loss tangent in the low-frequency region. Changes in cation sites, such Fe^{3+}/Fe^{2+}, during the annealing process are what cause these dipoles to arise in ferrites.

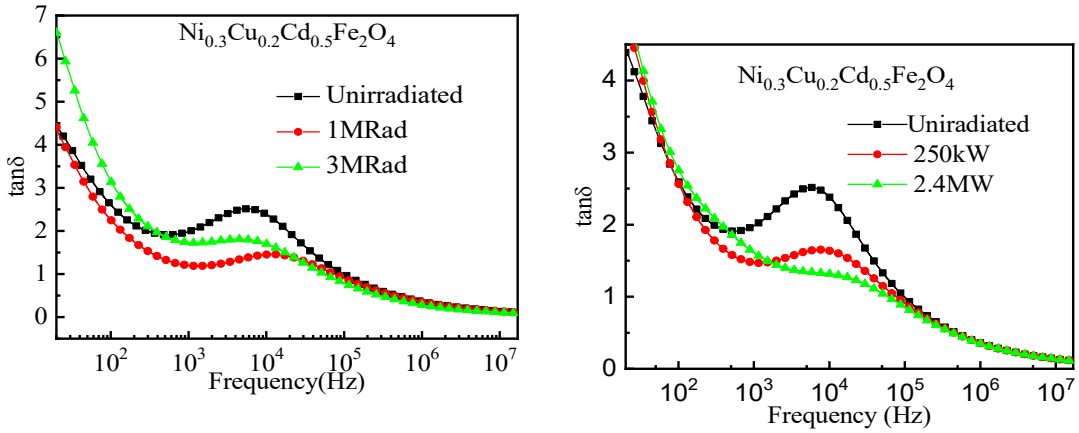

Fig. 4.24 Variation of dielectric loss factor as a function of frequency for $Ni_{0.3}Cu_{0.2}Cd_{0.5}Fe_2O_4$ nanoparticles before and after irradiation of (a) gamma and (b) neutron by different dose.

The initial decrease in $tan\delta$ with increasing frequency is explained by Koop's phenomenological theory of dielectrics [140].

Higher loss factors have been identified in both cases due to the phase delay of hopping charge with frequency in the lower frequency area, which corresponds to high resistivity due to grain boundaries and requires more energy to exchange electrons between Fe^{3+} and Fe^{2+} ions. Thus, the energy loss is high. Conversely, reduced resistivity (caused by grain) and lower energy needed for electron exchange between Fe^{3+} and Fe^{2+} ions are associated with the high

frequency range (5MHz). Thus, the energy loss is low at higher frequencies. Furthermore, it has been shown that when large doses of radiation are applied, the peak's height decreases. The peaking behavior of $tan\delta$ is clearly explained in the light of Rezlescu Model [141]. According to this model, the behaviour appears when the frequency of charge hopping between the two valance states of the same element matches the frequency of the applied field. The peak position of $tan\delta$ shifts towards the lower frequency area with a growing high dose of gamma and neutron irradiation, demonstrating that an increase in doping content reduces the jumping likelihood. The reduction in the quantity of Fe^{3+} ions at B-sites, which cause the polarization in ferrites, might be the cause of this decline in the jumping likelihood. The further explanation for the peak height drops with composition might be because the quantity of Fe^{3+} ions at the octahedral location decreases as resistivity increases. The board peak appears when the hopping frequency of the charge carrier coincides with the frequency of the applied electric field, the maximum electrical energy is transferred to the oscillating ions and a peak is observed as a result of maximum power loss. If the condition $\omega\tau = 1$ is met, this peak is associated with the dielectric relaxation phenomenon. It is also a result of the domain wall resonance, or grain-grain boundary contribution, as reported by Batoo et al. [143], Ramay et al. [144], and Ramesh et al. [145]. Our researched ferrites' low dielectric values at both annealing temperatures make them perfect from the standpoint of high-frequency applications. Thus, at higher frequencies, the current ferrite series with relatively low losses may find value in technological applications, and it also aligns with another finding by Batoo et al. [143]. with a 5 kHz loss factor.

4.2.7 ELECTRIC MODULUS STUDY

In analyzing the electrical transport properties of ferrite nanoparticles, the electric modulus study is a well-established technique. This essential technique also provides quantitative information about the structural nature of a polycrystalline sample along with the electrical

relaxation phenomenon as a microscopic property [146, 147]. The electric modulus can be expressed simply as [148]

$M^* = M' + jM''$ ..... (4.12)

where the real part (M') and the complex part (M'') correlate with dielectric constant as

$M' = \frac{\varepsilon'}{\varepsilon'^2+\varepsilon''^2}$ and $M'' = \frac{\varepsilon''}{\varepsilon'^2+\varepsilon''^2}$ ..... (4.13)

In the M'' study, typical broad peaks with an asymmetric nature can be observed while a sigmoidal step-like characteristic often appears in M'[149]. Fig. 4.25 represents the frequency-dependent M'along with effects of both gamma and neutron irradiation.

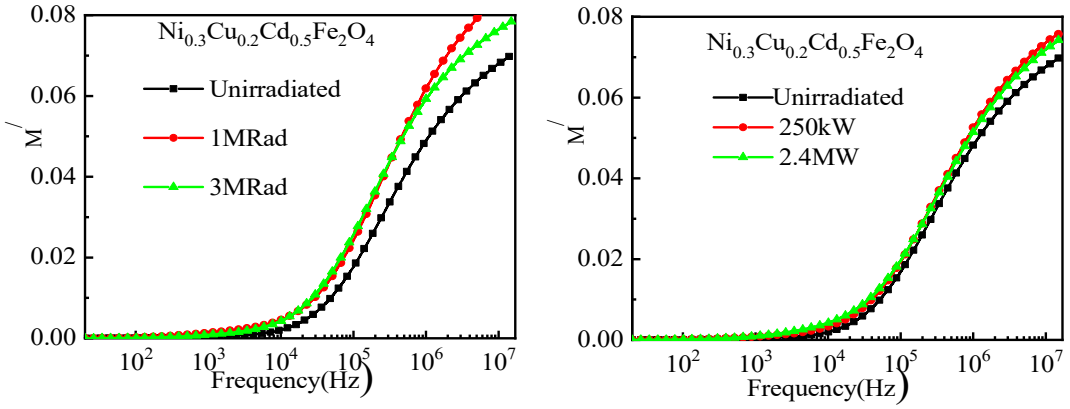

Fig. 4.25 Variation in the real part of electric modulus as a function of frequency for $Ni_{0.3}Cu_{0.2}Cd_{0.5}Fe_2O_4$ nanoparticles before and after irradiation of (a) gamma and (b) neutron by different doses.

At lower frequencies, $M'$is observed with very low magnitudes while the values rise sharply with increasing field frequency in the case of both irradiation cases. Besides, the M' values are observed to be saturated at a higher frequency range. The low-frequency variation of M' represents the conduction behavior due to charge carrier motion with long-range nature. At high frequency extents, the saturation of M' presents the frequency invariant nature and shows the electrode polarization with a negligible role in the investigated samples[148, 150]. The high-frequency saturation of M'observed in the study may also express the lack of

restoring force[148]. Fig. 4.26 shows the frequency-dependent M'' with gamma and neutron irradiation effects.

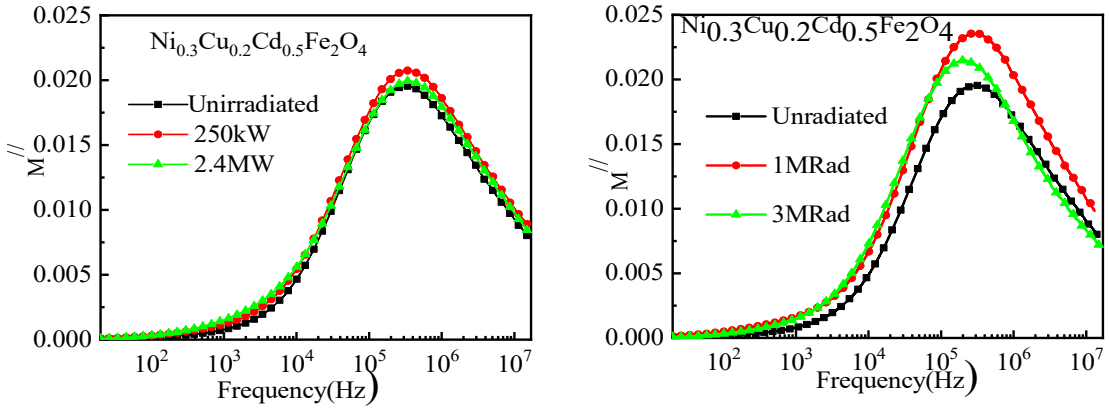

Fig. 4.26 Variation in imaginary part of electric modulus as a function of frequency for $Ni_{0.3}Cu_{0.2}Cd_{0.5}Fe_2O_4$ nanoparticles before and after irradiation of (a) gamma and (b) neutron by different doses.

The M''values are observed with lower magnitudes initially and the values rise gradually in order to form various broad peaks near the mid frequency extents. After the peaks, the M'' values fall sharply with increasing frequency. The conductivity relaxation behavior in the material draws such broad peaks in the $M''$and with the help of relaxation time distribution approach, these broad peaks are often interpreted. The broad peaks having position near the mid frequency, therefore, trace up two distinct frequency extents in the complex modulus plots; the low frequency regions before the peaks and the high frequency region after the peaks. Before the peaks, i.e. at the low frequency side, the charge carriers get longer distances for travelling and therefore, particular probability for successful hopping can be observed for the ions. On the other hand, the localized motion within the potential wells with spatial confinement of the ions can be observed at high frequency region, i.e. after the peaks. As a result, the peaks are appeared at the transition position between long-range and short-range

mobility characteristics of the charge carriers [131,147]. Such nature of complex modulus plots also implies the charge transport mechanism with hopping type electrical conduction in the investigated materials. When the dosage of gamma irradiation increases, the highest peak is seen to move towards a lower frequency. These backward deflections of peaks maximum reveal an increment of relaxation time by the increasing doses [151].

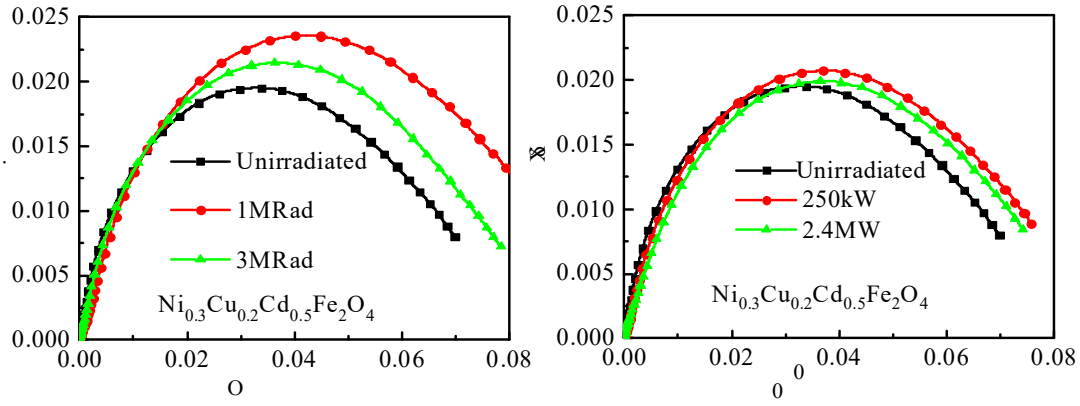

Fig. 4.27 Cole-Cole plots of electric modulus $Ni_{0.3}Cu_{0.2}Cd_{0.5}Fe_2O_4$ nanoparticles before and after irradiation of (a) gamma and (b) neutron by different doses.

The grain and grain boundary contributions can be observed with the electric modulus spectra (M''versus M' plots) depending on the relaxation time constant difference, as shown in Fig. 4.27. Typical semicircular arcs have been observed in the modulus spectra for both the gamma and neutron irradiation cases. The observed semicircles are depressed and trace the centers under the abscissa. Such semicircles in the modulus spectra identify the relaxation behavior with non-Debye characteristic (deviated from actual Debye nature) in the material [152]. In our study, only a single semicircular arc can be observed in the modulus spectra without overlapping the secondary one. The presence of semicircular arcs in the modulus spectra ensures the single relaxation along with single phase nature remains after irradiations.

4.2.8 COMPLEX IMPEDANCE STUDY

Impedance spectroscopy is a highly efficient technique in analyzing the grain and grain boundary resistance in the crystalline structure. This potential technique also visualizes the structure, conduction routes and defects in the structure. In terms of the real (Z') and imaginary (Z'') part of impedance can be expressed as [153]

$Z = Z' + jZ''$ ..... (4.14)

The Z' and Z'' can be expressed with a phase shift (θ) and magnitude $|Z|$ by the following expressions

$Z' = |Z|cos\theta$ and $Z'' = |Z|sin\theta$ ..... (4.15)

The impedance plot, also popular as the 'Nyquist plot', usually traces up two semicircular arcs; one is in the low-frequency region which describes the grain boundary contribution and another is in the high-frequency region which illustrates the grain contribution.

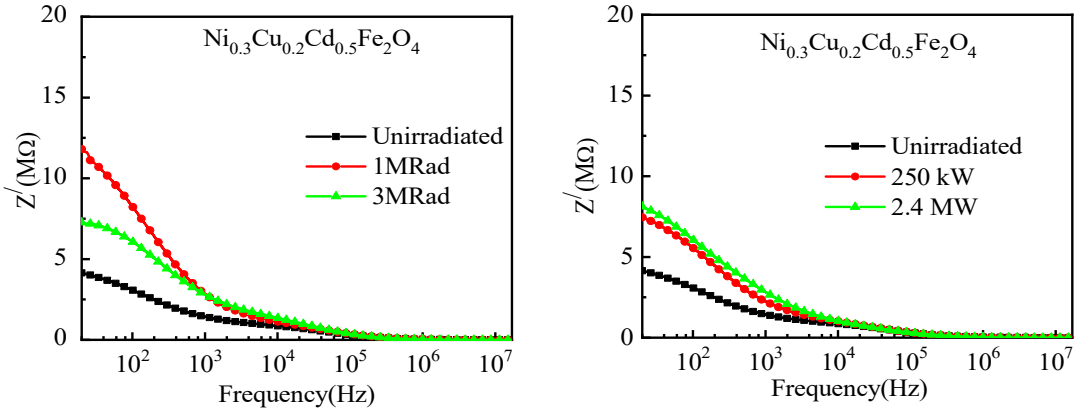

Fig. 4.28 Variation in frequency-dependent real part of the impedance of $Ni_{0.3}Cu_{0.2}Cd_{0.5}Fe_2O_4$ nanoparticles before and after irradiation of (a) gamma and (b) neutron by different doses.

The semicircles may occupy various depressed shapes in the impedance spectra and thus, the impedance plots are also familiar as Cole-Cole, Davison-Cole, Debye plots etc. depending upon the semicircular shapes. Fig. 4.28 shows the frequency-dependent Z' for both irradiation

cases. Initially, Z'possesses higher magnitudes while the resistance falls rapidly with increasing frequency. The rapid declination of Z' magnitude represents an increment of ac conductivity with increasing frequency. In both the irradiation cases, the Z' curves for different doses are observed to merge at high-frequency extents. This high-frequency coincidence of Z' curves presents the intrinsic grain effects [154]. In a similar way, the initial higher magnitudes of resistance exhibit the predominant role of grain boundary contribution which correlates Koop's model of dielectric results with good agreement. Fig. 4.29 represents the frequency-dependent Z'' along with gamma and neutron irradiation effects. In Z''curves are observed with various broad peaks at both the irradiation cases. The observed peaks shifted with irradiation doses. In the investigation, the relaxation characteristic introduces peaking nature in the complex impedance curve [155]. Besides, the backward shifting of such peaks points out the single relaxation mode in the studied material.

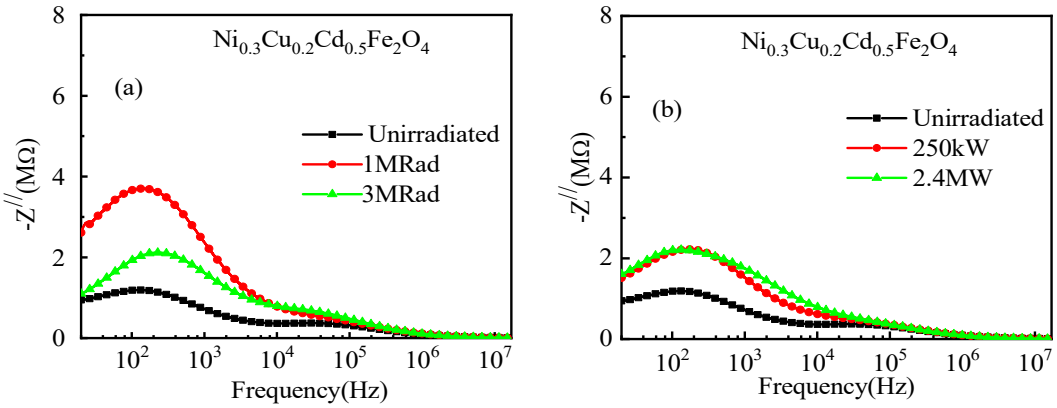

Fig. 4.29 Variation in frequency-dependent imaginary part of impedance of $Ni_{0.3}Cu_{0.2}Cd_{0.5}Fe_2O_4$ nanoparticles before and after irradiation of (a) gamma and (b) neutron by different doses.

Like Z' curves, the Z'' curves are also merged at a higher frequency and express the space charge polarization with continuous attenuation. In our investigation, both the Z' and Z''values

acquire higher magnitudes with irradiation doses as seen in Fig. 4.28 and Fig. 4.29 respectively. These rising magnitudes of impedance reveal the increasing defective structure of our studied sample and are expected for low-frequency regions. Fig. 4.30 represents the Cole-Cole plots of the investigation.

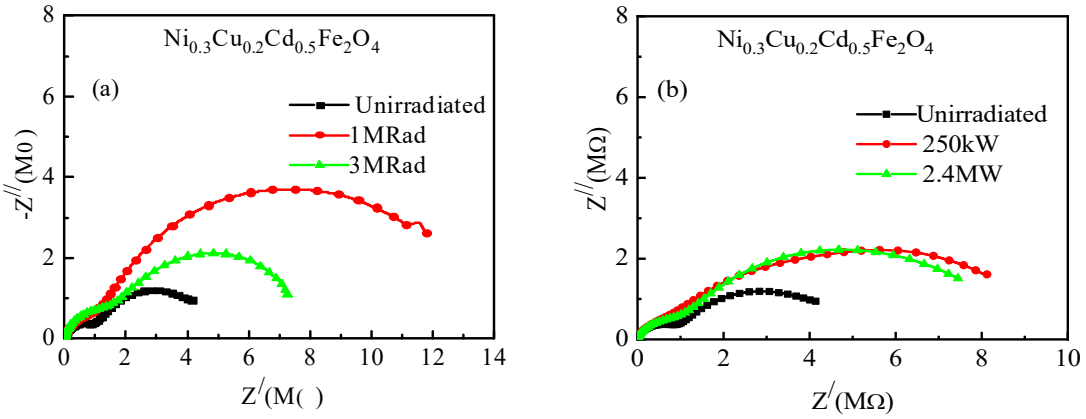

Fig. 4.30 Cole-Cole plots of impedance for $Ni_{0.3}Cu_{0.2}Cd_{0.5}Fe_2O_4$ nanoparticles before and after irradiation of (a) gamma and (b) neutron by different doses.

In the Cole-Cole plots, the tendency for forming two semicircular arcs with overlapping natures can be observed in both the irradiation cases. Impedance plot usually shows a single semicircular pattern for the materials with smaller grain structures while a pair of semicircular patterns with overlapping nature can be observed for the compositions with larger grain structures as well as the relative value of grain resistance (g) and grain boundary resistance (gb) observed. Besides the grain distributions, the magnitude of contributions can also be observed with the semicircular sizes [156, 157]. The impedance plots with overlapping semicircles represent the g contributions with smaller semicircles observed at a higher frequency while the gb contributions can be seen with larger semicircles observed at a lower frequency. The separation of the overlapping semicircles appears with the variation of the relaxation time constant and it can be observed significantly when the time constant varies with a factor below 100 [158]. In the present investigation, the semicircles showing g contributions

at high frequency are observed smaller compared to semicircles representing gb contributions at low frequency in both the irradiation cases. The observed semicircles possess different depressed shapes which shows the irradiation causes resistance behavior in the composition [159]. In the case of gamma irradiation, the grain boundary semicircle corresponding to 1MRad irradiation dose shows a larger size compared to others. This larger size implies a higher grain boundary contribution as shown in Table 4.1. The inset of Fig. 4.30 shows the equivalent circuit for structure-property relatedness using the brick-layer approach.

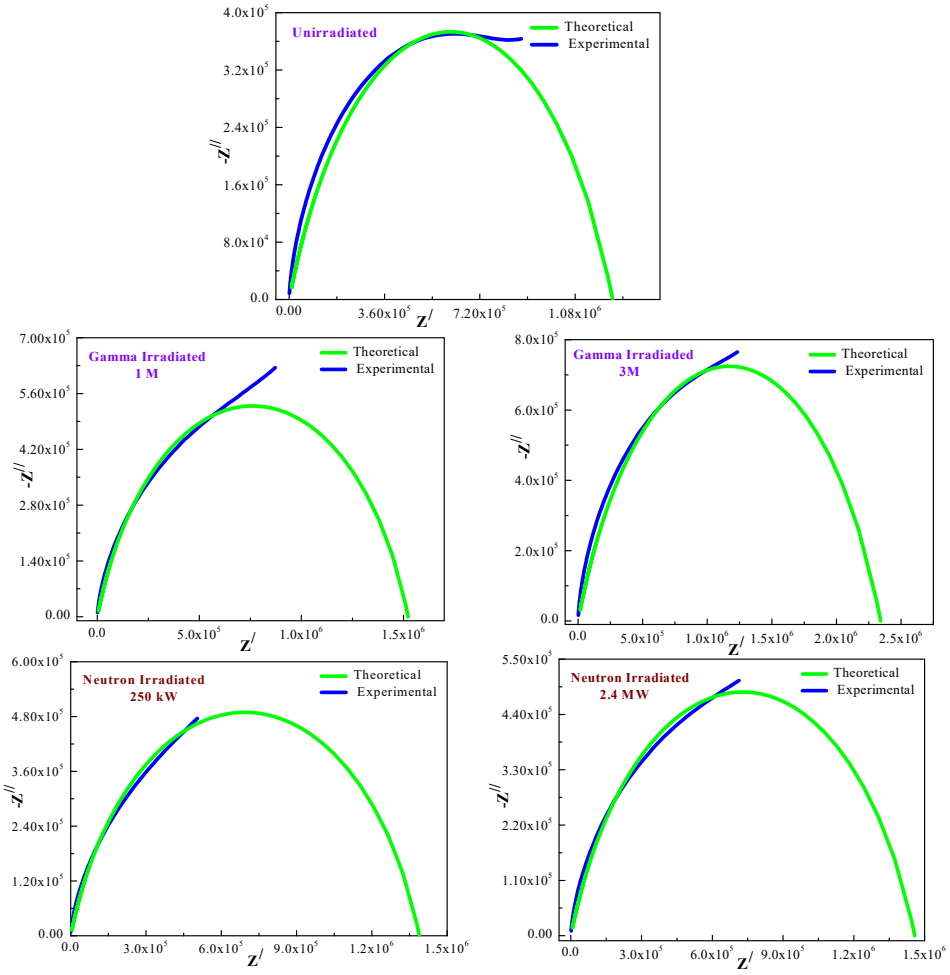

Fig. 4.31 Cole-Cole (grain data) fitted plots of impedance for $Ni_{0.3}Cu_{0.2}Cd_{0.5}Fe_2O_4$ nanoparticles before and after gamma and neutron irradiation.

It contains separate parallel arrangements of C_g and R_g(grain parameters) and C_{gb} and R_{gb} (grain boundary parameters) and models the observed semicircles in the impedance study. Table 4.1 shows the grain and grain boundary parameters for both irradiation cases. In Table 4.1, R_g and R_{gb} are observed with increasing magnitudes while C_g and C_{gb} declined with both the gamma and neutron irradiation doses. This causes a change in grain distribution.

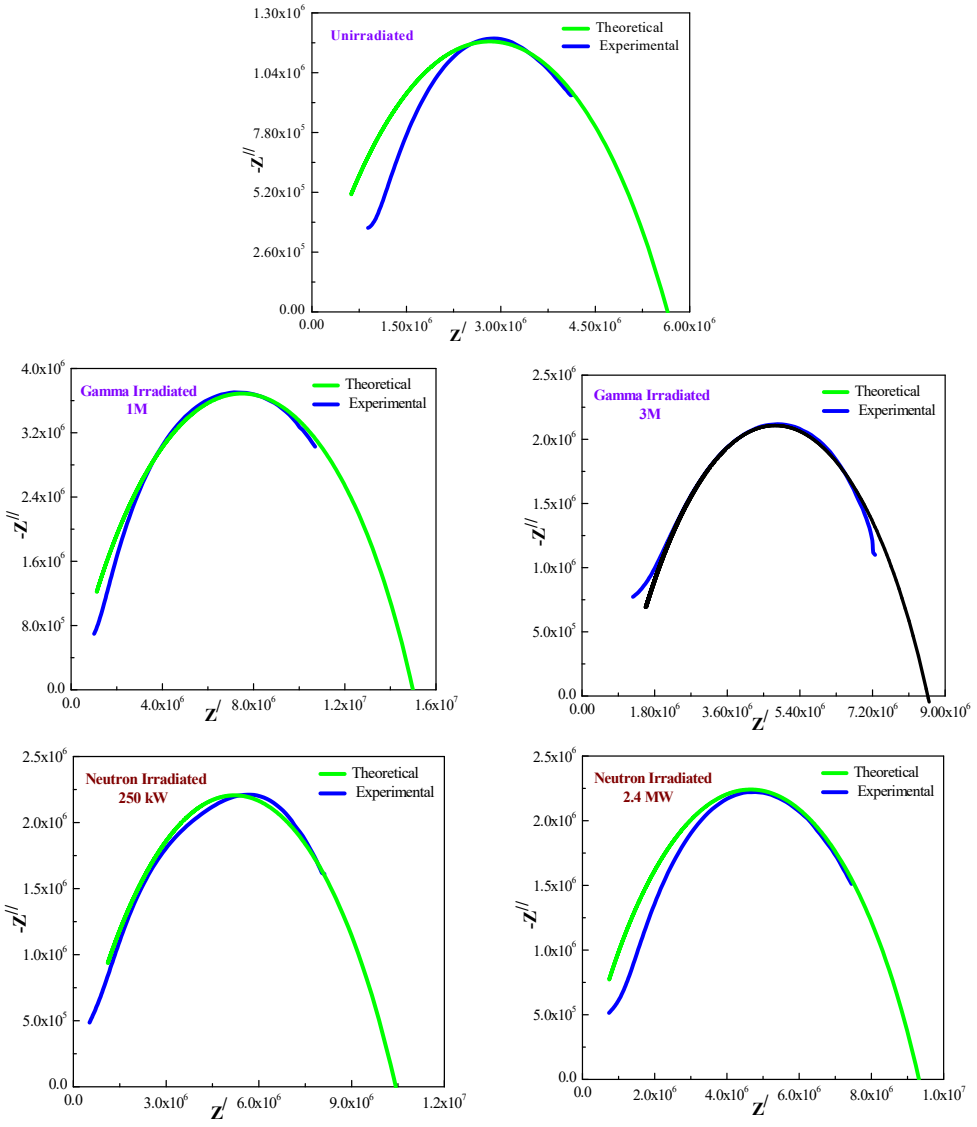

Fig. 4.32 Cole-Cole (grain boundary data) fitted plots of impedance for $Ni_{0.3}Cu_{0.2}Cd_{0.5}Fe_2O_4$ nanoparticles before and after gamma and neutron irradiation.

The change in grain structures causes a plenty of grain boundaries in the structure. The grain boundaries act as barriers and confine the charge flow [160]. Fig. 4.31 and Fig. 4.32 represent the well-fitting of the experimental and theoretical grain and grain boundary data for both the irradiation cases.

4.2.9 AC CONDUCTIVITY STUDY

Electrical conductivity is an intrinsic phenomenon of any material and expresses the electric current conducted by the material. At room temperature, ferrite materials are observed to show electrical conductivity with a wide range, about 10^{-9} to 10^{4} $(\Omega.m)^{-1}$ [160]. In the case of synthesized nanoparticles, frequency-dependent conductivity study is performed with the following expression,

$\sigma_{ac} = \varepsilon' \varepsilon_0 \omega tan\delta = \varepsilon'' \varepsilon_0 \omega$ ..... (4.16)

where, ω and ε_o symbolize the angular frequency and free space permittivity respectively.

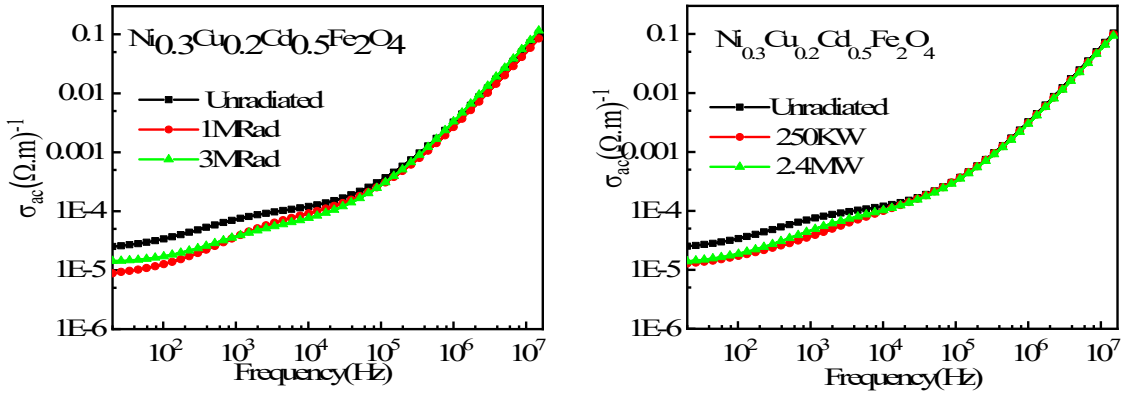

Fig. 4.33 Variation in ac conductivity of $Ni_{0.3}Cu_{0.2}Cd_{0.5}Fe_2O_4$ ferrite nanoparticles before and after gamma and neutron irradiation by different dose.

The variation of electrical conductivity with frequency for both the irradiation cases has been shown in Fig. 4.33. It is seen that conductivity possesses very low magnitudes and shows an almost frequency-independent nature initially while at a higher frequency, conductivity is

found to rise sharply with increasing frequency at both the irradiation cases. Therefore, electrical conductivity plots present frequency invariant nature i.e. dc nature at low frequency and frequency dependency i.e. ac nature at a higher frequency. The dc and ac nature observed in our investigation can be explained with Jonscher's power law [161] which illustrates both the dc and ac nature by the expression,

$\sigma\ (\omega) = \sigma(0) + A\omega^n$ …… (4.17)

where σ(0) presents the dc nature while σ(ω) expresses the ac characteristic, A is a constant, n is an exponent and 0 < n < 1.The dc nature σ(0) can be expressed as [136]

$\sigma\ (0) = \frac{\mathrm{L}}{\mathrm{AR}}$ …… (4.18)

where A and L represent the cross-sectional area and height (thickness) respectively. In the study, the frequency invariant nature observed initially shows the translational hopping effects with long-range nature and obeys the dc expression of Jonscher's power law. The frequency dependency of conductivity obtained at higher frequency extents presents the hopping motion having localized or reorientation nature with a significant contribution. This frequency dependency of conductivity plots follows the ac expression of Jonscher's power law [136, 162]. The high-frequency behavior also reveals the influence of lower dielectric magnitudes observed at higher frequencies in our dielectric study and thus provides a good agreement with the dielectric result. The hopping between Fe^{2+} and Fe^{3+} is observed at low frequency due to a more active grain boundary. At higher frequencies, hopping between Fe^{2+} and Fe^{3+} gets promoted with more active at conductive grains. This increasing hopping conduction causes an increase in ac electrical conductivity at a higher frequency [163]. Besides, two competing relaxation characteristics, unsuccessful hopping and successful hopping can also be observed at higher frequencies (~MHz). The rising ratio of successful to unsuccessful hopping also causes high-frequency conductivity with dispersive nature [162].

CHAPTER 5: CONCLUSIONS

5.1 GENERAL

This present investigation examined the electrical, magnetic, and physical characteristics of nanoferrites ($Co_{0.3}Cu_{0.2}Cd_{0.5}Fe_2O_4$ and $Ni_{0.3}Cu_{0.2}Cd_{0.5}Fe_2O_4$) both before and after gamma and neutron irradiation.

5.2 KEY FINDINGS

The present study examined the effects of gamma and neutron irradiations on the electrical, magnetic, and physical characteristics of nano ferrite samples, which have the chemical formulas $Ni_{0.3}Cu_{0.2}Cd_{0.5}Fe_2O_4$ and $Co_{0.3}Cu_{0.2}Cd_{0.5}Fe_2O_4$. Based on the acquired data, the following deduction may be made.

- Before and after gamma and neutron irradiation, the spinel single phase-structure was shown in all of the samples that were examined.
- The materials' XRD spectra showed peak shifts and conversions in the relative intensity of the peaks after gamma and neutron irradiation. These results were attributed to the cubic lattice's deformation caused by irradiation.
- Gamma irradiation of $Co_{0.3}Cu_{0.2}Cd_{0.5}Fe_2O_4$ and $Ni_{0.3}Cu_{0.2}Cd_{0.5}Fe_2O_4$ nanoferrite decreases its particle size (L), while it increases the unit cell volume, T_C and room temperature values of χ_M, ε', $tan\delta$ and σ.
- Neutron irradiation of the nanoferrite decreases the unit cell volume while increasing its particle size (L), T_C, and room temperature values of χ_M, ε', tanδ and σ.
- It was discovered that the gamma and neutron irradiation method reduced the crystallite size. Moreover, the conversion of certain Fe^{+} ions (0.67Å) to Fe^{2+} ions (0.76Å). may be the cause of the minor rise in the lattice constant of all samples under investigation.

- After being exposed to gamma and neutron irradiation in each composition, the lattice parameter increased.
- From M-H curve, it is apparent that at room temperature the nanocrystalline samples of $Co_{0.3}Cu_{0.2}Cd_{0.5}Fe_2O_4$ and $Ni_{0.3}Cu_{0.2}Cd_{0.5}Fe_2O_4$ are in a ferrimagnetic state. As the dosage of gamma and neutron irradiation increases, the saturation magnetization, M_s, decreases. The distribution of cations and the exchange interaction between the A and B sites might account for this outcome. The reduction of M_s in nanocrystalline is caused by the random canting of nanoparticles caused by anti-ferromagnetic exchange interactions as a consequence of gamma and neutron irradiation at different dosages.
- Dispersion curves of the dielectric constant έ, dielectric loss ε'' and ρ_{AC} with frequency as found to be decreased with frequency for each composition. The values of ε' and ε'' decreased also after gamma and neutron irradiation. The two layers model provided an explanation for these findings.
- Two overlapping incomplete semicircles may be seen in the sample Cole–Cole (Z'' vs Z') plots. The first is caused by the conduction of the grains at low frequencies, where it is impossible to determine their electrical parameters. The second is brought on by the conduction of the grain boundaries at high frequencies, where the values display a notable variation in response to the radiation dosage and have a larger capacitance and lower resistance than the grain boundaries.
- The semicircular Cole–Cole plots of (M'' vs M') guarantee that the electric stiffness of the samples under investigation is the primary characteristic both before and after the irradiation dosage.
- Similar to Ni-Cu-Cd ferrite samples, the ac conductivity of Co-Cu-Cd ferrite samples increases as the gamma and neutron irradiation dosage increases. However, the extra influence of their microstructures beyond cation redistribution results in greater values.

- After being exposed to gamma and neutron radiation, the conductivity, dielectric constant, and dielectric loss all increased, and this relationship held true for the ratio Fe^{2+}/Fe^{3+}.

This result indicates that irradiation has a significant impact on the structural, magnetic, and electrical characteristics of Co-Cu-Cd and Ni-Cu-Cd ferrites. Ultimately, it can be said that even though samples of $Ni_{0.3}Cu_{0.2}Cd_{0.5}Fe_2O_4$ exhibit more magnetization and resistivity than samples of $Co_{0.3}Cu_{0.2}Cd_{0.5}Fe_2O_4$ when subjected to very high doses of gamma and neutron irradiation.

Limitation of Study

The available raw materials used directly without further justification. Due to lack of proper time during research time Temperature dependent magnetization and Magnetocaloric effect could not be done.

Practical Implication

The result found potential for high radiation environment like nuclear reaction facilities and high energy acceleration etc.

Recommendation for Further Study

Mossbauer effect analysis, Temperature dependent magnetization, Magnetocaloric effect, PE loop and isotope changes after gamma, neutron and LASER irradiation can be analyzed.

CHAPTER 5: CONCLUSION

BIBLIOGRAPHY

[1] J.Smit, Magnetic Properties of Materials, second ed. Mc-Grew Hill, New York, 1972.

[2] A.Yang, C.N. Chinnasamy, J.M. Greneche, Y. Chen, S.D. Yoon, K. Hsu, C. Vittoria, V.G. Harris, Appl. Phys. Lett. 94 (2009) 113109.

[3] Y. Ahn, E.J. Choi, S. Kim, D.H. An, K.U. Kang, B.G. Lee, K.S. Baek, H.N. Oak, J. Korean Phys. Soc. 41 (2002) 123.

[4] M.K. Roy, B. Halder, H.C. Verma, Nanotechnology 17 (2006) 232.

[5] H. Xue, Z. Li, X. Wang, X. Fu, Mater. Lett. 61 (2007) 347.

[6] J.P. Singh, R.C. Srivastava, H.M. Agrawal, R.P.S. Kushwaha, P. Chand, R. Kumar, Int.J.Nanosci. 7 (2008) 21.

[7] S.T. Assar, H.F. Abosheiasha, A.R. El Sayed, Journal of Magnetism and Magnetic Materials 421 (2017) 355.

[8] M.A. Ahmed, S.I. El-dek ,S.F. Mansour, N. Okasha, Solid State Sciences 13(2011) 1180.

[9] Y.G. Chukalkin, B. N. Goshchitskii, S. F. Dubinin, S. K. Sidorov, V. V. Petrov, V. D. Parkhomenko, V. G. Vologin, Phys. Stat. Sol. (a) 28 (1975) 345.

[10] V.V. Petrov, Y.G. Chukalkin, B.N. Goshchitskii, Sov. Phys. Solid State 22 (1980) 339.

[11] M.A. Mousa and M.A. Ahmed, Journal of Material Science 23 (1988) 3083.

[12] M.A. Mousa, A.M. Summan, M.A. Ahmed and A.M. Badawy, J. Mater. Sci. 24 (1989) 2478.

[13] H.E.Hassan, T.Sharshar, M.M. Hessien, O.M. Hemeda, Nucl. Instrum. Methods Phys. Res. B 304 (2013) 72.

[14] Maheshkumar L. Mane, S.E. Shirsath, Vinod N. Dhage, K.M. Jadhav, Nucl. Instrum. Methods Phys. Res. B 269 (2011) 2026.

[15] B.Tareev, Physics of Dielectric Materials. Mir, Moscow, 1979.

[16] I.M. Hamada, J. Magn. Magn. Mater. 271 (2) (2004) 318.

[17] J. P. Singh, R. Singh, S. Ghosh, A. Tripathi, D. Kabiraj, S. Gupta, T. Som, Ravi Kumar, S. K. Arora, K. Asokan, D. K. Avasthi, D. Kanjilal, N. C. Mishra and G. K. Mehta, Nucl.Inst. Meth. Phys. Res. B 156 (1999) 206.

[18] M. Veena, A. Somashekarappa, G.J. Shankaramurthy, H.S. Jayanna, H.M. Somashekarappa, J. Magn. Magn. Mater. 419 (2016) 475.

[19] A. Karim, Sagar E. Shirsath, S.J. Shukla, K.M. Jadhav. B 268 (2010) 2706.

[20] Kee-Nam Choo, Man-Soon Cho, Byung-Hyuk Jun, Chan-Joong Kim, Sang-Jun Park. 2014, 2, 837.

[21] Dogra Anjana, M. Singh, Kumar Ravi, Nucl. Instrum. Methods Phys. Res. B 207 (2003) 296.

[22] Ghosh Sanjukta, O. Ayyub, N. Kumar, S.A. Khan, D. Banerjee, Nucl. Instrum. Methods Phys. Res. B 212 (2003) 510.

[23] M.C. Chhantbar, K.B. Modi, G.J. Baldha, H.H. Joshi, R.V. Upadhyay, Kumar Ravi, Nucl. Instrum. Methods Phys. Res. B 244 (2006) 124.

[24] Kumar Ravi, Sharma S.K., Dogra Anjana, Kumar V.V. Siva. Dolia S.N., Gupta A., Knobel M., Singh M., Hyperfine Interact. 160 (2005) 143.

[25] Darwish N.Z., Hemeda O.M., AbdJElati M.I., Appl. Radiat. Isot. 45 (4) (1994) 445.

[26] Hemeda M., ElJSaadawy M., J. Magn. Magn. Mater. 256 (2003) 63.

[27] Dalal Mohammed Hemeda, J. Appl. Sci. 2 (5) (2005) 989.

[28] Ateia E., Egypt. J. Solids, 29 (2) (2006) 317

[29] M.A. Ahmed , Ateia E., Abdelatif G., Salem F.M., Mater Chem. Phys. 81 (2003) 63.

[30] Okasha N., J. Alloys Compd., 490 (2010) 307.

[31] Karim Asif, Shirsath Sagar E., Shukla S.J., Jadhav K.M., Nucl. Instr. and Meth. In Phys. Res. B (2010) Accepted Manuscript.

[32] Zhenxing Yue, Ji Zhou, Longtu Li, Ziaohui Wang, Zhilun Gui, Mater. Sci. Eng., B 86 (2001) 64.

[33] Vital A., Angermann A., Dittmann R., Graule T., Töpfer, J., Acta Mater. 55 (2007) 1995.

[34] Raju Seetha Rama V., Murthy S.R., J. Mater. Sci. 41 (2006) 1475.

[35] B.M. Sahanashreea, E. Melagiriyappaa, H.S. Jayanna, H.M. Somashekarappac, Radiation Physics and Chemistry 139 (2017) 55–65

[36] M. Veena, G.J. Shankaramurthy, H.S. Jayanna, H.M. Somashekarappa, Journal of Alloys and Compounds 735 (2018) 2532-2543.

[37] B.D.Cullity, Elements of X-Ray Diffraction. Addison Wesley, 1978.

[38] J.A. Mydosh, Spin Glasses: an Experimental Introduction, Taylor and Francis, London Washington, DC, 1993.

[39] A.K. Nikumbh, A.V. Nagawade, G.S. Gugale, M.G. Chaskar, P.P. Bakare, J. Mater.Sci. 37 (2002) 637.

[40] J.B. Nelson, D.P. Riley. Proc. Phys. Soc. London. 57 (1945)160.

[41] T.L. Templeton, A.S. Arrott, A.E. Curzon, M.A. Gee, X.-Z. Li, Y. Yoshida, P.J. Schurer, J.L. Lacombe. J. Applied Phys. 73 (1993) 6728.

[42] Goldman, Handbook of Modern Ferromagnetic Materials, Kulwer Acad. Pub, Boston, USA, 1999.

[43] P.A. Shaikh, R.C. Kambale, A.V. Rao, Y.D. Kolekar.J. Alloys. Compd. 482 (1-2) (2009)276.

[44] R.C. Kambale, P.A. Shaikh, C.H. Bhosale, K.Y. Rajpure, Y.D. Kolekar.J. Smart Mat. Structr. 18(8) (2009) 085014.

[46] P.P. Naik, R.B. Tangsali, S.S. Meena, Pramod Bhatt, B. Sonaye, S. Sugur, Radiat.Phys. Chem. 102 (2014) 147–ne152.

BIBLIOGRAPHY

[47] P.P. Naik, R.B. Tangsali, B. Sonaye, S. Sugur, AIP Conf. Proc. 1512, 354, 2013. (http://dx.doi.org/10.1063/1.4791057).

[48] L. Maheshkumar, V. Mane, N. Dhage, P.S. Aghav, M.K. Babrekar, K.M. Jadhav, AIP Conference Proceedings 1349, 1131, 2011. ⟨http://dx.doi.org/10.1063/1.3606261⟩.

[49] M.M. Eltabey, I.A. Ali, H.E. Hassan, M.N.H. Comsan, J. Mater. Sci. 46(2011)2294.

[50] G.K. Williamson, W. Hall, Acta Metall. 122 (1953).

[51] R.D. Waldron, Phys. Rev. 99 (1955) 1727.

[52] Sonal Singhal, Sheenu Jauhar, N. Lakshmi, S. Bansal, J. Mol. Struct. 1038 (2013)45.

[53] H.F. Abosheiasha, S.T. Assar, J. Magn. Magn. Mater. 370 (2014) 54–61.

[54] B. Viswanathan, V.R.K. Murthy, Ferrite Materials; Science and Technology,Narosa Publishing House, New Delhi, 1990.

[55] M. Abdullah Dar, Vivek Verma, S.P. Gairola, W.A. Siddiqui, RakeshKumar Singh, R.K. Kotnala, Appl. Surf. Sci. 258 (2012) 5342.

[56] N. Okasha, J. Mater. Sci. 43 (2008) 4192.

[57] O.M. Hemeda, M. El-Saadawy, J. Magn. Magn. Mater. 256 (2003) 63.

[58] G.P. Pells, J. Nucl. Mater. 184 (1991) 177.

[59] R. Dupree, M.H. Levis, M.E. Smith, Philos. Mag. A 53 (1986) L17.

[60] A. Ibarra, R. Vila, M.Jimenez de Castro, Philos. Mag. Lett. 64(1991)45.

[61] V. Skvortsova, N. Mironova-Ulmane, U. Ulmanis, Nucl. Instrum. Meth.B. 191(2002)256.

[62] P. B. Belavi, G. N. Chavan, B. K. Bammannavar, L. R. Naik, R. K. Kotnala, J. Mat. Chem. Phys. 132(2012) 138.

[63] O.M. Hemeda. Turk. J. Phys. 28 (2004) 121.

[64] D.R. Patil, B.K. Chougule, J. Mat. Chem. Phys. 117 (2009) 35.

[65] S.K.Ahmed, M.B. Hossen, 5 (2016) 111.

[66] K.M.Batoo, S. Kumar, C.G. Lee and Alimuddin, Curr. Appl.Phys.9 (2009) 826.

[67] M. Ramay, S.A. Siddiqi, S.Atiq, M.S. Awan and S. Riaz,Chin. J.Chem. Phys. 23 (2010) 591.

[68] T. Ramesh, R.S. Shinde and S.R. Murthy, J. Magn, Magn. Mater. 345 (2013) 276.

[69] M. Hashim. Alimuddin, S.Kumar, S. Ali, B.H. Koo, H. Chang and R. Kumar, j.Alloys Compd. 511 (2012) 107.

[70] M.M. Haque, M. Huq. And M.A. Hakim, Mater. Chem. Phys. 112 (2008) 580.

[71] M. Chanda, Science of Engineering Materials, 3 (1980) 580.

[72] D. Ravinder, Mat. Lett. 54 (2004) 68.

[73] N. Rezlescu, E. Rezlescu, Phys. Stat. Sol. (a) 23 (1974) 575.

[74] A.V.R. Reddy, G.R. Mohan, D. Ravinder, B.S. Boyanov, J. Mater. Sci. 34 (1999) 3169.

[75] A.Y. Lipare, P.N. Vasambekar, A.S. Vasambekar, J. Magn. Magn. Mater. 279 (2004) 160.

[76] K.W. Wagner, Ann. Phys. 40 (1913) 817.

[77] V.R.K. Murthy, J. Sobhanadri, Phys. Stat. Sol. (a) 36 (1976) 129.

[78] R.G. Kharabe, R.S. Devan, C.M. Kanamadi, B.K. Chougule, Smart Mater.Struct. 15 (2006) N36.

[79] Muhammad Ajmal, Asghari Maqsood, J. Alloys Compd.460 (2007) 54.

[80] I.M. Hamada, J. Magn. Magn. Mater. 271 (2004) 318.

[81] Dalal Mohammed Hemeda, J. Appl. Sci. 2 (5) (2005) 989.

[82] E. Ateia, Egypt. J. Solids, 29 (2) (2006) 317.

[83] M.A. Ahmed, E. Ateia, F.M. Salem, J. Mater Sci 42 (2007) 3651.

[84] M.A. Mousa, A.M. Summan, M.A. Ahmed, Thermochim Acta 144 (1989) 45.

[85] O.S. Josyulu, J. Sobhanadri, Phys. Stat. Sol. (a), 59 (1980) 323.

[86] P. Venugopal Raddy, T. Seshadiri Rao, J. Less, J. Common Met. 105 (1985) 63.

[87] S.A. Mazen, Mater Chem. Phys. 62 (2000) 139.

[88] D. Ravinder, A. V. Ramana Reddy, G. Rammga Mohan, Mater. Lett. 48 (2001) 210.

[89] E. Ateia, Egypt. J. Solids, 29 (2) (2006) 317.

[90] E. Otsuki, S. Yamada, T. Otsuki, K. Shoji, T. Sato, J. Appl Phys., 69(8): (1991)5942.

[91] V.R.K. Murthy, J. Sobhanadri, Phys. Stat. Sol. (a) 36 (1976) 129.

[92] S.A. Mazen, Mater Chem. Phys. 62 (2000) 139.

[93] D. Ravinder, A. V. Ramana Reddy, G. Ranga Mohan, Mater. Lett. 48 (2002) 259.

[94] S.S. Bellad, B.K. Chougule, Mater Chem. Phys., 66 (2000) 58.

[95] A.Y. Lipare, P.N. Vasambekar, A.S. Vasambekar, J. Magn. Magn. Mater. 279 (2004) 160.

[96] C.G. Koop's, Phys. Rev. 83 (1951) 121.

[97] N. Rezlescu and E. Rezlescu, Phys. Status Solidi (a) 23 (1974) 575.

[98] L. Kumar and M. Kar, J. Magn. Magn Mater. 323 (2011) 2042.

[99] N. Singh, A. Agarwal, S. Sanghi, S. Khasa, J. Magn. Magn. Mater. 324 (2012)2506.

[100] N. Sivakumar, A. Narayanasamy, N. Ponpandian, G. Govindara, J. Appl. Phys.101 (2007) 1.

[101] J.R. Macdonald Wiley, New York, (1987).

[102] M. Kaiser, Phys. B 407 (2012) 606.

[103] A. Mishra, S.N. Choudhary, K. Prasad and R. N. P. Choudhary, Phys. B 406 (2011)3279.

[104] I. Ali, M. U. Islam, M. N. Ashiq, I. Shakir, N.M. Karamat Ishaque, M. N. Akhter, H. M. Khan, M. Irfan and M. A. Khan, Ceram. Int. 41 (2015) 8748

[105] B.V. R. Chowdari and R. Gopalkrishnnan, Solid State Ionics 23 (1987) 225.

[106] N. Sivakumar, A. Narayanasamy, N. Ponpandian, G. Govindara, J.Appl.Phys.101 (2007) 1.

[107] S.A. Saafan, A.S. Seoud, R.E. El Shater, Physica B 365 (2005) 27.

[108] S.A. Saafan, Physica B 403 (2008) 2049.

[109] Mohd Hashim, Alimuddin, Shalendra Kumar, Sikander Ali, B.H. Koo, H. Chung,Ravi Kumar, J. Alloy. Compd. 511 (2012) 107.

[110] M. Abdullah Dar, Vivek Verma, S.P. Gairola, W.A. Siddiqui, Rakesh Kumar Singh, R.K. Kotnala, Appl. Surf. Sci. 258 (2012) 5342.

[111] Philippe Knauth, Harry L. Tuller, J. Am. Ceram.Soc. 85 (7) (2002)1654.

[112] S.A. Mazen, N.I. Abu-Elsaad, Appl. Phys. A: Mater. Sci. Proc. 122 (2016) 1.

[113] R.C. Kambale, P.A. Shaikh, C.H. Bhosale, K.Y. Rajpure, Y.D. Kolekar, Smart Mater.Struct. 18 (2009) 1.

[114] M.F. Mahmood, M.B. Hossen, J Mater Sci: Mater Electron 32(2021) 14248.

[115] S.S. Bellad, and B.K. Chougle, Mater. Chem. Phys.66 (2000) 58.

[116] R. G. Kulkarni, V. U. Patil, J. Mater. Sci.17(1982)843.

[117] M. G. Chourashiya, J. Y. Patil, S.H. Pawar and L. D. Jadhab, Mater. Chem. Phys. 109(2008)39.

[118] D. Alder and J. Feinlieb, Phys. Rev. B 2 (1970)31.

[119] I. G. Austin and N. F. Mott, Adv. Phys. 18(1969)41.

[120] A. Vermaa, O. P. Thakur, C. Prakash, T. C. Goel and R. G. Mendiratta, Mater. Sci. Eng. B 116(2005)1.

[121] P. B. Belavi, G. N. Chavan, L. R. Naik, R. Somashekar, and R. K. Kotnala, Materials Chemistry and Physics 132, 138 (2012).

[122] M. Veena, A. Somashekarappa, G. J. Shankaramurthy, H. S. Jayanna, and H. M. Somashekarappa, Journal of Magnetism and Magnetic Materials 419, 375 (2016).

[123] H. Abosheiasha and S. T. Assar, Journal of Magnetism and Magnetic Materials 370, 54 (2014).

[124] G.P. Pells, Journal of Nuclear Materials 184, 177 (1991).

[125] V. Skvortsova, N. Mironova-Ulmane, and U. Ulmanis, Nuclear Instruments and Methods in Physics Research, Section B: Beam Interactions with Materials and Atoms 191, 256 (2002).

[126] A. Ibarra, R. Vila, and M. J. De Castro, Philosophical Magazine Letters 64, 45 (1991).

[127] O.M. Hemeda, Journal of Physical Chemistry B 110, 23637 (2006).

[128] D.R. Patil and B. K. Chougule, Materials Chemistry and Physics 117, 35 (2009).

[129] J.C. Maxwell, Electricity and Magnetism, Vol. 1 (Oxford University Press, Oxford, 1929).

[130] C.G. Koops, On the Dispersion of Resistivity and Dielectric Constant of Some Semiconductors at Audio frequencies (1951).

[131] M.B. Hossen, M. S. Alam, N. M. Eman, and N. J. Shirin, Phase Transitions 92, 719 (2019).

[132] M.S. Alam, R. Hossain, and M. A. Basith, Ceramics International 44, 1594 (2018).

[133] B.H. Devmunde, A. V. Raut, S. D. Birajdar, S. J. Shukla, D. R. Shengule, and K. M. Jadhav, Journal of Nanoparticles 2016, 1 (2016).

[134] S.T. Assar, H. F. Abosheiasha, and A. R. El Sayed, Journal of Magnetism and Magnetic Materials 421, 355 (2017).

[135] P. Mathur, A. Thakur, and M. Singh, Physica Scripta 77, (2008).

[136] V.S. Vinila and J. Isac, Int. J. Sci. Res. 7, 696 (2018).

[137] M. Hashim, Alimuddin, S. Kumar, S. Ali, B. H. Koo, H. Chung, and R. Kumar, Journal of Alloys and Compounds 511, 107 (2012).

[138] N. Singh, A. Agarwal, and S. Sanghi, Current Applied Physics 11, 783 (2011).

[139] M. Ajmal, N. A. Shah, A. Maqsood, M. S. Awan, and M. Arif, Journal of Alloys and Compounds 508, 226 (2010).

[140] C.G. Koop's,Phys. Rev. 83 (1951) 121.

[141] N. Rezlescu and E. Rezlescu, Phys. Status Solidi (a) 23 (1974) 575.

[142] L. Kumar and M. Kar, J. Magn. Magn Mater. 323 (2011) 2042.

[143] K.M.Batoo, S. Kumar, C.G. Lee and Alimuddin, Curr. Appl.Phys.9 (2009) 826.

[144] M. Ramay, S.A. Siddiqi, S.Atiq, M.S. Awan and S. Riaz,Chin. J.Chem. Phys. 23 (2010) 591.

[145] T. Ramesh, R.S. Shinde and S.R. Murthy, J. Magn, Magn. Mater. 345 (2013) 276.

[146] A.A. Birajdar, S. E. Shirsath, R. H. Kadam, S. M. Patange, D. R. Mane, and A. R. Shitre, Ceramics International 38, 2963 (2012).

[147] M. Kaiser, Physica B: Condensed Matter 407, 606 (2012).

[148] M. Arifuzzaman and M. B. Hossen, Results in Physics 16, 102824 (2020).

[149] M.A. Rafiq, M. N. Rafiq, and K. Venkata Saravanan, Ceramics International 41, 11436 (2015).

[150] J. Suchanicz, Materials Science and Engineering B B55, 114 (1998).

[151] K. Prabakar, S. K. Narayandass, and D. Mangalaraj, Materials Science and Engineering B: Solid-State Materials for Advanced Technology 98, 225 (2003).

[152] A. Bagum, M. B. Hossen, and F.-U.-Z. Chowdhury, Ferroelectrics 494, 19 (2016).

[153] J.T.S. Irvine, D.C. Sinclair, and A. R. West, Advanced Materials 2, 132 (1990).

[154] R. Padhee, P. R. Das, B. N. Parida, and R. N. P. Choudhary, Journal of Materials Science: Materials in Electronics 23, 1688 (2012).

[155] K.M. Batoo, S. Kumar, C.G. Lee, and Alimuddin, Journal of Alloys and Compounds 480, 596 (2009).

[156] A.M.M. Farea, S. Kumar, K. M. Batoo, A. Yousef, C. G. Lee, and Alimuddin, Journal of Alloys and Compounds 464, 361 (2008).

[157] H. Ye, R. B. Jackman, and P. Hing, Journal of Applied Physics 94, 7878 (2003).

[158] M.M. Costa, G. F. M. Pires Júnior, and A. S. B. Sombra, Materials Chemistry and Physics 123, 35 (2010).

[159] P.R. Arjunwadkar and R. R. Patil, Journal of Alloys and Compounds 611, 273 (2014).

[160] R.N. Aljawfi, F. Rahman, and K. M. Batoo, Journal of Molecular Structure 1065–1066, 199 (2014).

[161] A.K. Jonscher, Nature 267, 673 (1977).

[162] M.B. Hossen and A. K. M. A. Hossain, Journal of Magnetism and Magnetic Materials 387, 24 (2015).

[163] B.M. Sahanashree, E. Melagiriyappa, M. Veena, G.J. Shankaramurthy, A. Somashekarappa, H.S. Jayanna, and H. M. Somashekarappa, Radiation Physics and Chemistry 139, 55 (2017).

[164] C.G. Koops, Phys. Rev. 121 (1951) 83.

[165] J. Hyun, P. Piot and T. Sen, 22 (2018)

[166] R.G. Dale and J. Wondergem of the IAEA publication (ISBN 92-0-107304-6): Nuclear Medicine Physics: A Handbook for Teachers and Students

[167] R. Kerstin, https://edaxblog.com/2018/05/15/one-analysis-technique-so-many-options/

[168] J. Louis, V. Belle, https://readingfeynman.org/tag/symmetry-breaking/

[169] Lucas S. do Carmo, 18(2015), DOI: 10.13140/RG.2.1.2880.1369